Midrapidity Neutral-Pion Production in Proton-Proton Collisions at $\sqrt{s} = 200\text{GeV}$

Hisayuki Torii

A dissertation submitted in partial fulfillment of
the requirements for the degree of doctor of science

Department of Physics
Kyoto University

July,2004

Midrapidity Neutral-Pion Production in Proton-Proton Collisions at $\sqrt{s} = 200\text{GeV}$

Hisayuki Torii

2004

Abstract

We report the cross section of the neutral pion (π^0) production from the proton-proton collisions at $\sqrt{s}$ of 200GeV at the PHENIX experiment. This is the neutral pion measurement at the highest energy in the world as the proton-proton collisions. During 2001–2002, the Relativistic Heavy Ion Collider (RHIC) was successfully operated as the first polarized proton collider. The analyzed sample consists of 16M events of minimum bias trigger and 18M events of high-p_T trigger, which are equivalent to the beam luminosity of 39nb^{-1}. The measured p_T range is from 1.22GeV/c to 13.25GeV/c and the pseudo-rapidity range is from -0.35 to +0.35.

Two photons decaying from π^0 are detected by the PHENIX electro-magnetic calorimeter. The uncertainty of the absolute energy scale is the main source of the systematic error on the π^0 measurements. The total systematic error is between 10% to 15% depending on the measured p_T. The normalization error, which is the systematic error on the luminosity, is 9.6%. The present result is consistent with a next-to-leading-order perturbative Quantum ChromoDynamics (pQCD) calculation within the uncertainty of the measurement and the calculation. This work provides an essential reference data for detecting the jet quenching effect, which is predicted to be a probe of the QGP, at the RHIC experiment.

Contents

Chapter 1

Introduction

The Relativistic Heavy Ion Collider (RHIC) is constructed at Brookhaven National Laboratory (BNL) to provide collisions of polarized proton at the center of mass energy ($\sqrt{s}$) up to 500GeV and nucleus at the center of mass energy per nucleon ($\sqrt{s_{NN}}$) up to 200GeV. For the first time during 2001–2002, the RHIC was successfully operated as the first polarized proton collider in the world.

The Pioneering High Energy Nuclear Interaction eXperiment (PHENIX) detector triggered 4×10^9 events at $\sqrt{s}$ of 200 GeV. This study uses the PHENIX electro-magnetic calorimeters (EMCal), which are sitting in two central arms. Each arm has an azimuthal coverage of $90°$ and pseudo-rapidity coverage of ± 0.35. The data were collected using the minimum bias trigger and newly installed high-p_T trigger. The high-p_T trigger is essential in enhancing the sample of neutral pions at high p_T. We report the measurement of spin-averaged neutral pion cross section in proton-proton collisions.

In this chapter, we introduce two motivations for this work together with a brief review on the neutral pion production at high energy collisions. One motivation is to provide a testing ground of perturbative Quantum ChromoDynamics (pQCD) [1] and the other is to provide a reference data for Quark Gluon Plasma (QGP) search. We describe the two in Section 1.1 and Section 1.2, respectively.

1.1 Perturbative Quantum ChromoDynamics

1.1.1 Quark and Confinement

The very start-line of the quark model was marked by the introduction of new quantum number by Gell-Mann and Nishijima in 1953, named as strangeness. In 1956, S. Sakata group introduced a similar model with a different quantum coordination. At this time, anyone didn't think the new quantum number is related to the structure of nucleon. Many new particles with the strangeness number were discovered on the accelerators; the Bevatron at Berkeley from 1954 and the Cosmotron from 1952 and the Alternating Gradient Synchrotron (AGS) from 1960 at Brookhaven National Laboratory (BNL). The SU(3) hadron model was introduced by Gell-Mann and Ne'eman in 1961 in order to categorize the new strangeness particles and the model was a first trigger to understand the structure of the nucleon. The quark were introduced by Gell-Mann in 1964 and the gluon with the idea of color were introduced by Nambu and Han and also by Greenberg in 1965. They were baseline of the Quantum ChromoDynamics (QCD) theory introduced in 1973 [2]. Due to the color force, the quark and gluon are confined inside the hadron. The first experimental evidence [3, 4, 5] of the constituent parton in proton was reported in deep inelastic scattering at Stanford Linear Accelerator Center (SLAC). About 25 years later of the first discovery, the top quark was reported [6] in $p + \bar{p}$ collisions at the Tevatron in Fermi National Accelerator Laboratory (Fermilab).

Interaction Between Two Quarks. (Running Coupling Constant) The interaction between two quarks are mediated by the gluon and its color charge. Like the vacuum polarization in Quantum ElectroDynamics (QED), the quark and gluon have self energy as shown in Figure 1.1(A)–(C).

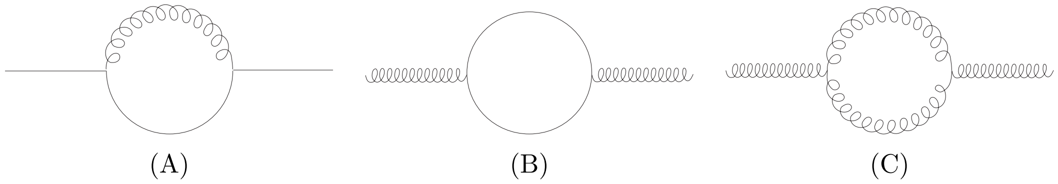

Figure 1.1: *Diagrams of (A)quark self energy and (B)(C)gluon self energy through vacuum polarization.*

Because the gluon interacts with itself as shown in Figure 1.1(C), the interaction between quarks is very different from that between electrons. The effective coupling constant in short distance is smaller than that in long distance unlike QED. The effective interaction between quarks shown in the left side of Figure 1.2 can be represented by varied form of gluons and quarks.

When the bare coupling constant (the first term of the right side in Figure 1.2) is defined as g_0, the effective coupling constant g ($\alpha_s = g^2/4\pi$) can be described by as follows:

$$g = g_0 + g_0^3 \cdot b_3 + g_0^5 \cdot b_5 + \cdots ,$$

where the b_3 and b_5 are coefficients. Because the sum has a singularity after accumulating all the higher orders, the equation needs to be renormalized by an

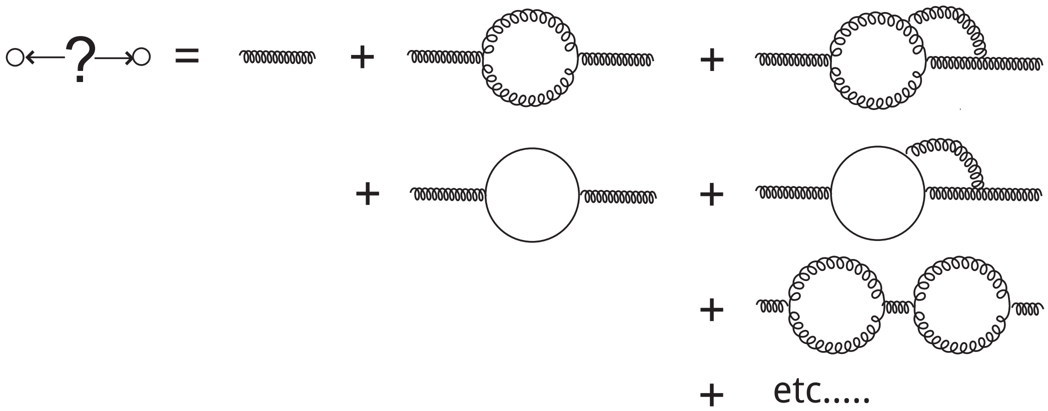

Figure 1.2: *Interaction between two quarks can be described with the bare coupling constant with the higher order diagrams.*

arbitrary scale, the renormalization scale (μ_R). The effective coupling constant can be expressed as following:

$$g = g_0 \cdot Z(\mu_R)\ .$$

The renormalization scale represents a subtraction of ultraviolet divergences.

1.1.2 pQCD in Hadron Collisions

The particle production in high energy hadron collisions can be factorized into three parts. The Figure 1.3 represents a schematic view of the factorization in $1 + 2 \rightarrow 3 + X$ reaction.

It is not necessary to restrict that a parton has zero transverse momentum relative to the initial and final hadron because of the gluon radiation shown in Figure 1.1(A). A soft parton with small transverse momentum results in so called collinear divergence in the small limit of the total momentum. A factorization scale(μ_F) is employed to regulate the divergence. It can be thought of as an arbitrary scale which separates the long (soft) and short (hard) distance physics. A parton with smaller transverse momentum than the scale is considered as a part of initial or final hadron structure. The cross section of the hadron production is expressed as following:

$$\begin{aligned} \sigma_{1,2}^{3} &= \sum_{i,j,k} \int dx_i dx_j dz_k \cdot f_1^i(x_i, \mu_F) \cdot f_2^j(x_j, \mu_F) & (1.1) \\ & \quad \times \sigma_{i,j}^{k}(p_i, p_j, p_k, \alpha_s(\mu_R), Q^2/\mu_R, Q^2/\mu_F) \times D_k^3(z_k, \mu_F)\ , \end{aligned}$$

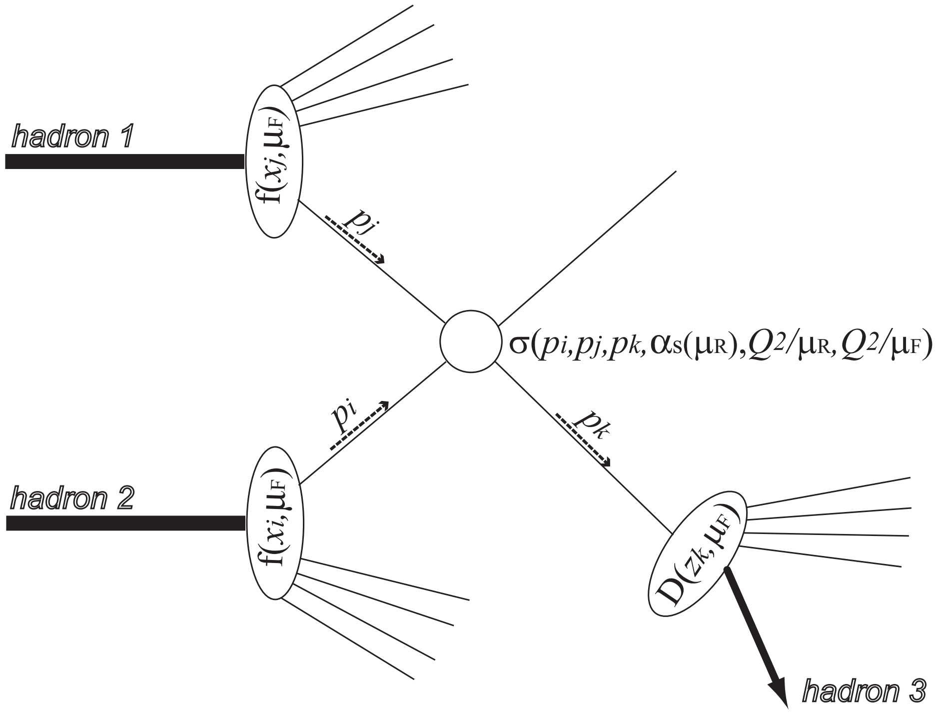

Figure 1.3: *Diagram for the hadron production in the hadron reaction of* 1+2 $\rightarrow$ 3.

where μ_F is the factorization scale, $f_1^i(x_i, \mu_F)$ is parton distribution function (PDF) of i parton in 1st hadron, $f_2^j(x_j, \mu_F)$ is PDF of j parton in 2nd hadron, $D_k^3(z_k, \mu_F)$ is fragmentation function (FF) from k parton to 3rd hadron, x is the momentum fraction of the initial parton in the initial hadron, z is the momentum fraction of the final hadron in the final parton, and x and z are the momentum fraction of the initial and final parton in the initial and final hadron, respectively,

p_i, p_j, and p_k are the momentum of i, j, and k parton, Q^2 is the momentum transfer, and $\sigma_{i,j}^k(\cdots)$ represents the cross section from two partons (i and j) into a parton (k).

As mentioned in the previous section, the coupling constant, α_s, depends on the renormalization scale (μ_R). The both renormalization and factorization scale are arbitrary and are frequently assumed to be equal. Then the cross section of the hadron production can be simplified as

$$\begin{aligned}\sigma_{1,2}^3 &= \sum_{i,j,k} \int dx_i dx_j dz_k \cdot f_1^i(x_i, \mu) \cdot f_2^j(x_j, \mu) \\ &\qquad \times \sigma_{i,j}^k(p_i, p_j, p_k, \alpha_s(\mu), Q^2/\mu) \times D_k^3(z_k, \mu) \ ,\end{aligned}$$

where μ is defined as $\mu \equiv \mu_R = \mu_F$.

Because the cross section must not depend on such the arbitrary scales,

$\mu\frac{d\sigma_{1,2}^{3}}{d\mu} \equiv 0$ is required. Although the optimization of the scale is discussed in several theoretical publications [7], one of the largest uncertainties on the calculation is from choice of the scale.

Parton Distribution Function (PDF) The proton structure function ($F_2(x, Q^2)$) is initially measured by lepton deep inelastic scattering (DIS) during the last decade in many experiments; electron scattering at Stanford Linear Accelerator Center (SLAC) [8] and by H1 [9] and ZEUS [10] at Deutsches Elektronen-Synchrotron (DESY) and muon scattering by BCDMS [11], E665 [12], EMC [13], and NMC [14]. In addition to the lepton, neutrino-nucleus scattering is another probe for $F_2(x, Q^2)$ measured by CCFR [15]. An example of the measured $F_2(x, Q^2)$ over the wide (x, Q^2) range are shown in Figure 1.4 [16]. The $F_2(x, Q^2)$ shows Q^2-scaling behavior in the middle of x region, however in the lower x, the scaling is violated due to the evolution.

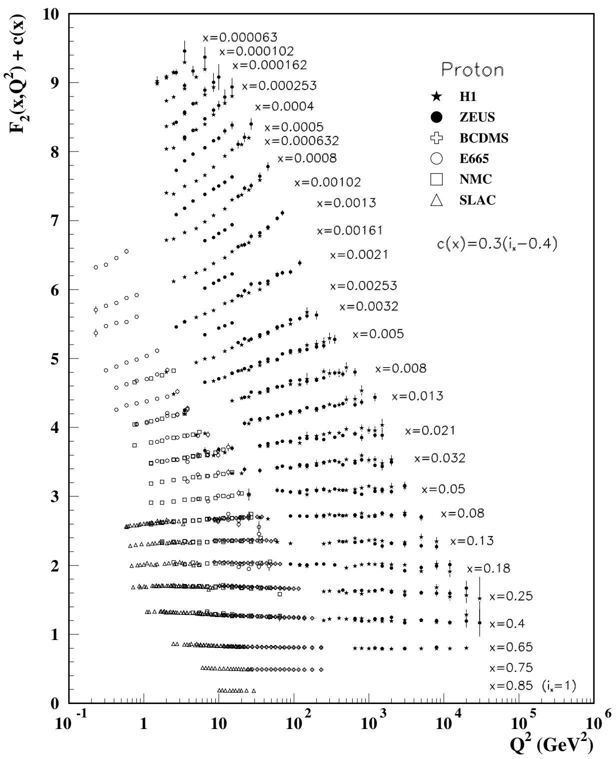

Figure 1.4: *Proton structure function $F_2(x, Q^2)$ measured by H1 [9] and ZEUS [10], BCDMS [11], E665 [12], NMC [14], and SLAC[8].*

The ratio of two parton distribution functions are constrained by other measurements. The ratio of $\overline{d}/\overline{u}$ is extracted from the ratio of lepton pair Drell-Yan production in p+p and p+d collisions measured by NA51 [17] and E866 [18], and the ratio of d/u is extracted from the asymmetry between $W \to l^{\pm}\nu$ measured by CDF [19]. The inclusive jet production[20, 21] and direct photon production[22] can provide another constraint on the PDF.

Several theoretical groups [23, 24, 25, 26] have tried to extract the parton distribution function. An example of the global analysis based on the NLO pQCD calculation is shown in Figure 1.5 by the CTEQ [24] group. The further global analysis including systematic error estimate [27, 28, 29] or next-to-next-to-leading-order (NNLO) correction [26, 30] have been performed recently.

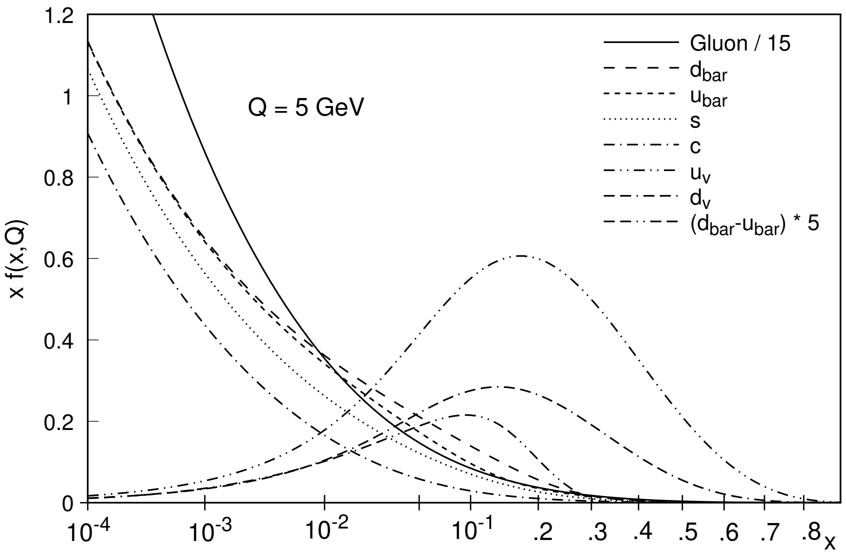

Figure 1.5: *Parton distribution function by the CTEQ [24] group as a function of x at Q=5GeV.*

Fragmentation Function (FF) The fragmentation function, $D_p^h(z, Q^2)$ is measured by $e^+ + e^-$ collisions in wide range of $\sqrt{s}$ from 3GeV to 183GeV at KEK [31], DESY [32, 33, 34], SLAC [35, 36], and CERN [37, 38, 39]. The undergoing process is $e^+ + e^- \to \gamma\ or\ Z \to h + X$.

Several pQCD theoretical works have been performed with leading order (LO) [40] and next-to-leading-order (NLO) for hadrons [41, 42, 43, 44] and photons [45] production. The fragmentation from gluon are achieved in 3-jet process, $e^+ + e^- \to q + \bar{q} + g$. Because of lack of the statistics in high z region, one of large uncertainties remained in the determination of the fragmentation from gluon.

1.1.3 Experimental Overview

In this section, we give a short summary of history of the π^0 measurement at pseudo-rapidity (η) of around 0 in the $p + p$ and $p + \bar{p}$ collisions during past 30 years together with a short summary of next-to-leading-order (NLO) pQCD calculation for the π^0 measurement.

In 1971, the intersecting storage rings (ISR) was built at CERN. Two rings were designed to be a collider of proton beam at the momentum from 8 to 31GeV/c. The measurement of π^0 were performed by SS [46], CCR [47], CCRS [48], Eggert. *et. al.*[49]. From the middle of 1970's, the ISR accelerator archived higher intensity in the p+p collisions. The R702 (CSS) [50], R108 (CCOR) [51], R110 (BCMOR) [52] R806 (ABCS) [53, 54], R807 (AFS) [55] measured the π^0 in the p+p and p+$\bar{\text{p}}$ collisions and also in $\alpha+\alpha$ collisions [56, 57]. The super proton synchrotron (SPS) with 2.2km diameter was constructed in 1977 at CERN to accelerate the proton beam at the maximum momentum of 450GeV/c. In 1981, the SPS was upgraded to S$p\bar{p}$S to accelerate the p and $\bar{p}$ beam as a collider. Between 1980s and 1990s, NA24 [58], WA70 [59], UA6 [60] measured the π^0 production in the fixed target and UA2 [61] measured in the $p+\bar{p}$ colliding mode. At Fermi National Accelerator Laboratory (FNAL), a proton synchrotron was constructed in 1972 to accelerate proton at the maximum momentum of 400GeV/c and was upgraded to Tevatron in 1987, where E268 [62], E704 [63], and E706 [64] measured the π^0 with the fixed target experiments.

An next-to-leading-order (NLO) pQCD calculation was introduced by F. Aversa *et al.* [65] initially and for the π^0 production by P. Aurenche *et al.* [66]. The NLO pQCD calculation for π^0 production have succeeded to describe the experimental data in wide range of $\sqrt{s}$ in hadron collisions. The uncertainty of the calculation is $\pm$ 50% level which are derived from the uncertainty on the factorization and renormalization scales.

This work, measurement of the π^0 production at $\sqrt{s}$ of 200GeV in proton+proton collisions, is very unique measurement, because it's the π^0 measurement at the highest $\sqrt{s}$ in the world as the proton-proton collisions. This work provides an ideal testing ground for the pQCD.

Origin of Nucleon Spin In a naive model, the nucleon spin of 1/2 can be factorized as following:

$$\frac{1}{2} = \frac{1}{2}\Delta\Sigma + \Delta G + \Delta L_Q + \Delta L_G \ ,$$

where $\Delta\Sigma$ and ΔG are the quark and gluon spin in the nucleon and ΔL_Q and ΔL_G are the quark and gluon orbital angular momentum in the nucleon.

The experimental study of the spin dependent structure function started at SLAC by E80 [67] and E130 [68] and was extended by EMC [69] with higher precision. New results in polarized deep inelastic scattering measured by E142 [70], E143 [71], and SMC [72] were essentially consistent with the EMC collaboration. A recent global analysis gives $\Delta\Sigma \approx 0.3$ which is apparently below the nucleon spin of 1/2. The measurement of the gluon polarization is the most important and immediate goal to understand the origin of the nucleon spin.

Because hadrons contain a lot of gluon, the polarized hadron collisions are a natural place to look for the effects of ΔG. We, the PHENIX collaboration, plan to measure the ΔG in the polarized proton-proton collisions through asymmetry of various particles [73] including the π^0 [74]. To evaluate the gluon polarization from the asymmetry of the π^0 production, the theoretical interpretation with pQCD is critical. This work, the inclusive measurement of the π^0, is a base for the future measurement of the asymmetry. The comparison of this work with the pQCD calculation is essential.

1.2 Quark Gluon Plasma (QGP)

As discussed in the previous section, the high energy hadron collision is one of ways to observe the behavior of quark and gluon although they are confined inside the hadron. Another way is to put hadrons into higher density and/or higher temperature condition. In such condition, the hadrons are expected to become a new state of matter called as quark gluon plasma (QGP). Figure 1.6 shows a phase diagram as functions of temperature and density. In higher temperature and density condition, the quark and gluon become free like plasma. A recent lattice calculation [76] results in that the transition temperature at zero baryon density is 170MeV.

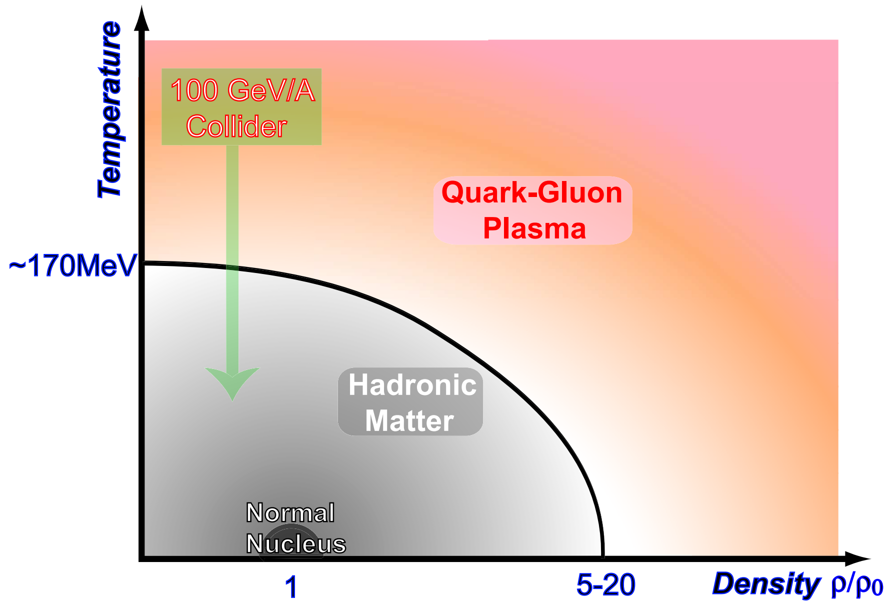

Figure 1.6: *Phase diagram as function of density and temperature. The RHIC is designed to search the QGP at low density and at high temperature.*

The QGP is also very attractive because it's known to be a state of matter in the early universe. Just before the hadron were formed, in 10^{-8} seconds after the big bang, the universe consisted of the melted soup of quarks and gluons. The experimental effort to find the QGP have been performed during the last decade in heavy ion collisions at the Bevatron, the Alternating Gradient Synchrotron (AGS), and the Super Proton Synchrotron (SPS) over wide range of $\sqrt{s}$ from a few GeV to 18GeV.

1.2.1 Jet Quenching as a Probe of QGP

The Landau Pomeranchuk Migdal (LPM) [77] effect is an interesting phenomenon which is introduced in QED. If an electron goes through a thin metal, the LPM effect predicts the photon radiation by bremsstrahlung decrease because the radiation length is smaller than the width of the thin metal. The prediction is confirmed experimentally [78, 79].

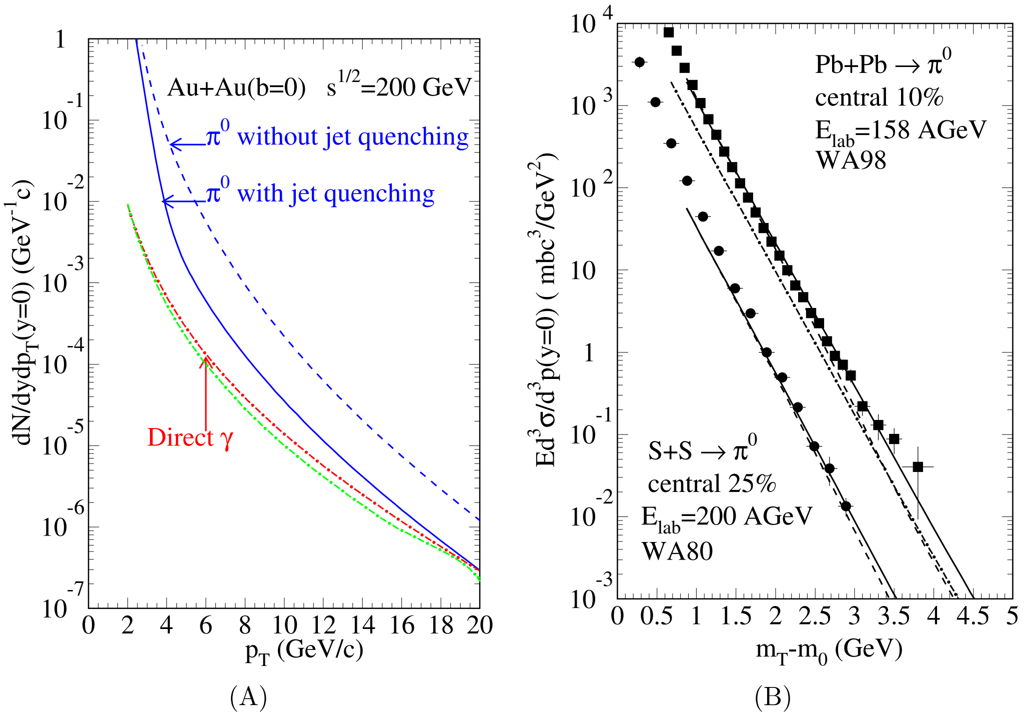

Figure 1.7: *(A)pQCD calculation [80] of π^0 and direct-photon production in Au+Au central collisions at $\sqrt{s}$=200GeV with and without jet quenching effect. The calculation predicts a large decrease of the π^0 yield in case of that the jet quenching effect exists. The upper (red) and bottom (green) line for the direct-photon production represents the calculation without and with the jet quenching effect, respectively. (B)Comparison with two experimental results by WA80 [81] and WA98 [82] and pQCD calculation [83] with (solid line) and without (dot-dashed line) the jet quenching effect. Also, the calculation without the jet quenching effect and without initial k_T smearing are shown (dashed line) together. The data can be described well by pQCD calculation with the initial k_T smearing and without jet quenching effect.*

The secondary interaction between the produced parton with large transverse momentum and the remnant material is useful probe [84] to study the status of the remnant material. In QCD, a similar effect [85] as LPM effect, which is named as jet quenching effect, is predicted through color bremsstrahlung. The

QCD calculations [80, 86, 87] predict that a parton loses its energy when it goes through the QGP matter. Figure 1.7 (A) shows one of the predictions in Au+Au collisions at $\sqrt{s} = 200$GeV with and without the effect in π^0 and direct photon production. The yield of π^0 is predicted to decrease by a factor of 5 at p_T of 10GeV/c.

The inclusive π^0 production in the heavy-ion collisions were measured in the past experiments at p_T up to 4GeV. Figure 1.7 (B) shows comparison between a pQCD calculation [80] and experimental results; π^0 production in S+S 10% central collisions at $E_{lab} = 200$AGeV($\sqrt{s_{NN}}$=14.1GeV) by WA80 [81] and in Pb+Pb 10% central collisions at $E_{lab} = 158$AGeV($\sqrt{s_{NN}}$=12.6GeV) by WA98 [82]. Both results are described well by the pQCD calculation without jet quenching effect and with the initial k_T smearing. This fact indicates that the jet quenching effect has not been observed at these energies.

If the jet quenching effect occurs in the collisions, the inclusive π^0 yield will decrease by a factor of 5 as shown in Figure 1.7 (A). At PHENIX experiment, we have studied and reported the high p_T π^0 and charged hadron production from Au+Au collisions at $\sqrt{s}$ of 130GeV [88]. The Au+Au collisions can be described as an incoherent superposition of the p+p collisions as predicted in the Glauber model [89]. The yield in Au+Au central and peripheral collisions were multiplied by factors ($< N_{binary} >$) predicted by the Glauber model and compared. The measurement of the ratio between central and peripheral collisions with the same detector reduced some systematic errors. Although the systematic uncertainty of the ratios was large of about 40%, we have observed the ratio is 30-50% for π^0 production and 50-90% for charged hadron production as shown in Figure 1.8.

We, the PHENIX collaboration, have measured the high p_T π^0 and charged hadron at $\sqrt{s}$ of 200GeV [90]. The large uncertainty of 30% in the analysis for 130GeV was due to the large uncertainty in the peripheral collisions. To reduce the uncertainty, we will compare the π^0 yield with p+p collisions. The motivation of this work is to provide a reference data of p+p collisions at $\sqrt{s}$ of 200GeV. This work is essential to conclude the quenching effect in Au+Au collisions for the QGP search.

In Chapter 2, we will introduce the setup of the PHENIX experiment. Since the PHENIX electro-magnetic calorimeters (EMCal) and the high-p_T trigger are essential for the π^0 measurement, we will focus on the detailed performance of the EMCal and the structure of the high-p_T trigger. In Chapter 3, we will describe the detailed procedure of the π^0 analysis. The results together with the systematic uncertainty are shown and discussed with in Chapter 4. In Chapter 5, we will conclude this work.

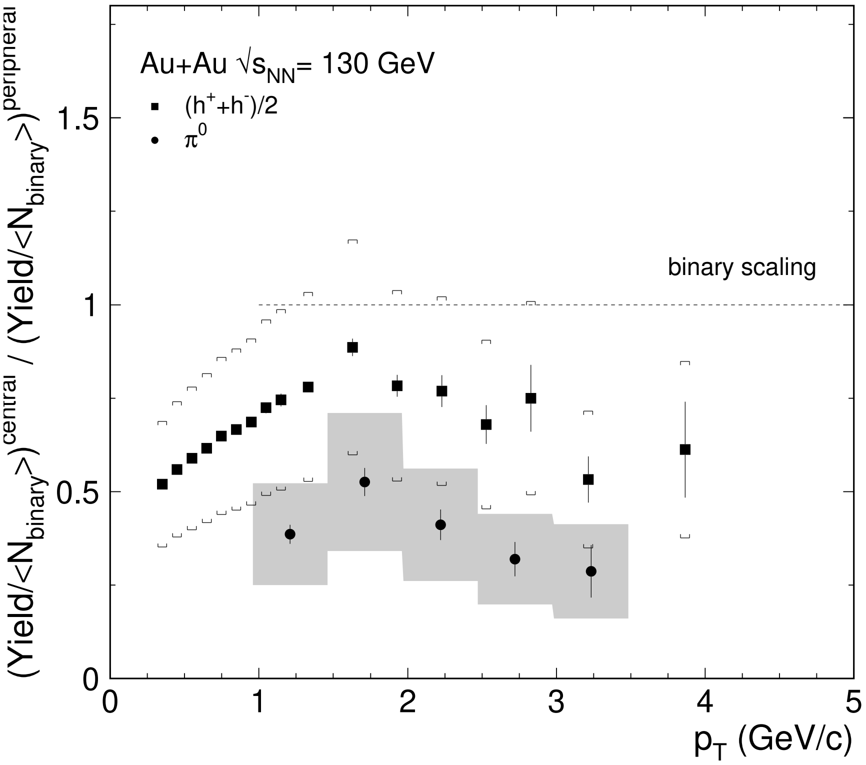

Figure 1.8: *Ratio of yield per event in central vs peripheral Au+Au collisions, with each divided by* $< N_{binary} >$ *for that class. The error bars indicate the statistical errors on the spectra. The shaded area for* π^0*'s and the brackets for* $(h^+ + h^-)/2$ *are the quadrature sums of the systematic errors that do not cancel in the ratio and the uncertainty in* $< N_{binary} >$.

Chapter 2

Experimental Setup

2.1 Overview of the Apparatus

The Relativistic Heavy Ion Collider (RHIC) [91] was proposed in 1990 initially and built in the Brookhaven National Laboratory (BNL) in the United State. The Pioneering High Energy Nuclear Interaction eXperiment (PHENIX) for heavy-ion physics at RHIC has started in the early summer of 2000, that for spin physics has started in 2001. The RHIC is designed to accelerate polarized proton at the maximum energy of 250GeV and heavy ion at that per nucleon of 100GeV The polarized proton and heavy ion produced at the source are transported through a proton linac and Tandem-Van-de-Graaff, respectively, and accelerated in 3 synchrotron: the booster accelerator, the Alternating Gradient Synchrotron (AGS) at 25GeV/c for proton and 9GeV/c for Au ion, and RHIC ring at the maximum energy. The RHIC ring has the total length of 3.8km with the maximum bunch of 120 and the designed luminosity is $2 \times 10^{26}\mathrm{cm}^{-2}s^{-2}$ for Au ion and $2 \times 10^{32}\mathrm{cm}^{-2}s^{-2}$ for proton. The Figure 2.1 shows an overview of the 2 ion sources and 3 accelerators.

The PHENIX [92] is one of the large experiment build in one of 6 intersection point of two RHIC rings and consists of 2 central arms which has pseudo-rapidity coverage of ± 0.35 and $180°$ azimuthal angle in total, 2 muon arms which has pseudo-rapidity coverage of $\pm(1.2-2.4)$, and beam detectors which are specialized to make triggers and to measure the luminosity and the centrality in heavy ion collisions. The Figure 2.2 shows the bird-view of one of two central arms and one of muon arms. The Electro Magnetic Calorimeter (EMCal) is essential to measure the photons decaying from π^0. In this section, we quickly overview all the detectors on the central arms. Then, we explain the detail structure and performance of the EMCal.

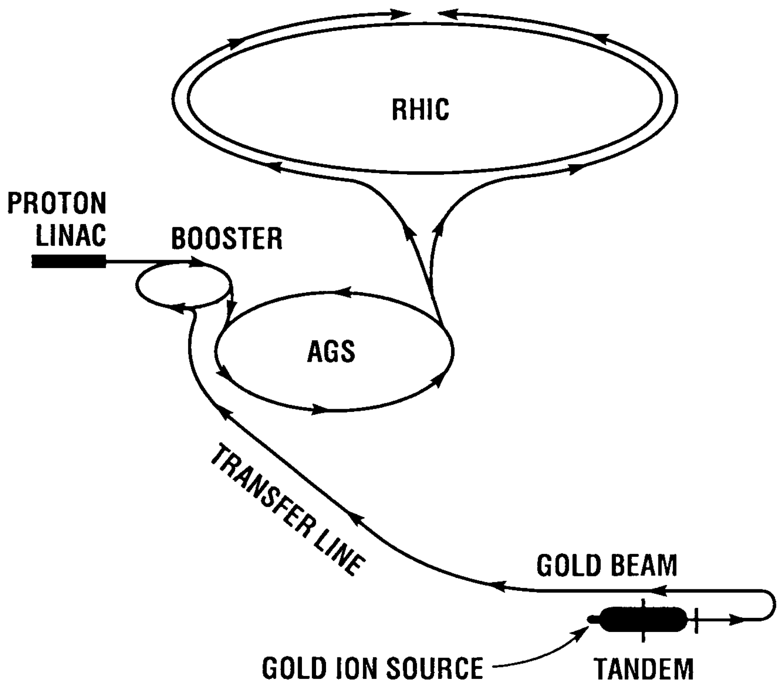

Figure 2.1: *Overview of RHIC. Two ion sources, LINAC and TANDEM for proton and nuclei respectively, and three synchrotron accelerators are shown. Two RHIC rings intersect each other at 6 points. The PHENIX is constructed in one of the 6 intersection points.*

2.2 Beam Detectors

In this section, the beam detectors [93] [94] used to trigger the events and to measure the luminosity and centrality for the Au+Au collisions are described.

2.2.1 Beam Beam Counters (BBC)

The beam beam counters (BBC) are placed at 1.4m along to the beam pipe from the nominal collision point and covers the pseudo-rapidity from 3.0 to 3.9. Each of them consists of 64 quartz Čerenkov counters, which each of the quartz has 3cm thickness. The BBC is designed to measure the number of charged particle produced by the collisions and to measure the collision vertex and collision time. The collision vertex and time are determined by the difference and average of the arrival time to north and south counters. Due to the limited coverage, only the 50% and 93% of the inelastic collisions can be triggered for p+p and Au+Au

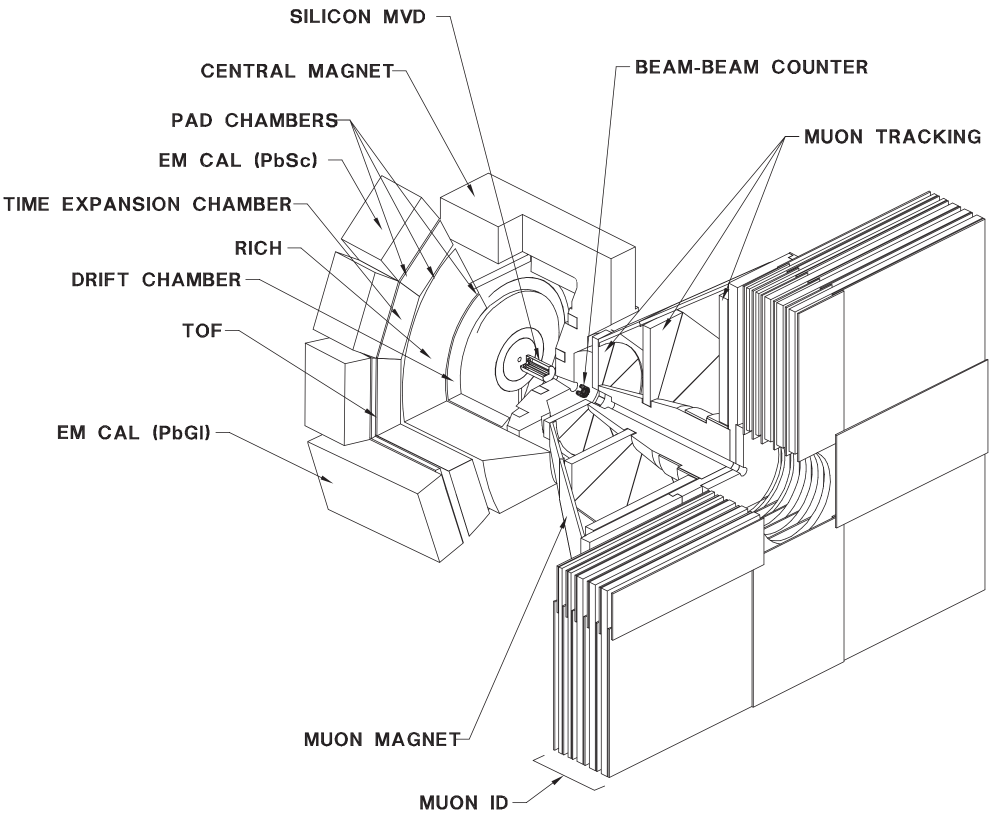

Figure 2.2: *Overview of PHENIX detectors with one of two central arms and one of two muon arms. See text for details of each detectors.*

collisions at $\sqrt{s}$ of 200GeV, respectively.

2.2.2 Zero Degree Counters

The zero degree counters (ZDC) are hadron calorimeter designed to measure the number of neutron from the collision, which are placed at 18m north and south from the nominal collision point. Because both north and south ZDC sit at just the upstream of the last bending magnet on the RHIC ring, most of the charged particles are swept out from the acceptance. Each of them is made of alternating tiles of plates of tungsten and layers of optical fibers. The direction of the plates and layers are tilted by 45° relative to the incident neutron direction to collect the Čerenkov light. Since only small fraction (about 1%) of inelastic p+p collisions are able to be detected, the ZDC is used only to measure the luminosity in heavy ion collisions and to reduce the systematic error of the luminosity measurement in p+p collisions.

2.2.3 Normalization Trigger Counters (NTC)

The normalization trigger counters (NTC) is made of scintillation counters designed to trigger the p+p collisions and to measure the luminosity of p+p collisions. The NTC consists of scintillation plates and is placed at 40cm apart of the north and south side from the collisions point. In this analysis, the NTC is used only to reduce the systematic error on the luminosity measurement.

2.3 Charged Particle Detection System in the Central Arms.

In this section, the detectors for charged particles [95, 96, 97] in the central arms is described quickly. The schematic view of all the detectors are shown in Figure 2.3. They are used only for the calibration of the Electro Magnetic Calorimeter (EMCal) in this work.

2.3.1 Magnet

The central magnet consists of inner coil and outer coil. They provide cylindrical magnetic field optimized to the different physics programs for central arms because of the two independent coils. During the run for this work, only the outer coils is activated and the integrated magnetic field is $0.7\,T\cdot m$. Due to the magnetic field, the charged particles with the momentum of less than 0.2GeV/c momentum are trapped in the field.

2.3.2 Photon Converter

The Photon Converter is placed at about 40cm distance from the vertex position and is made of brass with 1.7% radiation length. The purpose is to measure photon yield by tagging electron and positron pair through the pair creation process, $\gamma \rightarrow e^+ + e^-$. and is to study the non-photonic source of lepton. By comparing yield of the lepton with and without the Photon Converter, we can separate non-photonic and photonic source of electron and positron. During run 2001–2002 for this work, the Photon Converter were installed and pulled out in the middle of the run.

2.3.3 Drift Chamber (DC)

The Drift Chamber (DC) is placed between 2.02m and 2.46m in the radial distance from the nominal interaction point and consists of 3 different direction of the wire: same directions as the beam pipe and $\pm 6^\circ$ tiled angled relative to the beam pipe direction. The detector consists of 2 modules for each direction. A module consists of 4 or 12 anode wires depending on the wire direction. In total, 40 drift cells are located in different radii. The designed position resolution in a single wire is 0.15 mm and the two track resolution is 1.5mm.

2.3.4 Pad Chamber (PC)

The Pad Chamber (PC) consists of 3 planes; PC1 at 2.5m, PC2 at 4.1m, and PC3 at 5.0m apart from the beam pipe. The PC's are designed as a proportional chamber with readout of the cathode pads. Each pad has either 8.2x1.5mm^2 or 8.2x2.7mm^2 dimension. To prevent false hits caused by the electronic noise, three pads are read individually and gathered to compose a square cell, which covers a 8.4x8.4mm^2 area. The designed position resolution for the cell is $\pm$4mm. The purpose of the detector is to measure the charged multiplicity and to reduce the background in the sample of charged particles.

2.3.5 Ring Image Čerenkov Counters (RICH)

The Ring Image Čerenkov Counters (RICH) is designed to identify the electron, positron, and high p_T charged particle. Each of the detectors in the east and west arms has a volume of roughly $40m^3$ and minimum thickness of 87cm of the pressured gas, which is CH_2, N_2, or CO_2 gas depending on the run periods. During run 2001–2002 for this work, CO_2 gas was used. The Čerenkov photons produced in the pressured gas are reflected on the mirror and are detected by the photo multiplier tubes (PMT's). The average size of the Čerenkov ring is 8cm and the average number of the Čerenkov photons produced by electron is 11 on the plane where the PMT's are sitting. The detector is also used to form a LVL1 trigger in order to enhance the electron, positron, and high p_T charged particle.

2.3.6 Time Expansion Chambers (TEC)

The Time Expansion Chambers (TEC) is sitting only in the east arm at the distance between 4.2 and 4.9m apart from the beam pipe. It consists of 6 cells with 3cm drift length in different radii. The drift time, position, and the pulse height are measured by the anode wires. This detector is designed to improve the momentum resolution at the higher p_T than 4GeV/c and to identify electron and positron using the energy loss information (dE/dx).

2.3.7 Time Zero Counters (TZR)

The Time ZeRo counters (TZR) consists of 8 scintillator slats of 100x8x17.5cm^3 and 3mm thick scintillator for conversion rejection. The purpose is to measure the collision time.

2.3.8 Time Of Flight (TOF)

The Time Of Flight (TOF) consists of 960 scintillator slats which has 1.5cm width and 1.5cm depth. It covers 45° in the azimuthal angle. The designed time resolution is 100 psec. The TOF has capability to identify the charged π and K at p_T up to 2.5GeV/c.

2.4 Electro Magnetic Calorimeter (EMCal)

The Electro Magnetic Calorimeter (EMCal) [98] plays an important role in detecting photons coming from π^0 decay. In this section, the overview of the EMCal system, the detailed specification, and the basic performance are described.

2.4.1 Overview of EMCal

In PHENIX, the electro-magnetic calorimeter (EMCal) [98] is the primary tool for measuring photons, electrons, and positrons. In order to cover topics in physics programs, for example a thermal photon measurement in relativistic heavy ion collisions, and prompt photon, π^0 and weak boson measurements in polarized

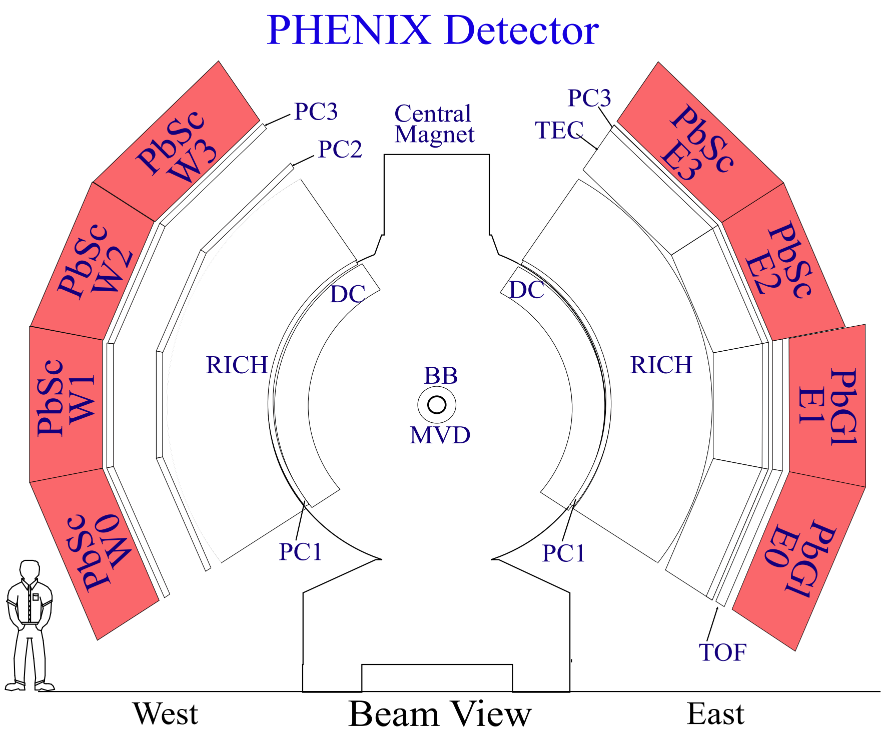

Figure 2.3: *Overview of EMCal system.*

proton collisions, the EMCal needs to cover a wide energy range extending from a few hundred MeV to 80GeV. A goal of the physics program is to measure differential cross sections of prompt photon and π^0's to an accuracy of 10%. A 2% accuracy in the calorimeter energy scale is required to achieve this for p_T more than 10GeV/c of interest, because the cross sections fall steeply.

The EMCal is originally designed for relativistic heavy-ion physics. There are two kinds of calorimeter in the PHENIX detector. One is a shashlik [99, 100, 101] type lead–scintillator sampling calorimeter (PbSc) and another is a lead glass calorimeter (PbGl). Table 2.1 shows their basic parameters. A super-module is composed of 12×12 channels for the PbSc and 4×6 channels for the PbGl. The one channel is named as tower. A sector is composed of 18 super-modules for the PbSc and 192 super-modules for the PbGl covers a $2m \times 4m$ plane area approximately. The 4 PbSc sectors and the 2 PbGl sectors are installed in the end of PHENIX central arms as shown in the Figure 2.3. From the bottom to the top sectors in the west and east arms, each sector is named as from W0 to W3 and from E0 to E3 sectors respectively. The total EMCal system in the PHENIX detector consists of the 108 PbSc super-modules and the 384 PbGl super-modules, i.e. the 15552 PbSc towers and the 9216 PbGl towers. The detailed structure of both PbSc and PbGl are described next.

		PbSc	PbGl
radiation length (X_0)	[mm]	21	29
Moliere radius	[mm]	∼30	37
channel			
cross section	[mm^2]	52.5×52.5	40×40
depth	[mm]	375	400
	[X_0]	18	14
η coverage		0.011	0.008
ϕ coverage		0.011	0.008
super-module			
number of channels		144 (12×12)	24 (4×6)
sector			
number of super-modules		18 (3×6)	192 (12×16)
total system			
number of sectors		6	2
number of channels		15552	9216
η coverage		0.7	0.7
ϕ coverage		90°+45°	45°

Table 2.1: *Basic parameters of two kinds of PHENIX EMCal.*

Lead Scintillator Calorimeter (PbSc) The PbSc is a shashlik type sampling calorimeter made of alternating 65 lead tiles and 66 scintillator tiles whose thickness are 4.0mm and 1.5mm, respectively. The basic block is a module consisting of four towers, which are optically isolated, and are read out individually. The tower has $5.52 \times 5.52\text{cm}^2$ cross section and 37.5cm in length. Figure 2.4 depicts the internal view of the module. The 64 holes with 1.2mm diameter are placed on both lead and scintillator tiles. The spacing between holes is 9.27mm. The 32 read-out fibers made with wave length shifter (0.5% POPOP) pass through the entire tower from one edge to the other and return to the first edge after following smooth curves. The both edges of the 32 fibers are gathered into a PMT. The attenuation length of the fiber is approximately 1m, which affects the linearity of the energy measurement.

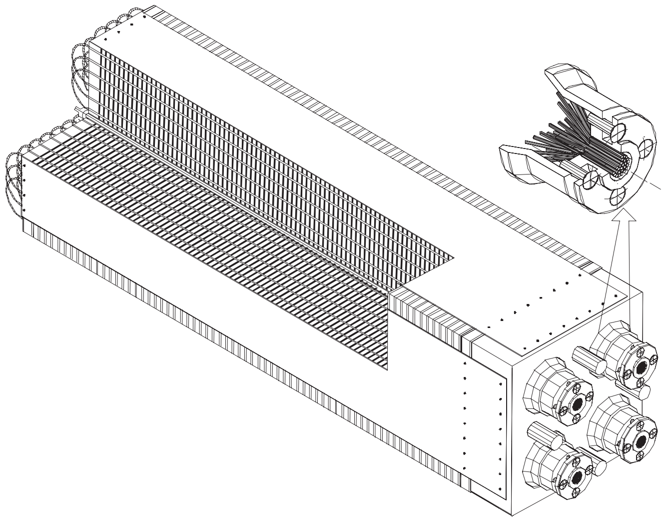

Figure 2.4: *Overview of one module of the PbSc EMCal.*

The 4 edges of the scintillator tiles are coated by aluminum to reflect the scintillation light except one corner. The transparent corners of the 4 towers are placed in the center of the module. For the purpose of the calibration, a leaky fiber, which simulates the real photon shower shape, is inserted in the center of the module and provides laser light into 4 towers through the corners. Figure 2.5 shows the entire schematic of the laser calibration system [102]. The laser light are split by 3 steps and delivered into 3888 modules in total. The laser amplitude is monitored by a phototube and photo diodes in all the light splitters. The purpose of this laser calibration system is to normalize the initial energy calibration, which has been obtained by utilizing cosmic ray for all towers during construction, by accounting of that the operation condition has changed from the time of construction and to measure the gain drift during the data taking. The gain of the amplifier for the photo diodes is monitored by test pulses.

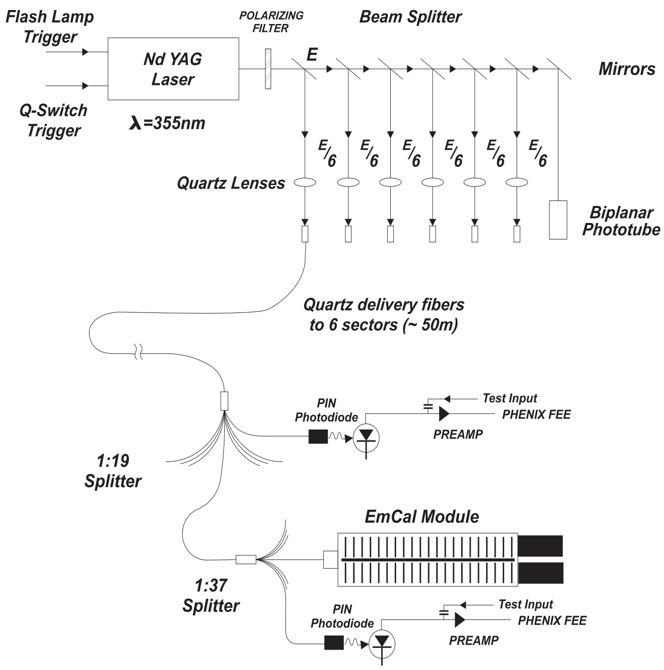

Figure 2.5: *Overview of the PbSc laser calibration system [102].*

Lead Glass Calorimeter (PbGl) The PbGl is a Čerenkov type calorimeter. A lead glass has 4.0×4.0 cross section and 40cm length, we name this element as tower. The entire array comprises 9216 tower previously used in WA98[82] experiment at CERN. The PbGl has a nominal energy resolution of $6\%/\sqrt{E}\mathrm{GeV}$ and intrinsic timing resolution of better than 300psec. Figure 2.6 shows the internal view of one super-module, composed by 4x6 towers. The towers within the super-module are individually wrapped with aluminized mylar foil and shrink tube and are isolated optically. Steel sheets of 0.5mm thickness are used to house the entire towers and phototubes.

To monitor the gain drift, the PbGl LED calibration system are installed. The three LEDs with different wave length are placed on the front of every super-module. An aluminized foil on the front of the SM contains a hole for each tower that allows entry for the LED light. A polystyrene reflective dome encloses the LED system on the front surface of the SM.

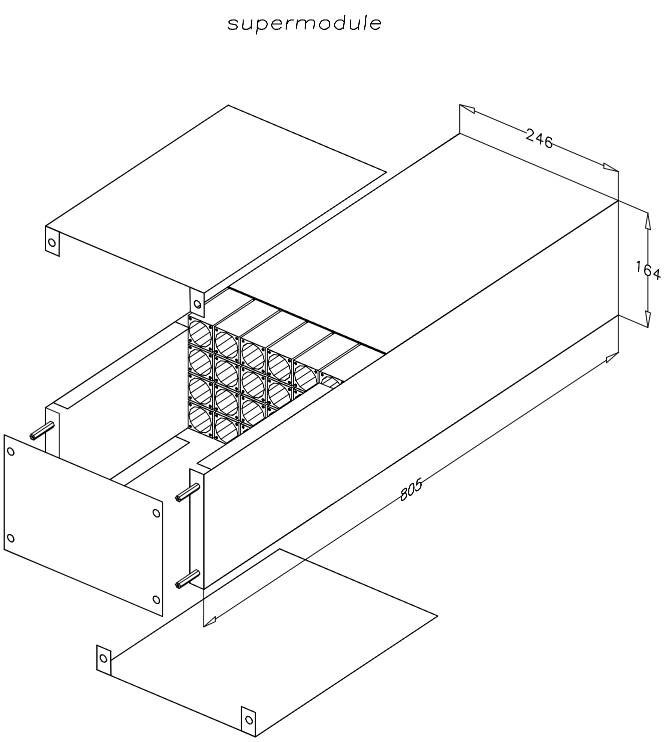

Figure 2.6: *Overview of one super-module of the PbGl.*

2.4.2 Basic Performance of PbSc

The basic performance, energy resolution, linearity and hadron rejection has been measured at BNL in the energy range up to 7GeV [103]. In order to extend these measurements to the energy range up to 80GeV, a beam test [104] has been performed at the CERN H6 beam line in 1998. In this section, we summarize the basic performance of the PbSc measured at the both tests.

Energy Resolution The energy resolution is obtained using electron and positron beam with the well-calibrated momentum. Figure 2.7 shows the energy resolution obtained by both beam tests at CERN and BNL. They can be fit with linear or quadratic expressions. Only statistical errors are taken into account in the fits. We estimate an additional 1% systematic error based on the reproducibility of the measurements at each energy point. The results of the fits are

$$\begin{aligned}\sigma_E/E &= 1.2\% + \frac{6.2\%}{\sqrt{E(\mathrm{GeV})}}\ , \text{ and} \\ &= 2.1\% \oplus \frac{8.1\%}{\sqrt{E(\mathrm{GeV})}}\ ,\end{aligned}$$

where $\oplus$ denotes a root of the quadratic sum, $\alpha \oplus \beta = \sqrt{\alpha^2 + \beta^2}$. The angle dependence of the resolution is negligible. They are valid in the energy region of 0.5GeV to 80GeV with 1% systematic uncertainty.

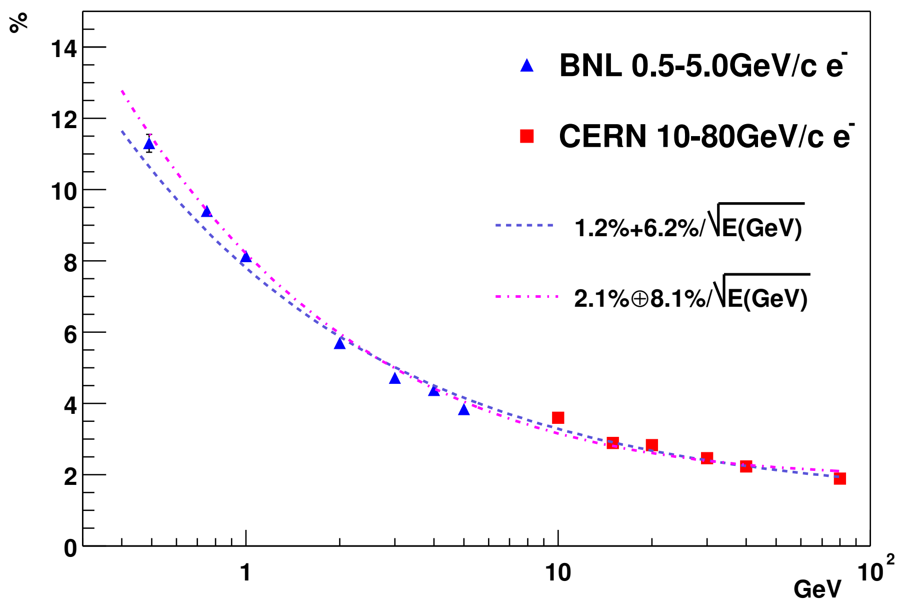

Figure 2.7: *Energy resolution obtained by both beam tests at BNL and CERN. A dashed line shows the result of fitting by a linear formula,* $\sigma_E/E = 1.2\% + 6.2\%/\sqrt{E(\mathrm{GeV})}$. *A dashed dotted line shows the result of fitting by a quadratic formula,* $\sigma_E/E = 2.1\% \oplus 8.1\%/\sqrt{E(\mathrm{GeV})}$.

Energy Linearity Figure 2.8 shows the measured energy with the PbSc divided by the beam energy as a function of the beam energy. The data point at the 10GeV from the CERN result seems to start deviate by 2% from those at more than 20GeV. This is investigated carefully for several possible source as follows The electronics that was used at the test beam has linear response within 1%. The linearity of the PMT is confirmed to be linear within 2% [105]. The shower leakage is evaluated to be 1% at 10GeV and 4% at 80GeV [106, 107] and is confirmed to be canceled by the effect of the light attenuation in the readout fiber. In total, we do not expect an intrinsic non-linearity to be as large as 2%. However, the point at the 10GeV/c is consistent with linear behavior within our systematic error obtained from run-by-run deviation. We conclude that the result is not inconsistent with the expectation within the systematic uncertainties in the energy region from 10GeV to 80GeV.

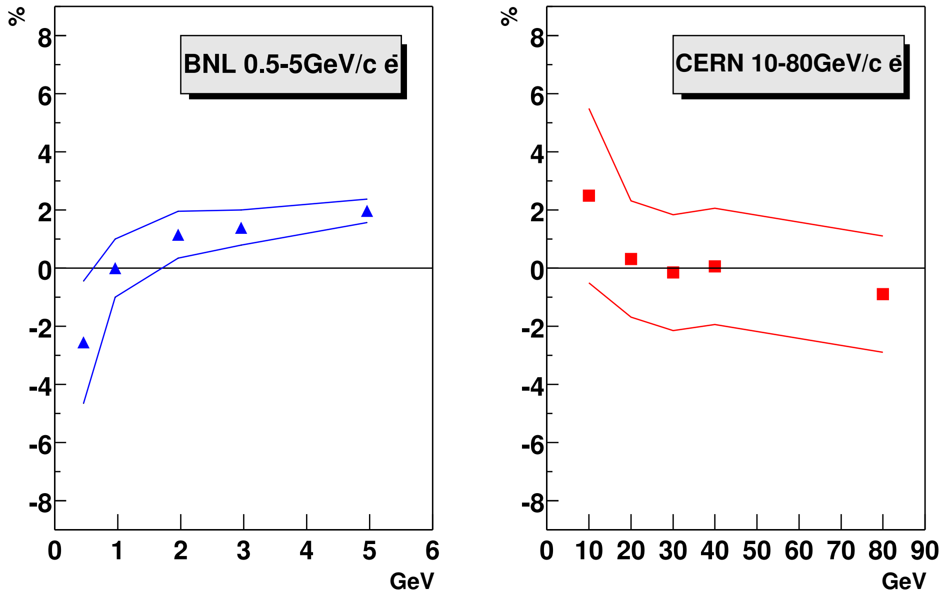

Figure 2.8: *Linearity for both beam tests at BNL (left) and CERN (right). The Solid lines show total systematic uncertainties in the analysis.*

Position Resolution Using electron and positron with the well-known impact position on the surface of the EMCal in the test beam, the position resolution is evaluated with the logarithmic method [108]. Figure 2.9 shows the position resolution obtained from both beam tests at CERN and BNL. The points can be fitted by a formula:

$$\sigma_x(\mathrm{mm}) = 1.4(\mathrm{mm}) + \frac{5.9(\mathrm{mm})}{\sqrt{E(\mathrm{GeV})}} \ .$$

Since most particles enter the calorimeter at an oblique angle, an additional term of

$$20.0 \cdot \sin(\theta) \quad [\mathrm{in\ mm}] \ ,$$

is estimated from the GEANT [109] simulation and the AGS test beam, and is added in quadrature to the resolution, where θ is the incident angle of the particle in the surface of the calorimeter.

Efficiency of Positron and Rejection of Charged $\boldsymbol{\pi}$ PHENIX plans to measure the leptons decaying from the W boson for the spin physics. Because the mass of the W boson is 80GeV, the momentum of the leptons become roughly

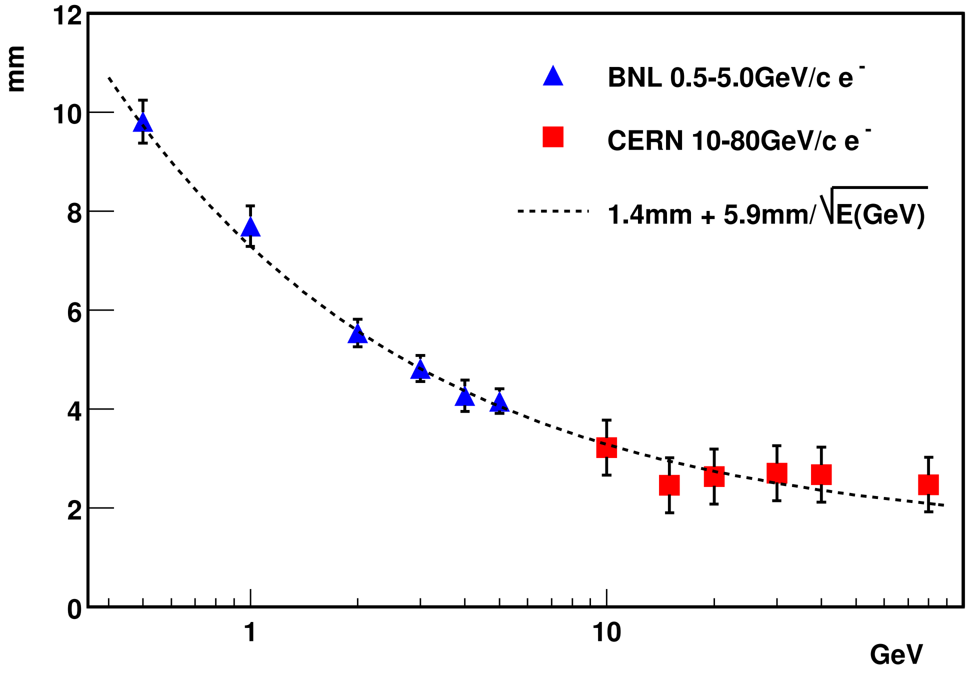

Figure 2.9: *Position resolution obtained by both beam tests at BNL and CERN. A dashed line shows the result of fitting, 1.4 mm + 5.9 mm /* $\sqrt{E(\text{GeV})}$.

40GeV/c. In such higher energy, the shower leakage behind the calorimeter needs to be considered. Another consideration is about the background predicted to be caused by mis-identified charged π mainly. These two considerations are strongly related to the length of the calorimeter, specifically to the radiation length and the nuclear interaction length. The calorimeter with longer length would be favored in terms of reducing the shower leakage, however, would be affected more by the hadronic shower of charged π. The efficiency of the high energy positron and rejection of the charged π are investigated.

Figure 2.10 shows the efficiency for the 40GeV positron beam when we require the measured energy deposit is greater than E_{cut}, and the pion rejection power for the 40GeV π^+ beam obtained with the same cut. At the E_{cut} of 38GeV, the 90% of electron survive the criteria and the rejection power for the charged π with the momentum of 40GeV/c is 300. A simulation using this result and the expected momentum resolution results in that the EMCal will work well to reduce the main background contribution without loosing the signals from the W boson.

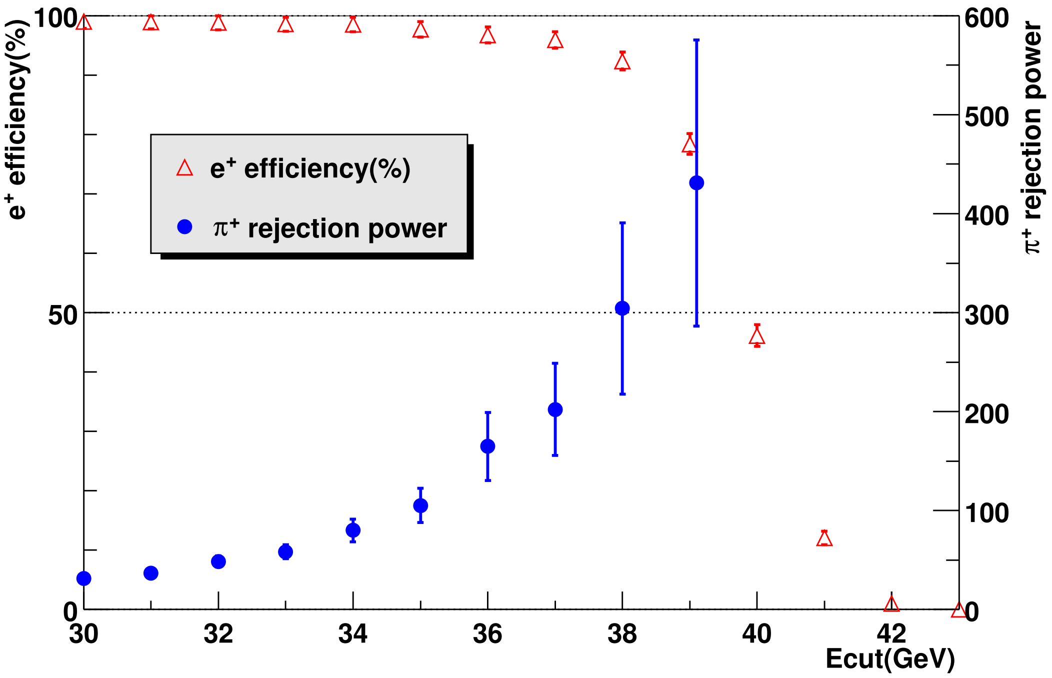

Figure 2.10: *Efficiency (open triangle) for the 40GeV positron beam when we require a measured energy deposit of more than E_{cut}, and the pion rejection power (closed circle) for the 40GeV π^+ beam obtained with the same cut.*

2.4.3 Clustering Algorithm

In the heavy-ion collisions, many photons, hadrons, and leptons hits on the EMCal. The maximum occupancy is about 15% for the PbSc in the central Au+Au collisions at $\sqrt{s}$ of 200GeV. In such extreme condition, the sum of the energy of all towers is easily affected by other clusters unlike at the test beam. For example, the observed ionization energy for the minimum ionizing particles increases by about 6% in central Au+Au collisions. Instead of taking all clusters for energy measurement, a new idea is proposed to sum only a few towers, which are named as "core" towers. This idea comes from the fact that about 80% of energy deposits on only one tower when a photon hit on the center of the tower. This technique of taking only the "core" towers enables EMCal to survive such an extreme condition in the heavy-ion collisions.

In the proton collisions, such a special treatment of the energy measurement is not necessary because the occupancy is low enough to separate clusters. However, to achieve the 2nd motivation of providing a reference point for QGP search, the same algorithm as in the heavy-ion collisions is favorable. The cluster algorithm for the "core" towers is described in this section.

First, the towers with more than a threshold are selected. The threshold is 10MeV for the PbSc and 15MeV for the PbGl. The towers which share at least same edge on each other are gathered into an isolated cluster. Such an isolated cluster might be composed of more than one shower. For this effect, more sophisticated cluster is defined by assuming that they are all photons, An isolated cluster is split into two "peak-area" clusters in the way that the number of "peak-area" clusters is equal to the number of local maximum in the isolated cluster. The energy of a tower within the 5x5 area from the two peaks is shared into the two "peak-area" clusters. in an iterative fashion using parameterized shower profile.

Then, the E_{core} energy is defined as

$$E_{core} = \sum_{i}^{core} E_i^{meas},$$

where E_i^{meas} is the measured energy in i-th tower and $\sum_i^{core}$ is defined as summing of the towers belonging to the "core" towers. The "core" towers are defined in the following condition:

$$\begin{aligned} \frac{E_i^{pred}}{E_{all}^{meas}} &> 0.02 \text{ , and} \\ E_{all}^{meas} &= \sum_{i}^{all} E_i^{meas}, \end{aligned}$$

where E_{all}^{meas} is the sum of measured energy in all towers belonging to the "peak-area" cluster, E_i^{pred} is the predicted energy using the shower profile in i-th tower. The averaged number of towers belonging to the "core" towers is 4 towers.

The E_{core} contains 91.8% energy of the total energy on average. The energy fraction of the E_{core} to the total energy depend on the incident angle, position, and energy. The dependence is studied by the GEANT simulation tuned by using the obtained performance [98] in test beam and corrected in the data analysis. The additional contribution on the energy resolution due to this clustering algorithm is estimated. It results in an additional constant term of 3%, which is larger than the nominal energy resolution of 2.1% as described in Section 2.4.2.

From the test beam data, it is known that, as the light generated by a shower travels from its source to the PMT via fibers, it is attenuated. Since the depth of the shower varies logarithmically with the energy, this attenuation gives rise to a non-linear energy response for particles as shown in Section 2.4.2. The non-linearity due to the attenuation in the fibers are corrected in the following form, $e^{x_0 \ln(E)/\lambda} = E^{x_0/\lambda}$, where $\lambda = 120$cm. The shower leakage are also estimated as 1% at 10GeV and 4% at 100GeV of photon. The correction of both effects are applied in the data.

2.5 Data Acquisition (DAQ) Systems

2.5.1 Overview of DAQ Systems

PHENIX is designed to make measurements on a variety of colliding systems from p+p to Au+Au. The occupancy in the detector varies from a few tracks in p+p interactions to approximately 15% of all detector channels in central Au+Au interactions. The interaction rate at design luminosity varies from a few kHz for Au+Au central collisions to approximately 500 kHz for minimum bias p+p collisions. The PHENIX DAQ system [110, 111] is designed to seamlessly accommodate improvements in the luminosity. This is accomplished through the pipelined and dead-time-less features of the detector front ends and the ability to accommodate higher-level triggers.

The wide range of event sizes and luminosities present special challenges for triggering and data acquisition. In PHENIX it is necessary to measure low-mass lepton pairs and low p_T particles in a high-background environment. In order to preserve the high interaction rate capability, a flexible triggering system that permits tagging of events is constructed. The DAQ system has two levels of triggering denoted as level 1 (LVL1) and level 2 (LVL2). The LVL1 trigger is fully pipelined. The buffering in the pipeline is sufficient to handle fluctuations in the event rate so that dead-time is reduced to less than 5% for full RHIC luminosity. The LVL1 trigger and lower levels of the readout are clock-driven by bunch-crossing signals from the 9.4 MHz RHIC clock. The higher levels of readout and the LVL2 trigger are data-driven where the results of triggering and data processing propagate to the next higher level only after processing of a given event is completed.

The general schematic for the PHENIX DAQ system is shown in Fig.2.11. Signals from the various PHENIX subsystems are processed by Front-end Electronics Module (FEM) that convert the analog signals into digital signals. This involves analog signal processing with amplification and shaping to extract the optimum time and amplitude information, development of trigger input data, and buffering to allow time for the LVL1 trigger decision and the digitization. This is carried out for all detector elements at every beam crossing synchronously with the RHIC beam clock. The timing signal is a harmonic of the RHIC beam clock and is distributed to the FEM's by the PHENIX Master Timing System (MTS). The LVL1 trigger provides a fast filter for discarding empty beam crossings and uninteresting events before the data is fully digitized. It generates a decision every 106 ns and has an adjustable latency of 40 beam crossings.

Once an event is accepted, the data fragments from the FEM's and primitives from the LVL1 trigger move in parallel to the Data Collection Modules (DCM). The only connection between the interaction region where the FEM's are located and the counting house where the DCM's are located is by fiber-optic cable. The DCM's perform zero suppression, error checking and data reformatting. Many

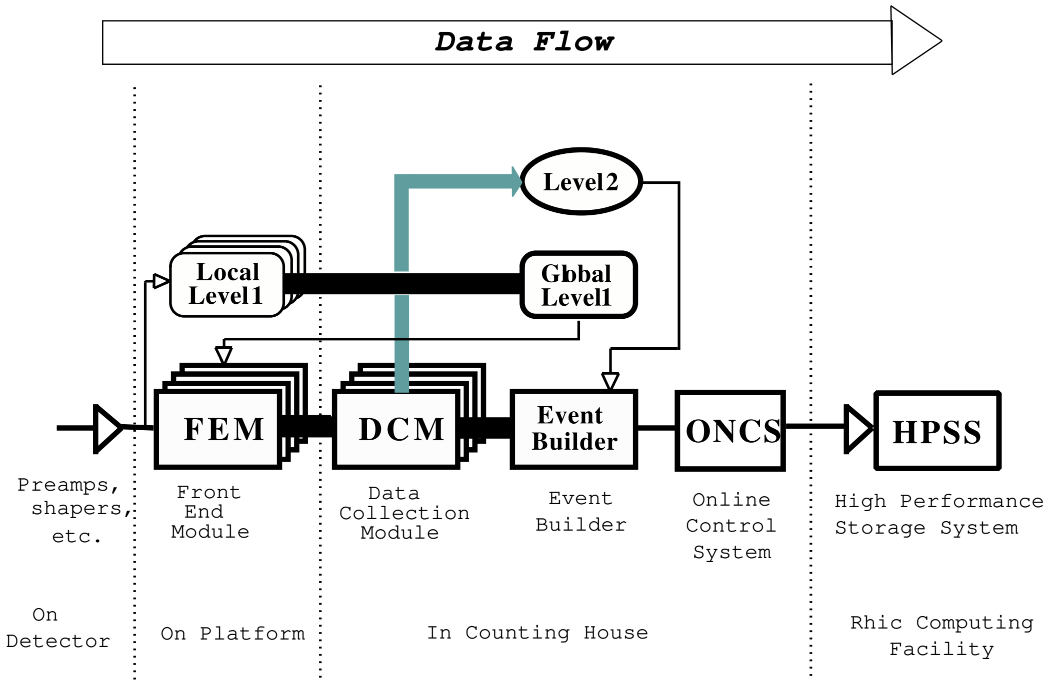

Figure 2.11: *Schematic diagram of the PHENIX DAQ system*

parallel data streams from the DCM's are sent to the Event Builder (EvB). The EvB performs the final stage of event assembly and provides an environment for the LVL2 trigger. In order to study the rare events, it is necessary to further reduce the number of accepted events by at least a factor of six. This selection is carried out by the LVL2 triggers while the events are being assembled in the Assembly and Trigger Processors (ATP) in the EvB. The EvB then sends the accepted events to the PHENIX On-line Control System (ONCS) for logging and monitoring made up by the linux computing farms. The logged data, which is named as PHENIX Raw Data File (PRDF), are send to the RHIC Computing Facility (RCF) for sinking on the tape in High Performance Storage System (HPSS). The data in the HPSS are analyzed and converted into an intermediated data format in the linux computer at RCF and Computing Center in Japan (CCJ).

2.5.2 Front-end Electronics Module for EMCal

The purpose of the Front-end Electronics Module (FEM) is to digitize analog signals from detectors and to buffer the data to allow for LVL1 trigger decisions. This involves analog signal processing with amplification and shaping to extract the optimum time and amplitude information, and development of trigger. The data is buffered for up to 40 beam crossings to allow for the time needed to make the LVL1 trigger decision. The FEM's process the data from the individual

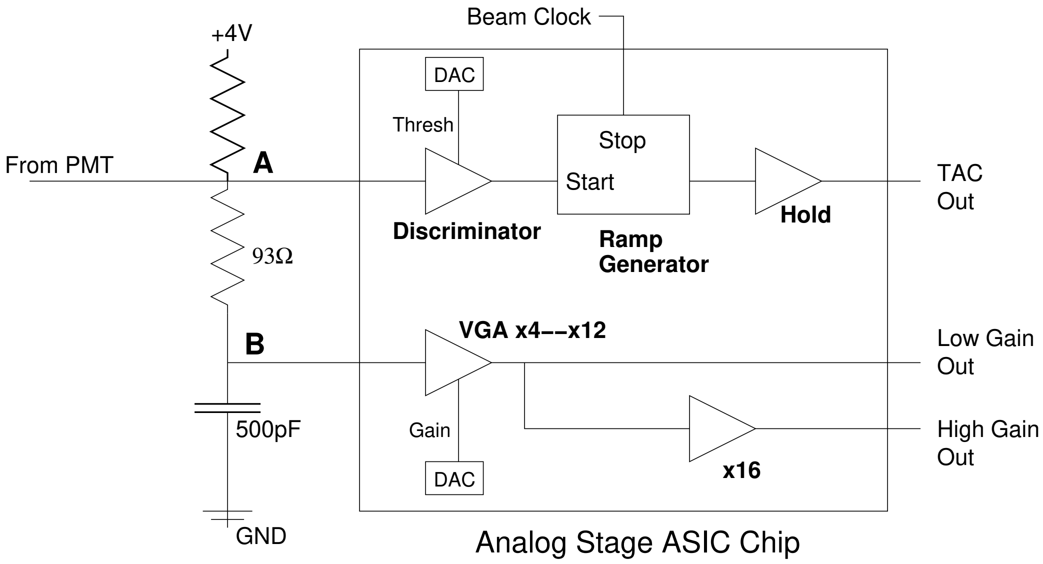

Figure 2.12: *Schematic view of one channel on the FEM circuit for EMCal.*

sub-detectors and send it to the DCM's for assembly.

Figure 2.12 shows the schematic view of one channel on the electric circuit of the FEM for the EMCal. The current from a PMT are terminated by 93Ω register and stored into the 500pF capacitance. The stored charge in the capacitance cause a decrease of the voltage from a reference voltage of +4V. The difference of the two voltages after and before the decrease are the target for the energy measurement. The decrease are amplified through the two steps of the amplifier for two outputs, low-gain and high-gain output. The both outputs are sampled and stored in analog form in 64-cell Analog Memory Units (AMU) on every clock.

The fast-shaped pulse is discriminated for starting the Time-to-Amplitude Converter (TAC). The output of the TAC stopped by clock is also sampled and stored in the AMU. After receipt of an accept from the LVL1 trigger, the sampled cells of before and after the voltage decrease are kept in AMU until an un-busy of the DCM and are digitized through Analog Digital Converter (ADC). The output from the low and high gain with the 12bits dynamic range cover the energy range up to roughly 1GeV and 16GeV, respectively. The dynamic range for the TAC is reduced to 10bit, where the 1 bit is roughly 35psec on average. In order to generate equalized signal for trigger, the gain of the first amplifier is adjustable, however, this adjustable feature was not used during RHIC 2001–2002 run.

The above feature are implemented in an application specific IC (ASIC). An ASIC board consists of the 6 ASIC's and 4 AMU IC's for every 24 channel. The 6 ASIC boards, *i.e.* 144 channels are implemented in a specific designed box with other controller board and trigger board. All boards include embedded firmware contained in Field Programmable Gate Arrays (FPGA's). The FPGA's functions of the controller board include accepting and delivering the RHIC timing from the Master Timing System (MTS) to the 6 ASIC boards and accepting the un-busy signal from DCM until transmittal of raw data packets. The programming of the FPGA is provided from a host computer through Attached Resource Computer Network (ARCNET).

2.5.3 Level 1 Trigger

During run 2001–2002, PHENIX has had two kinds of the level 1 trigger for the purpose of the π^0 measurement and for this analysis. One is minimum bias trigger which require at least one hit on one of the north and south BBCs. The other is the EMCal RICH level 1 Trigger (ERT) designed to enhance the electron, positron, pair of electron and positron, high-p_T charged particles, and π^0. The ERT is very critical for the measurement of the high-p_T π^0. For enhancement of the high-p_T π^0 samples, only the information of EMCal is used and the upper limit of the p_T range in this work is extended from approximately 6 GeV for the minimum bias triggers to 15 GeV. In this section, the EMCal's part of the ERT trigger are introduced.

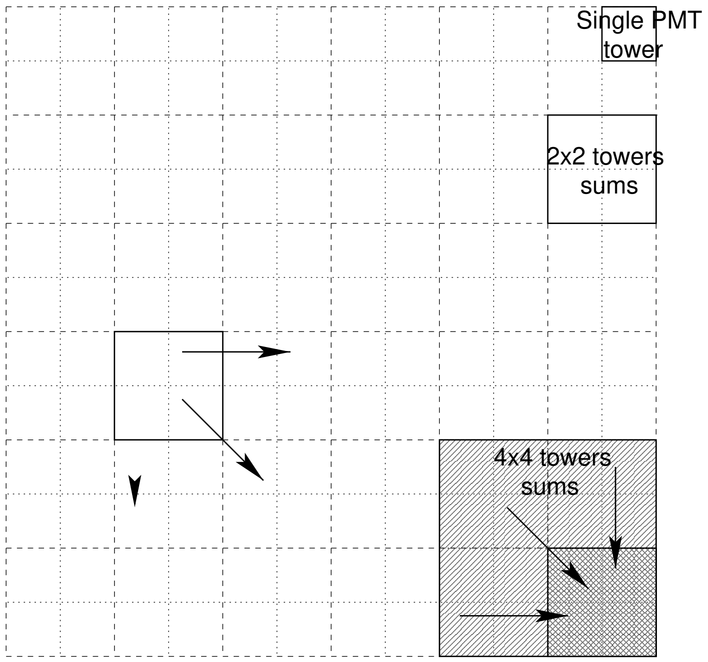

Figure 2.13: *Basic idea of ERT 2x2 non-overlapping and 4x4 overlapping trigger. The 4 analog signals from 2x2 towers are summed and used for 2x2 non-overlapping trigger. The 4 analog signals of the 4 2x2 towers are summed and used for 4x4 overlapping trigger. The two adjacent 4x4 sums overlap each other, unlike ERT 2x2 non-overlapping trigger.*

A photon deposits only the 23% and 81% of the energy in one tower when the photon hits on the corner and center of the PbSc's tower, respectively. For enhancing the high energy photon effectively, the summing procedure of more than one tower to obtain the more accurate energy is critical. The EMCal's level 1 trigger have two different methods as shown in Figure 2.13: 2x2 non-overlapping tower sum and 4x4 overlapping tower sum. The output of 2x2 towers are summed in the ASIC board and discriminated for the first method. The summed signal are transferred into the adjacent 2x2 towers and composes the 4x4 sums for the second method. The first one is mainly for the purpose of enhancing the cosmic ray event and low energy photon. In order to cover the wide range of p_T, three separate discriminators for 4x4 overlapping sums are implemented.

Figure 2.14 shows the schematic view of the electric circuit. After discriminating one level of the 2x2 sum and three different levels of 4x4 sum, the 36 digital signals for each level in a super-module are transmitted through the specific designed bus into a trigger board. When the number of valid signals out of 36 is higher than a specific number, the trigger board send a signal for a LVL1 decision for accepting the event. The specific numbers for the π^0 trigger are set as one except enhancing the cosmic ray event to perform the energy calibration. In case of that some of 36 signals become noisy during run, the transmittal of each 36 signal to the trigger board can be stopped. The signal for a LVL1 decision from a noisy super-module can be inactivated. During the run, the rate per event and the rejection power of each trigger from all super-modules are monitored in the ONCS computer and the noisy components of the trigger are inactivated. All the parameters and the inactivation of the outputs are programmable from a main computer as mentioned in the previous section.

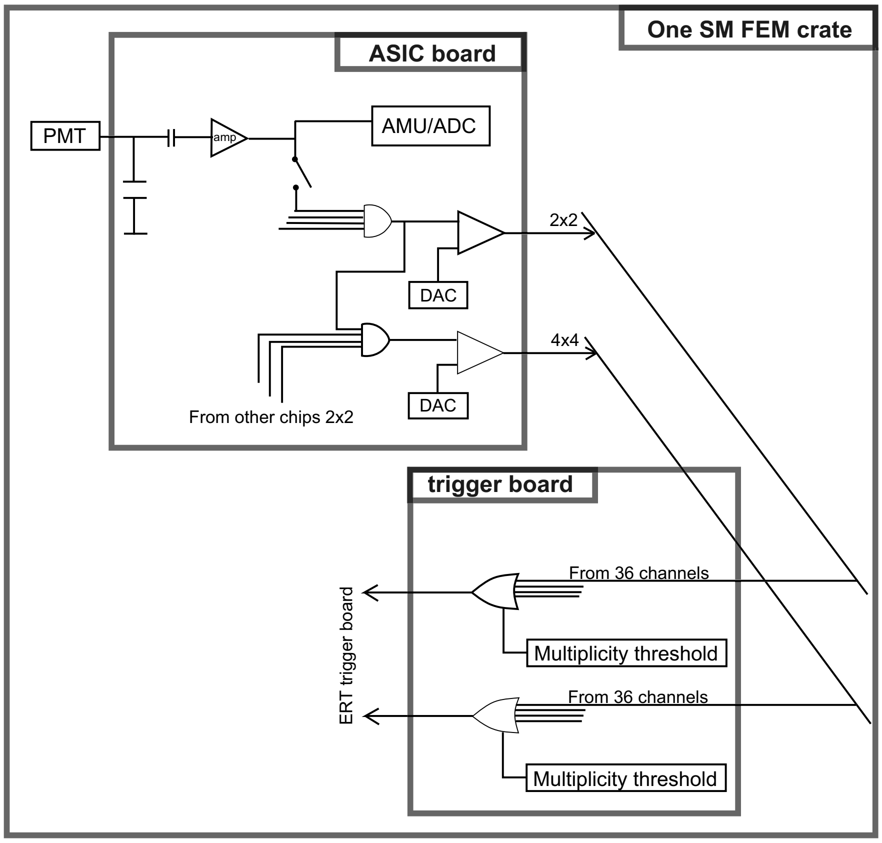

Figure 2.14: *Schematic view of the EMCal circuit for the ERT trigger. The analog sums from 2*x*2 towers and the 4*x*4 towers are discretized on the ASIC board. The 36 digital signals for 1 threshold level of 2*x*2 non-overlapping trigger and 3 threshold level of 4*x*4 overlapping trigger,* i.e. *144 digital signals in total, are sent into the trigger board. The number of the fired signal out of 36 is compared with a certain number for the LVL1 decision.*

Chapter 3

Analysis

3.1 Outline

In the following sections, we focus on the analysis of the PbSc. First, the run and trigger selection is explained in Section 3.2. The calibration of the PbSc during the run is critical for the purpose of correcting the yield and discussed in Section 3.3. The differential cross section ($E\cdot d^3\sigma/dp^3$) is calculated from the corrected yield of π^0 ($N^{\rm corr}_{\pi^0}$) and the luminosity ($\mathcal{L}$) as following:

$$E\cdot d^3\sigma/dp^3 = \frac{1}{2\pi}\cdot\frac{1}{\mathcal{L}}\cdot\frac{N^{\rm corr}_{\pi^0}}{p_T\cdot dp_T}\ .$$

The correction from the raw π^0 yield ($N^{\rm raw}_{\pi^0}$) to the corrected yield ($N^{\rm corr}_{\pi^0}$) in the high-p_T trigger is written as following:

$$\begin{array}{rcll} N^{\rm corr}_{\pi^0} = & & N^{raw}_{\pi^0} & \text{(Section 3.4)} \\ & \times & C^{\rm reco}_{\pi^0}(p_T) & \text{(Section 3.5)} \\ & \times & 1/\epsilon^{\rm high}_{\pi^0}(p_T) & \text{(Section 3.6)} \\ & \times & 1/\epsilon^{\rm mini}_{\pi^0}(p_T) & \text{(Section 3.7)} \\ & \times & \epsilon^{\rm conv\&albedo}_{\pi^0}\ . & \text{(Section 3.8)} \end{array}$$

In Section 3.4, the extraction procedure of the raw π^0 yield ($N^{\rm raw}_{\pi^0}$) is described. Most of the corrections from $N^{\rm raw}_{\pi^0}$ to $N^{\rm corr}_{\pi^0}$ are obtained using a Monte Carlo simulation with a parameterized EMCal response tuned to reproduce the test beam results as shown in Section 2.4.2. However, the performance during the run was deteriorated than that in the test beam due to the imperfection of the calibration. In Section 3.5, the detail of the Monte Carlo and reconstruction efficiency ($C^{\rm reco}(p_T)$) together with the performance of the PbSc during the run are described. In Section 3.6, trigger efficiency ($\epsilon^{\rm high}_{\pi^0}(p_T)$) of π^0 in the high-p_T trigger is discussed. Because the minimum bias trigger is defined by a hit of charged particles at forward and backward rapidity, the p_T distribution of π^0 in the minimum bias trigger can be biased. The correction for the bias, the trigger efficiency of π^0 ($\epsilon_{\pi^0}^{\mathrm{mini}}(p_T)$) in the minimum bias trigger is explained in Section 3.7. Due to the detectors between the collision point and the EMCal, the photons from π^0 decay may be lost before reaching to the EMCal. It is necessary to estimate and correct the π^0 production in the detectors, too. The correction ($\epsilon_{\pi^0}^{\mathrm{conv\&albedo}}$) of such the effects from other detectors are studied by the GEANT simulation as described in Section 3.8.

Finally, the calculation procedure of the luminosity ($\mathcal{L}$) and the merge procedure of the PbSc and the PbGl analyses are described in Section 3.9.

3.2 Run and Trigger Selection

The proton-proton data-set from run 2001–2002 consists of ∼17,000 PRDF files in total. This analysis includes only the runs that were collected after January 8th 2002, when the ERT triggers became stable. This portion of the data-set contains approximately 275 million events which corresponds to approximately 80% of the integrated luminosity for the entire run period.

Since the threshold for the ERT 2x2 tile trigger was raised from 0.3 GeV to 0.8 GeV in the middle of the data-taking period on January 15th 2002, the efficiency correction is time dependent. Due to higher trigger rates in lower threshold of 0.3 GeV, the trigger are sampled (pre-scaled) at every 10 and read out. Because the number of the high-p_T π^0 in lower threshold is less than in the higher threshold by a factor of 10 due to this sampling procedure, we decide to use only the data collected after this threshold had been raised. This choice works to avoid the complication of the threshold change and reduces the number of events to 230 million and the number of files to ∼8,000 PRDF files. This data-set includes the runs which were collected while the photon converter is installed. Because, as discussed in Section 3.4.3, no effect due to the presence of the converter is observed in the π^0 yield, these runs are neither removed from nor treated specially.

Out of the available runs, good runs are selected by placing quality cuts on the detector systems which are utilized in the measurement. The run-to-run performance of the BBC is checked by looking at the mean and sigma values for the measured collision z-vertex and collision time. There are no runs which appear anomalous, so no runs are removed from the analysis. Figure 3.1 shows the typical vertex distribution measured by the BBC in the minimum bias trigger. The typical width of the distribution is 40cm. We use the events with $< |30cm|$ in the analysis.

There are two classes of EMCal-only ERT triggers as described in Section 2.5.3: the 2x2 non-overlapping trigger and the 4x4 overlapping trigger. Because of a trouble on the electric circuit for the 4x4 overlapping trigger, the 2x2 non-

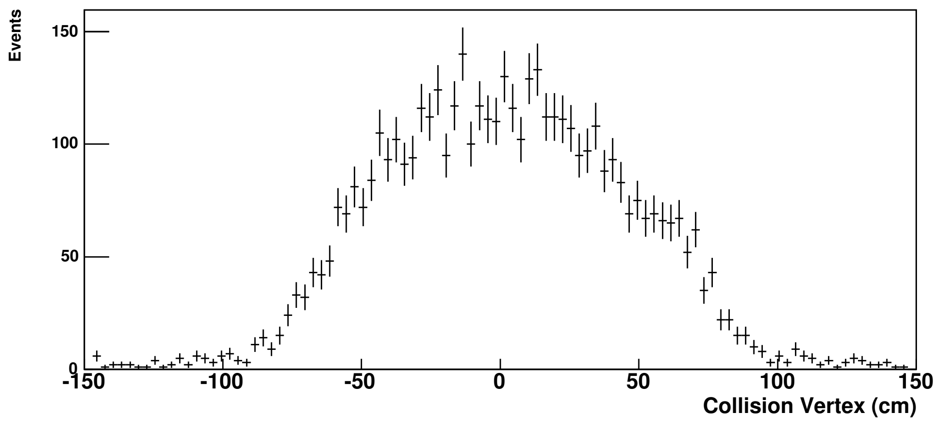

Figure 3.1: *Vertex distribution measured by the BBC from one run.*

overlapping trigger is used for extracting the π^0 spectra at high p_T. The 4x4 overlapping triggers, nevertheless, provide important information for understanding trigger biases. So, both sets of triggers are monitored as part of the trigger quality.

The quality assurance (QA) procedure for the ERT trigger is applied to each run by requiring that; 1) the LVL1 trigger bits are consistent with the ERT hits, 2) the rejection power of the ERT trigger, which is defined as the ratio of the number of the ERT trigger to that of the raw minimum bias trigger, is between 0 – 150. 3) the number of ERT hits per raw event, where the raw event contains the other trigger, is less than 10^{-3}. The 2nd requirement is the strongest one. Most of runs show that the rejection powers are around 80 for the analyzed runs. There are several runs with either zero or significantly higher than typical rejection power because the trigger, or perhaps some other critical subsystem, was clearly not operating properly. For some of the runs with anomalously high rejection power, it is suspected that the minimum bias trigger was misbehaving. For example, the minimum bias trigger is known to fire on noise hits if the TDC overflow value for a channel drifts below the threshold value in the logic. In another example, the minimum bias trigger is fired by empty bunches for one rings. Regardless of the origin, the runs with zero or higher rejection power than typical ones are discarded from the analysis

As a result of these run selection cuts, this analysis utilizes approximately 50% of the runs collected after January 15th. This sample consists of 4252 PRDF files from 102 runs with 130 million events, including 16 million events of the minimum bias trigger and 18 million events of the high-p_T (ERT 2x2 non-overlapping) trigger, which is equivalent to the beam luminosity of 39nb^{-1}.

3.3 EMCal Calibration

3.3.1 Quality Assurance of EMCal

For data quality, the main concern for the EMCal is changes in the number of dead or hot channels because such fluctuations not only alter the background in the π^0 sample but also can affect the acceptance correction in a manner which could be difficult to reproduce using simulation.

The dead towers are identified by looking at the energy distribution measured by each tower. Specifically, we examine 1) the number of clusters which deposit the maximum energy of >100 MeV on the tower, 2) the integrated energy on the tower, and 3) the mean energy on the tower.

A tower is considered hot if its value for any of these quantities deviated by 5σ from the mean value. In addition, a HV failure in a super-module happened during the run. As a result, it is necessary to use two sets of different dead map in the analysis. In both maps, the number of problematic channels in W3 sector is excessive (about 50%) when compared with the number in the other sectors because this sector is populated with ASIC boards which had been considered defective during the initial testing. Given that it performed poorly throughout the entire run, this PbSc sector is excluded from this analysis. As will be discussed in Section 3.5. the two different dead maps are taken into account in this analysis by splitting the data into two pieces and then applying an acceptance correction calculated with the appropriate dead map to each of these data-set. In the result, about 2% of towers are considered as dead. Another 2% of towers have a trouble during the energy calibration as discussed in the next section.

3.3.2 Energy Calibration

A good energy scale calibration for the calorimeter is essential for this measurement in addition to the position resolution and energy resolution. First of all, we try to calibrate the energy of the calorimeter using the laser calibration system as shown in Section 2.4. The purpose of the system is to measure the gain drift during the run. However, the system failed to do it because of the instability of the FEE for the photo diodes. The data during Au+Au collisions, which were taken for 4 months just before the p+p collisions, show different behavior of the gain drift from the laser calibration system. So we decide not to use the system, but to use the data itself to calibrate the energy.

Tower-by-Tower Energy Calibration From the test beam measurement done at the AGS, it is known that minimum ionizing particles at a normal incident angle produce a 260 MeV signal in the PbSc calorimeter. A set of minimum ionizing particles is isolated from the data-set by requiring a charged track in the drift chamber (DC) and the pad chamber (PC) for which the momentum is more than 0.4GeV/c. If two or more clusters are found for the same track, the track is matched to each of the cluster separately. This multiple use of tracks is dictated by the assumption that one of the clusters is the true one and the others are caused by random associations. As discussed below, the contribution of the latter is subtracted.

For each combination of a track and a cluster, the energy deposited in the PbSc is corrected for the incident angle of the particle on the PbSc using the following formula:

$$E_{\mathrm{corr}} = E_{\mathrm{clus}} \cdot \cos(\theta) \ , \tag{3.1}$$

where E_{clus} is the full cluster energy which is the energy sum from all towers in the cluster without any photon-sophisticated corrections, and θ is the incident angle of the track at the PbSc calculated from the track information.

Despite the low multiplicity in proton-proton collisions, random associations are still possible. Such events give rise to a background which falls steeply with energy and thus can shift the extracted position of the MIP peak. These associations are determined via the "flip & slide" method. In this procedure, the EMCal are flipped in z coordination when the hit position is greater than $|70.0\mathrm{cm}|$, and are slid in z coordination by ± 70.0cm towards the point of z=0 when the hit

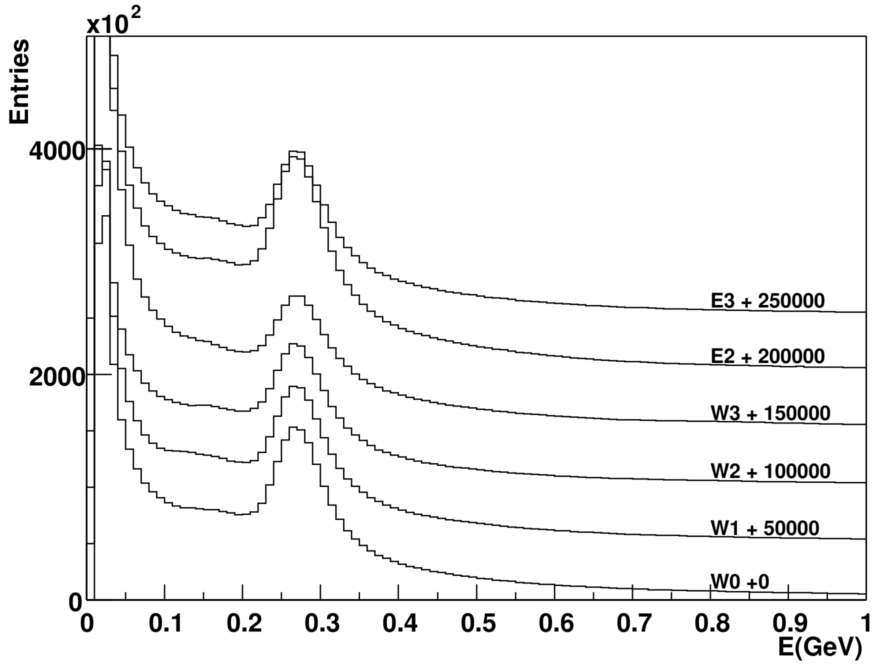

Figure 3.2: *Distribution of E_{corr} [$E_{\mathrm{clus}} \cdot \cos(\theta)$] in each of the six sectors. The peak is generated by minimum ionizing particles.*

position is less/more than |70.0cm|, where the z-coordination is defined as the same direction of the beam axis. The "flip & slide" spectrum is subtracted from the measured spectra to remove the random associations. Figure 3.2 shows the resulting spectra of E_{corr} for the six sectors. The number of MIPs seen in E2 sector is noticeably larger than the number seen in the other sectors. This difference might be caused by the TZR counter because the E2 sector is in the shadow of this counter. However, the π^0 peak and width in the E2 sector are normal.

The peak positions in all of the towers are obtained by fitting the peaks with a single gaussian function and then are used to derive corrections for the gain. These corrections are then applied to the data. This calibration is not perfect because the shape of the background from hadronic showers can affect the fitting. The uncertainty coming from the background shape is estimated in two ways: (A) differences inside a sector, and (B) differences between sectors. we assume that the (A) is due to only the incident angle. The systematic uncertainty due to (A) is estimated when estimating the energy resolution. The (B) is possible when the materials upstream of the sectors are different. The systematic uncertainty due to (B) is taken into account in the estimate of the absolute energy calibration as discussed in this section later.

In 2% of the towers, it is not possible to fit the MIP distributions with a gaussian as needed to obtain the position of the MIP peak. This fact is incorporated into a systematic error when calculating the acceptance correction as described in Section 3.5.2.

Energy Scale Calibration The position of the π^0 peak as a function of p_T is determined for each sector in the way described in Section 3.4. Due to the p_T smearing, the measured π^0 peak is expected to be about 139MeV unlike the nominal mass of 135MeV. However, the measured π^0 peaks in the sectors are different from the expectation by less than ± 1.5% although the gain of all the towers have been calibrated. They are used to calibrate the energy scale for every sector. We will discuss the uncertainty of the absolute energy calibration later in Section 3.5.4.

3.4 π^0 Reconstruction

In this section, we describe the method used to extract the raw π^0 yield ($N_{\pi^0}^{\mathrm{raw}}$) and then discuss the systematic error of this reconstruction procedure.

3.4.1 Procedure

For this analysis, an event is accepted if the z-vertex measured by BBC for the minimum bias trigger is within ±30 cm. For the high-p_T trigger sample, events are also required to fire the ERT 2x2 non-overlapping trigger. In the selected events, π^0 candidates are constructed for all pairs of clusters if:

- the energy asymmetry between the clusters, $|E_1 - E_2|/(E_1 + E_2)$, is less than 0.8, where the E_1 and E_2 is the measured energy in two clusters,
- the central tower, which is defined as a tower with the largest measured energy, has to be at least two towers away from the edge of sectors and outside from the 3x3 region of dead towers, and
- for the high-p_T sample, the cluster with the maximal energy has to be associated with a 2x2 non-overlapping trigger hit.

This cluster selection does not include cuts which require that the cluster had no associated track in the DC or PC. Since this choice increases the background only slightly, it is preferable in this analysis so as to avoid the additional complications of estimating the efficiency of the cuts.

For each of these two clutsters, the invariant mass, $M_{\gamma\gamma}$, is calculated using the following formula:

$$M_{\gamma\gamma}^2 = 4 \cdot (E_1) \cdot (E_2) \cdot \sin^2(\theta_{\gamma\gamma}/2) ,$$

where E_1 and E_2 are the measured energy of cluster 1 and 2 respectively, and $\theta_{\gamma\gamma}$ is the opening angle between the two photons calculated from the hit positions at the front face of the calorimeter and the vertex position obtained from the BBC.

3.4.2 Background Subtraction

Figure 3.3 shows examples of the invariant mass spectra as extracted from the minimum bias and high-p_T trigger sample for four p_T bins. The background is small especially in the higher p_T region. Nevertheless, a background subtraction is required. The background could be estimated by mixing clusters from different events. The spectra by mixing clusters does not have the same shape as the background. This disagreement is due to three effects: 1) correlations between particles which are present in the final state of proton-proton collisions, typically jet shape, 2) two clusters produced by a hadron interaction resulting in a sharp peak in the lower invariant mass, and 3) photon conversion to pairs. The third effect is the largest and is discussed in Section 3.8.

Instead of using the event mixing technique, the background is subtracted by fitting the invariant mass distribution. In this method, the π^0 peak is assumed to be gaussian and the background is fit with a variety of functions. In addition to varying the shape fitted to the background, different integration and fit ranges are used to estimate the systematic error in the subtraction. To be specific, we use two different integration ranges: [0.10,0.17] and [0.11,0.16] (in GeV/c^2) for

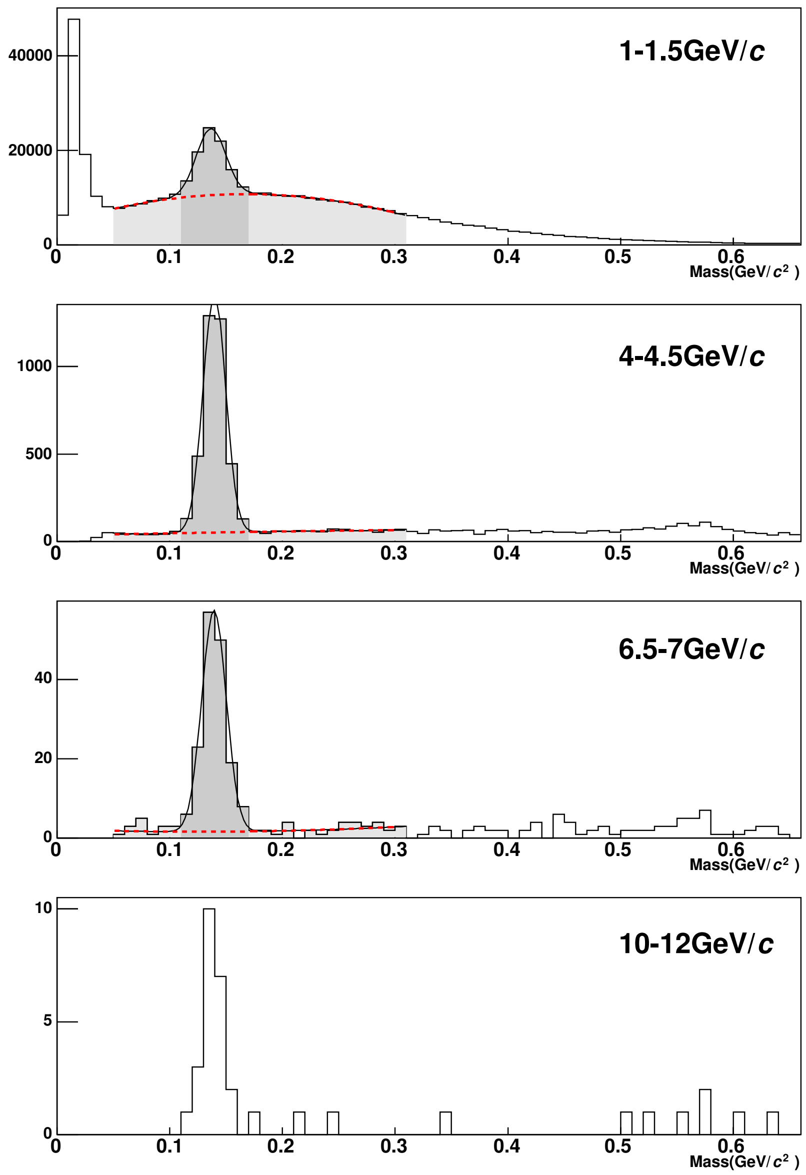

Figure 3.3: *Invariant mass distribution from the minimum bias trigger events with* p_T *=1–1.5 GeV/c and from the high* p_T *trigger events with* p_T *=4–4.5 GeV/c, 6.5–7 GeV/c, and 10–12 GeV/c shown together with the result of the fit for the background (red dotted line) and for the entire region (black straight line). The shaded areas represent the mass region for the fit (shallow shaded) and for the integration (dense shaded).*

the yield, three different fit ranges: [0.05, 0.30], [0.06,0.25], and [0.07, 0.20] (in GeV/c^2), and three different functions for the background: gaussian, second-order polynomial, and third-order polynomial. These combinations provide 18 ($2 \times 2 \times 3$) estimates for the yield. The π^0 yield is determined for each p_T bin from the mean of these 18 estimates and a systematic error is assigned to this value based upon the root-mean-square of the distribution of these estimates. The systematic error is 6% in the lowest p_T bin of 1.0–1.5GeV/c and decreases as p_T increases.

Due to limited statistics, the background can not be estimated in the same way for the bins with p_T of more than 7GeV/c. The signal to background ratio is obtained for each p_T bin for $p_T < 7$ GeV/c. By extrapolating the ratio, an estimate of the background contribution is inferred from the signal in each high p_T bin. To check this estimate, the background under the peak is estimated as the product of the yield per MeV in the region between the π^0 and η peaks and the integration range for the π^0 peak. These results are consistent with the estimate of 10% based on the extrapolation from lower p_T. The systematic error of 2% is derived by extrapolation of the systematic errors from lower p_T bins. Figure 3.4 shows the π^0 yield ($N_{\pi^0}^{\rm raw}$) as a function of p_T for the minimum bias and the high-p_T triggers.

3.4.3 Run Dependence

The dependence of the π^0 yield normalized to the number of analyzed events is checked as a function of run by partitioning the runs into ten sets. To estimate the expected run dependence, two types of run-to-run changes – (1) the change of dead map and (2) the change in the number of active ERT tiles – are considered as a simple assumption. This assumption is that the acceptance is independent of the p_T and scales as

$$(N_{\rm good\ towers})^2 \quad \times \quad (N_{\rm good\ trigger\ tiles}) \ ,$$

where $N_{\rm good\ towers}$ is the number of the good towers and $N_{\rm good\ trigger\ tiles}$ is the number of good trigger tiles. When the changes occur within one of the above set of runs, the number of events are calculated before and after the change and the weighted sum of the scale is used to calculate the effective acceptance for the set.

After applying this estimate for the acceptance correction, Figure 3.5 shows the run dependence of the π^0 yield per event normalized to 1.0 by the average over the entire run in the minimum bias and the high-p_T trigger. In both triggers, no decrease of the π^0 yield is observed during the run which are collected while the photon converter is installed so these runs are not treated specially in the analysis as noted in the Section 3.2. The run dependence in the minimum

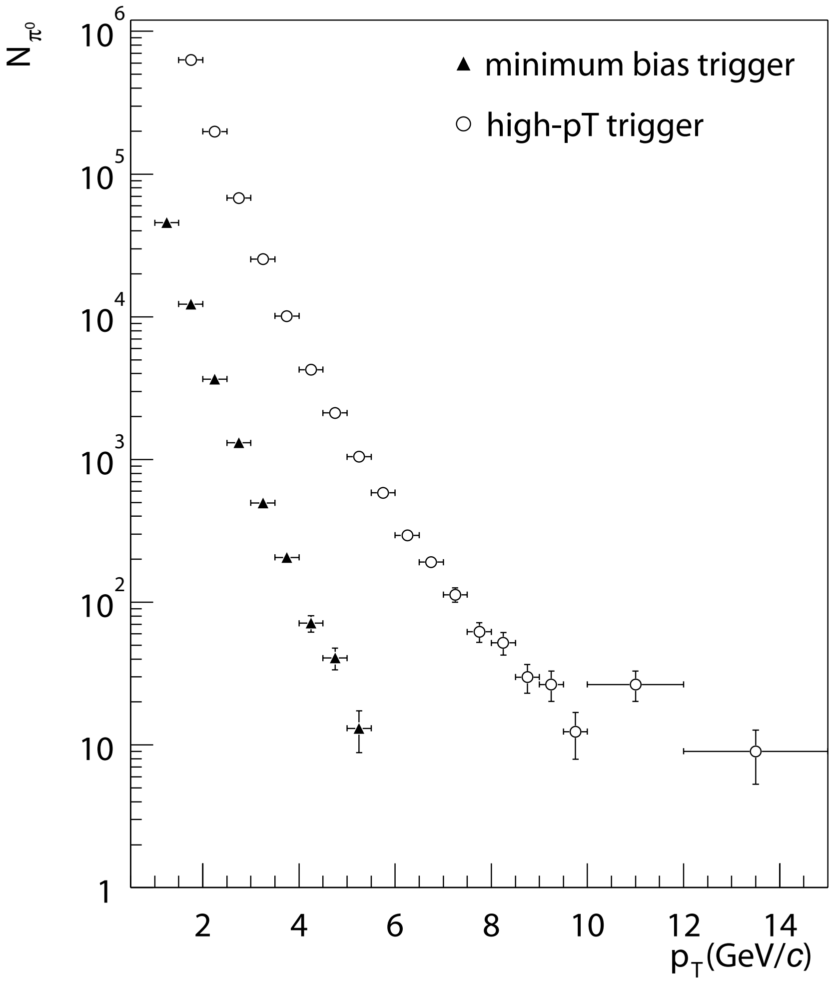

Figure 3.4: *Raw π^0 yield as a function of p_T for the minimum bias event sample (filled triangle) and the high-p_T trigger sample (open circle) with only the statistical error bar.*

bias trigger shows no dependences within the available statistical and systematic errors. However, that in the high-p_T trigger shows a continuous increase over the entire run range. The fitting by a 1st order polynomial function shows 3% increase from the start to the end of the run period. If this increase is caused by instability of the trigger threshold during runs, it will not affect our final result since we use the high-p_T trigger sample only for p_T higher enough than the threshold. However, we can't quite understand the cause of the increase. We, thus, assign a systematic error of 3%.

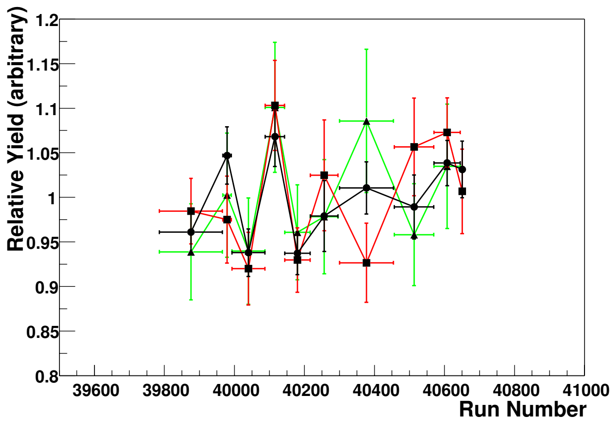

(A)

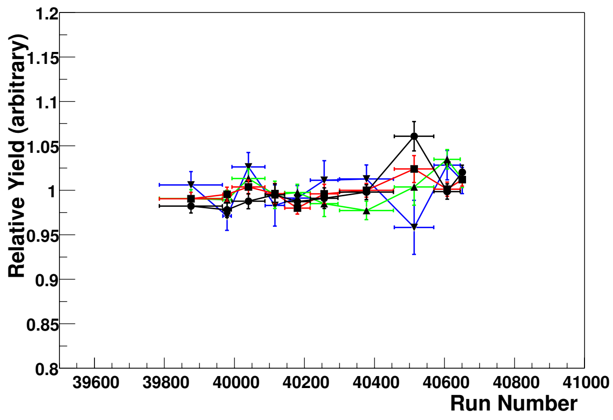

(B)

Figure 3.5: *Run dependence of π^0 yield in the minimum bias trigger sample (A) and the high-p_T trigger sample (B) per events by the average over the entire run range for three p_T ranges: (black line, circle) (1.0-1.5) GeV/c, (red line, square) (1.5-2.0) GeV/c, and (green line, up triangle) (2.0-2.5) GeV/c, and (blue line, down triangle) (2.5-3.0) GeV/c. The data for the p_T range of (2.5-3.0) GeV/c is only shown for the high-p_T trigger sample.*

3.5 Reconstruction Efficiency

Because of the intrinsic limitations of the detector, the observed π^0 spectra must be corrected for reconstruction efficiency, detector acceptance, and p_T smearing effects. These three corrections are obtained simultaneously using a Monte-Carlo simulation of the calorimeter, named as "FastMC". The FastMC is not like the GEANT simulation, but is a simulation in which the detector response is parameterized according to the performance during the run. As discussed in Section 3.1, we name the total correction as $C_{\pi^0}^{\mathrm{reco}}(p_T)$. This section describes the FastMC simulation used in this analysis and the estimates for the systematic error in the corrections. The systematic error on the corrections is derived from the uncertainty of the detector performance.

3.5.1 Contents of FastMC

The FastMC is written to simulate the initial condition of π^0 and the calorimeter performance. This FastMC includes the following initial condition:

- Vertex distribution – a gaussian distribution of 80 cm width based on one of the measured vertex distribution and with 30 cm cut. The effect of the changes of the vertex width during the run is estimated to be 0.5% and is negligible.
- p_T distribution – a formulae fitted to the obtained cross section spectrum.
- Pseudo-rapidity (η) and Azimuthal Angle (ϕ) Distribution – flat distribution within ± 0.5 of η and 0 to 360° of ϕ.
- π^0 decay – isotropic decay into two photons in the rest frame of the π^0.

The FastMC includes the following effects in the PbSc: acceptance, energy scale, energy non-linearity, energy resolution, and position resolution. For each effect, the parameterized functions are used in the FastMC to calculate $C_{\pi^0}^{\mathrm{reco}}(p_T)$. In the rest of this chapter, we explain which parameters are used in the FastMC and how we estimate the systematic uncertainty.

3.5.2 Acceptance

The dead channels in the calorimeter and clusters near the edge of the calorimeter need to be excluded from the data analysis. To simulate the acceptance properly, these channels also need to be cut in the simulation. The FastMC uses the same dead map and the same edge definition as is used in the data analysis. For each calorimeter hit, the sharing of the deposited energy among the towers is calculated using the shower profile extracted from the beam test.

The uncertainty of 4.5% is derived from two measurements.

- Dead towers – The 2% of towers with no MIP peak as discussed in Section 3.3.2 may not contribute to the π^0 yield at all.
- Edge towers – By the knowledge of the difference of the track projection and the cluster position on the EMCal by electron and positron, the uncertainty due to imperfection of the edge cut is taken into an account. The p_T dependence of this error is less than 1%.

The systematic error due to the uncertainty of the shower profile is negligible. For the systematic error for two photons decaying from π^0, the two errors are multiplied by two and added quadratically.

Energy Asymmetry One of good checks for the acceptance correction is the energy asymmetry between the clusters, $|E_1 - E_2|/(E_1 + E_2)$, where the E_1 and E_2 is the measured energy in two clusters. The energy asymmetry is equal to $\beta|cos\theta|$, where θ is the decay angle in the π^0 rest frame and β is the velocity of the π^0 in the laboratory frame. Since the π^0 has spin 0, the decay distribution should be flat in the energy asymmetry.

Figure 3.6 shows the raw number of π^0 yield as a function of the energy asymmetry compared with the FastMC in the p_T range of 1.0–1.5 and 2.0–2.5 in GeV/c. The FastMC contains all parameters as described later. The raw yield

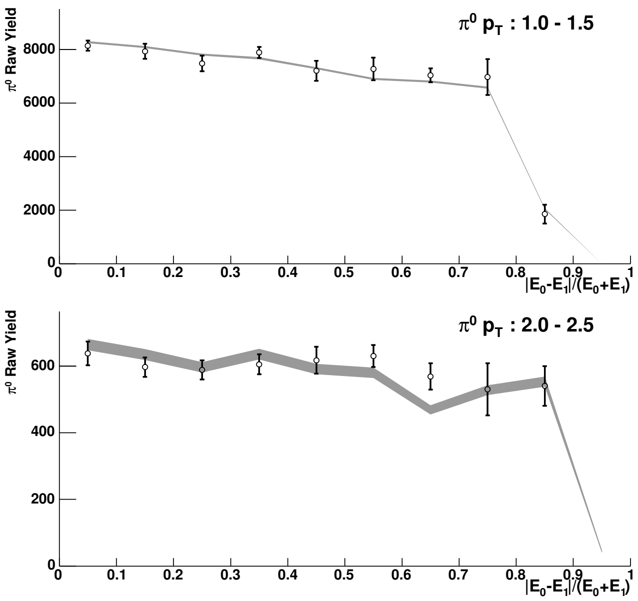

Figure 3.6: *Raw number of π^0 as a function of the energy asymmetry at p_T range of (1.0,1.5) and (2.0,2.5) (in GeV/c). The statistical and systematic errors are added quadratically. The shaded area shows the expectation from the FastMC.*

are constant at the energy asymmetry up to 0.8. In the p_T range of 1.0–1.5, the yield at the energy asymmetry of 0.8 is smaller than the other. The measured yield are consistent with the expectation from the FastMC. To reduce the larger background in the higher energy asymmetry, we analyze the π^0 sample with the energy asymmetry of less than 0.8 as discussed in Section 3.4.

3.5.3 Energy Resolution

Since the magnitude of the MIP energy deposit is sensitive to the clustering algorithm, a better test of the energy resolution is achieved by looking at the E/p ratio for electrons and positrons. A set of electrons and positrons is selected by adding a cut on the RICH to the charged track selection. As in the MIP analysis described before, the "flip & slide" method is used to determine the contribution of random associations to the electron and positron sample. Figure 3.7 shows the E/p ratio for the electron sample as a function of the momentum where the E is the corrected energy for photon. The peak position of E/p ratio plateaus at 0.98, not 1.0, because the depth of the shower from an electron is one radiation length ($\sim$2 cm) shallower than that from a photon and thus the light from the electron is slightly more attenuated in the fibers than the light from the photon. The inconsistency for $p<$ 0.8 GeV/c is a well known feature which is caused by a combination of the tower threshold effect and the electron energy loss prior to entering the calorimeter.

The p_T dependence of the ratio of the width to the mean in the E/p distribution is investigated. This quantity is equivalent to the energy resolution because the width arises mainly from the energy resolution. Figures 3.8 shows the p_T dependence of the ratio of the width to the mean in the E/p distribution for the PbSc. The error bar shows the deviation in different sectors. This ratio is fit to the sum of a constant and a $1/\sqrt{E}$ term in quadrature. The energy resolution is well described by the following magnitudes:

$$\frac{\sigma_E}{E} \sim (4.7 \pm 2.6)\% \oplus \frac{(9.5 \pm 0.9)\%}{\sqrt{E}} \ . \tag{3.2}$$

The obtained energy resolution is worse than the measured one in the test beam as discussed in Section 2.4.2. We explain possible causes of the worse resolution in Appendix B.

The uncertainty in this quantity affects the accuracy of the smearing correction and thus is a source for a systematic error on $C^{\rm reco}_{\pi^0}(p_T)$. In the FastMC, the effect of this uncertainty is estimated by varying the constant and the fluctuation terms of the energy resolution independently within their uncertainties. The errors in $C^{\rm reco}_{\pi^0}(p_T)$ vary from 0 to 3% with p_T due to the uncertainty in the constant term and by less than 1.5% due to the uncertainty in the fluctuation term.

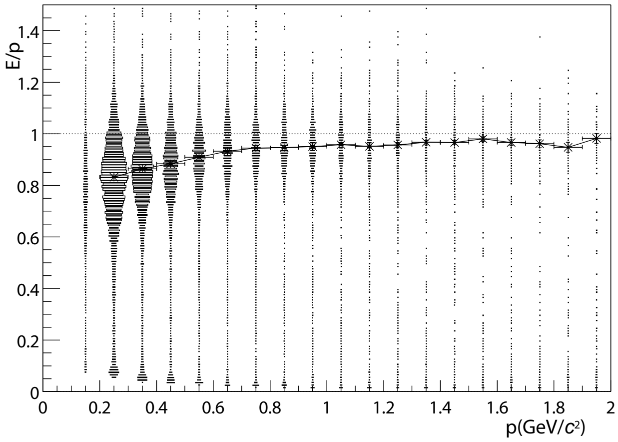

Figure 3.7: *A scatter plot of E/p versus p for electrons and positrons in the W0 sector. The star points indicate the central position of the distribution in each momentum bin and connected by line segments to aid the eye.*

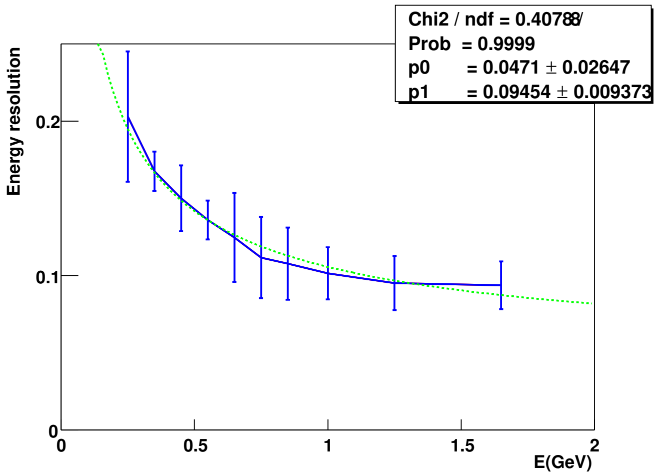

Figure 3.8: *Ratio of the width to the center value in the E/p distribution versus p_T from the sample of electrons and positrons in the PbSc. The error bar shows the deviation of the energy resolution in different sectors. The green dotted line is the result of a fit of these data to a "$a_0 \oplus a_1/\sqrt{E}$" function.*

3.5.4 Absolute Energy Calibration

The position of the π^0 peak as a function of p_T is compared against the FastMC. Figure 3.9 shows that the data are in good agreement with the predictions from the FastMC. As discussed in Section 3.8.1, the absolute energy calibration in the data is 0.7% lower than it should be. To remove this scale error from the result, the FastMC includes a correction for this non-optimal calibration. The measured position of the π^0 peak is shifted to be 139MeV unlike the nominal mass of 135MeV. because of the p_T smearing. When the measured p_T is higher/lower, the measured position of the peak likely looks higher/lower. The steep p_T distribution of the π^0 production cause the shift. However, in the lower p_T, the measured position is lower than 139MeV because of the tower threshold effect during the clustering algorithm. When the absolute energy scale is shifted by $\pm 1\%$ variation, all the data points are within the expectations from the varied energy scale. We conclude the uncertainty on the absolute energy scale is $\pm 1\%$.

This uncertainty influences the accuracy of the smearing correction and thus needs to be considered as a source for a systematic error. In the FastMC, the effect is treated by varying the energy scale correction from -1.0% to +1.0%. The $C_{\pi^0}^{\mathrm{reco}}(p_T)$ changes from 2 to 7% as p_T goes from 1 to 15 GeV/c.

3.5.5 Energy Non-linearity

As described in Section 2.4.3, a threshold cut is applied to select the towers to be included in the energy summation when clusters are constructed. This cut skews the measured energy of clusters, especially for those coming from hits with a small deposited energy. The FastMC included this effect by placing the same threshold cut of 10 MeV on the tower energy in the simulated data as is used in the real data.

From the test beam data, it is known that, as the light generated by a shower travels from its source to the PMT via fibers, the light is attenuated. Since the depth of the shower varies logarithmically with the energy, this attenuation causes non-linear energy response for particles. This effect is corrected in the real data analysis using the $e^{x_0 \ln(E)/\lambda} = E^{x_0/\lambda}$ form where λ is the attenuation length (120 cm) and x_0 is the radiation length of the calorimeter (~ 2 cm). In the FastMC, the additional contribution of the varied attenuation length is taken an account to estimate the systematic error. To estimate the maximal error from the uncertainty in this correction, the FastMC is run with three different values for the attenuation length of the fibers: (1) the nominal value of 120 cm, (2) a larger value of 66 cm, and (3) a smaller value of 600 cm. The upper and lower limits on the attenuation length are based on expectations for the variation in the attenuation length of the fibers. The position and the width of the π^0 peak in the data are compared against these three simulations as a function of p_T. The data indicate that the true value for the attenuation length is between 66 and

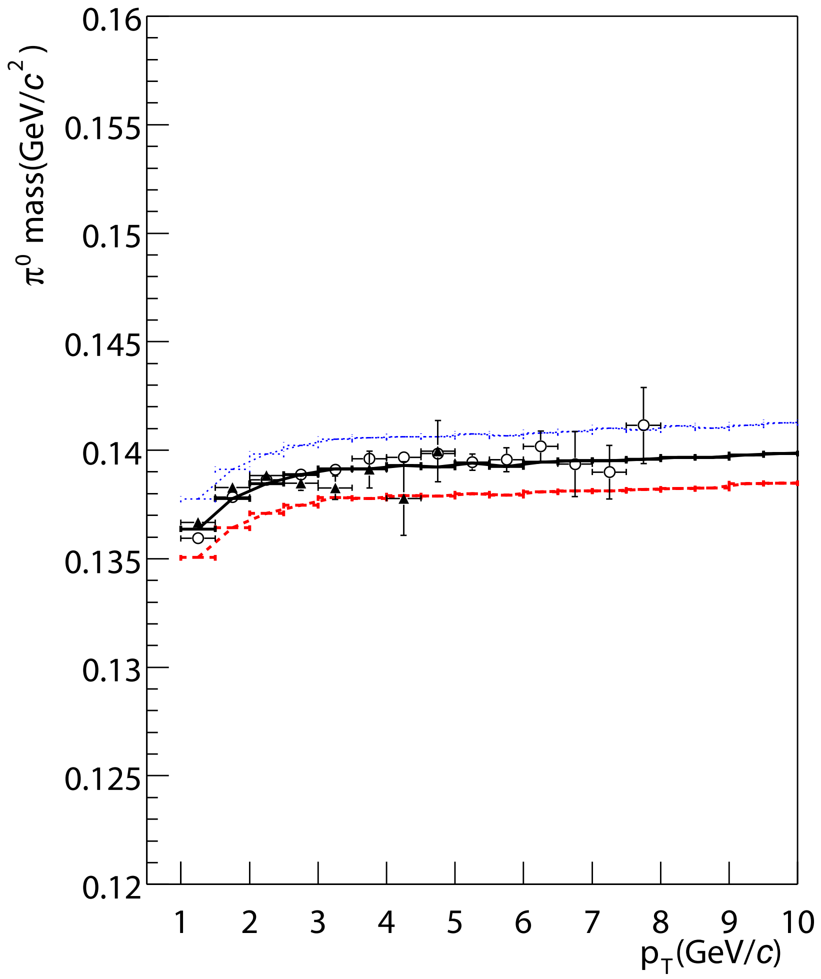

Figure 3.9: *Position of the π^0 peak as a function of p_T in the minimum bias trigger sample (closed triangle) and the high-p_T trigger sample (open circle) compared with the FastMC when the energy scale is corrected by -1.0% (red dashed line), 0.0% (black solid line), and +1.0% (blue dotted line)*

120 cm. From the best fit of the FastMC result with the data, the value for the attenuation length is chosen to be 81 cm instead of 120 cm. A systematic error is assigned to the value of $C^{\mathrm{reco}}(p_T)_{\pi^0}$ which is equal to the difference between results for attenuation lengths of 66 and 120 cm. In the result, we assign 2 to 8% depending on p_T as the systematic error.

3.5.6 Position Resolution

As discussed in Section 2.4.2, the position resolution is obtained from the test beam and is written as following:

$$\sigma_x = (1.4 + \frac{5.9}{\sqrt{E\ (\mathrm{GeV})}}) \oplus 20.0 \sin(\theta) \quad [\text{in mm}] , \tag{3.3}$$

where θ is the incident angle of the particle as obtained from the hit position of the cluster and the vertex position for the event.

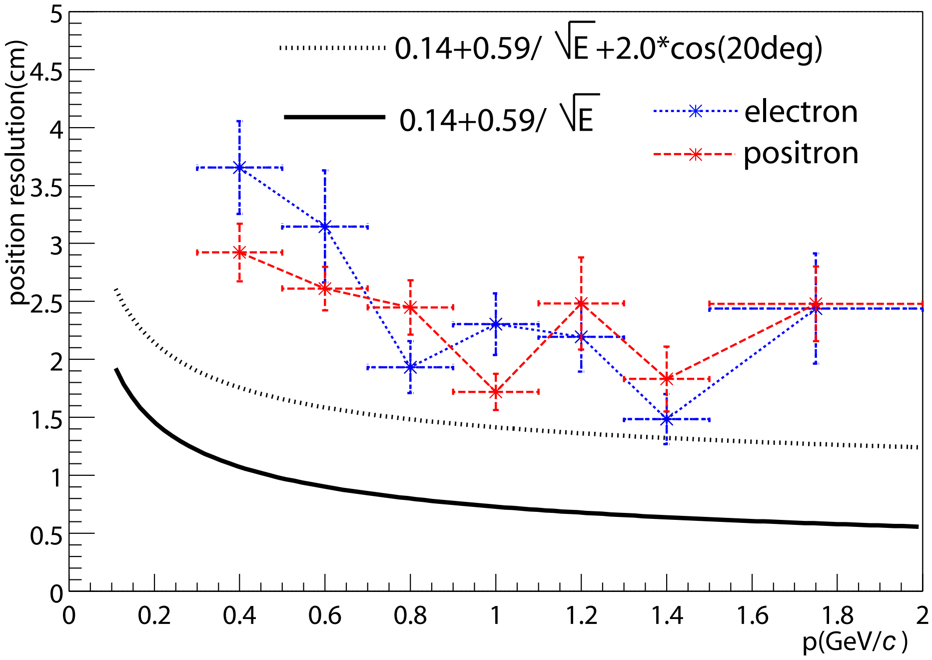

Figure 3.10: *Position resolution as a function of* p_T *as extracted for the electron (red dashed line) and positron (blue dotted line) samples compared with the nominal resolution (lower solid line) and with an additional terms of* $2.0\cos(20°)$ *mm (upper dotted line) as described in Section 2.4.2.*

By looking at the difference between the projection of the track to the calorimeter and the measured position of the cluster, we try to check the position resolution. For the sample of electrons and positrons, Figure 3.10 shows the width of the residual distribution as a function of p_T. This dependence is compared with the expectation for the nominal position resolution and the nominal position resolution with an additional term of $2.0\cos(20°)$ cm because 20° is the maximum angle for the PHENIX central arm acceptance. In both cases, the data lay above the curves. The resolution degradation could arise from errors in the tracking parameters. So we decide to discard the check and to use the π^0 width.

The width of the π^0 peak as a function of p_T is shown in Figure 3.11 and compared with the FastMC using the obtained energy resolution determined by E/p width as shown in Equation (3.2). The dashed line shown in the figure is an expectation using the nominal position resolution. In lower p_T, the width is consistent with the expectation. This fact proves that the obtained energy resolution from E/p width is correct. However, the π^0 width starts to deviate from the expectation with the nominal position resolution at p_T more than 3GeV/c. As shown from electron and positron samples, the position resolution might be worse than the nominal resolution. The worse position resolution could affect the π^0 width in the higher p_T because the opening angle of two photons becomes smaller as the p_T increases. The comparison is done also for the nominal resolution plus 0.5 cm and 1.0 cm, which are shown as the solid and dotted lines in the figure, respectively. In this plot, the agreement is best when there is an additional 0.5 cm term. We decide to use the nominal position resolution plus 0.5 cm and to assign ±0.5cm for the uncertainty of the position resolution. The variation in $C^{\mathrm{reco}}_{\pi^0}(p_T)$ for these three cases is less than 0.5%.

3.5.7 Summary of Systematic Errors

Each of the effects included in the FastMC introduces a systematic error to the final result for $C^{\mathrm{reco}}_{\pi^0}(p_T)$ and thus also the final cross section. Table 3.1 lists the summary of the systematic error assigned to $C^{\mathrm{reco}}_{\pi^0}(p_T)$ for each effect.

Source	p_T=1GeV/c	p_T=10GeV/c
Acceptance	4.5%	4.5%
Energy absolute calibration	2.1%	7.0%
Energy non-linearity	1.6%	8.3%
Energy resolution (fluctuation term)	1.5%	1.0%
Energy resolution (constant term)	0.0%	3.5%
Position resolution	0.5%	0.5%

Table 3.1: *Summary table of the systematic error estimates on* $C^{\mathrm{reco}}_{\pi^0}(p_T)$.

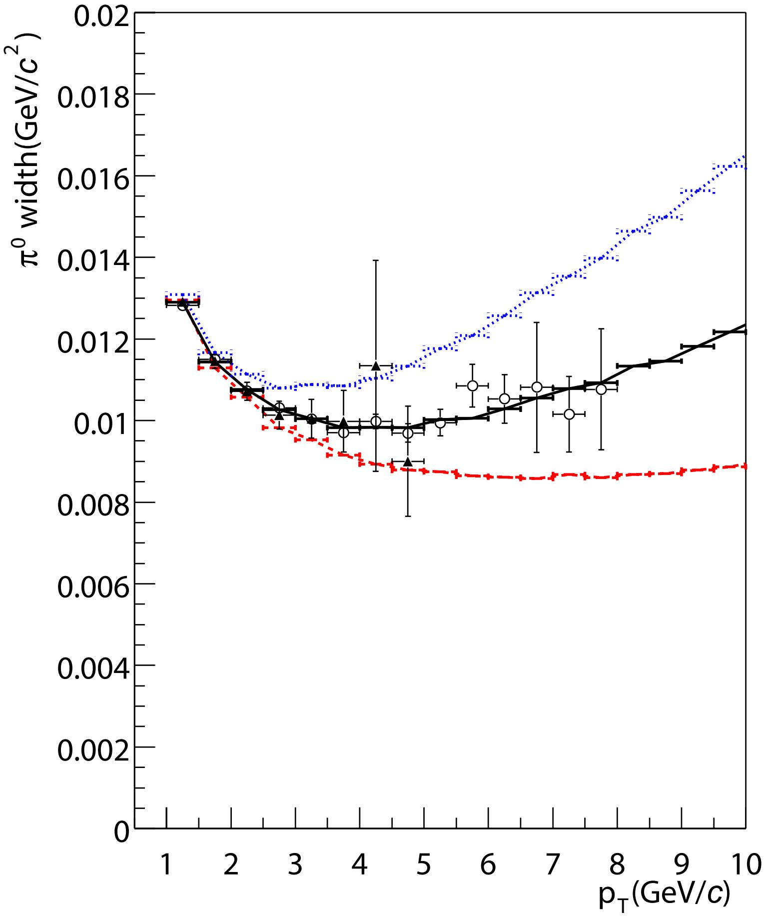

Figure 3.11: *Width of the π^0 peak as a function of p_T in the minimum bias trigger sample (closed triangle) and the high-p_T trigger sample (open circle) compared with results from the FastMC using a position resolution equal to the nominal one (red dashed line), plus 0.5 cm (black solid line), and 1.0 cm (blue dotted line).*

3.6 High-p_T Trigger Efficiency

Because the high-p_T trigger is not 100% efficient, its efficiency for triggering on π^0 particles, $\epsilon_{\pi^0}^{\mathrm{high}}(p_T)$, has to be extracted from the data and then applied as a correction to the observed high-p_T π^0 spectrum. From the samples in the minimum bias trigger, the efficiency of the high-p_T trigger is measured on a tile-by-tile basis, where the tile is defined as 2x2 sum in the 2x2 non-overlapping trigger. The energy deposited in each 2x2 sum is calculated by summing up the energy in the four towers which comprise the tile. The energy of any dead tower is ignored. We cannot assign an ERT hit directly to one tile since the granularity of the ERT hit is at the super-module level, in other word, one ERT hit represents the OR of threshold decisions for thirty-six 2x2 sums. We assume the ERT hit is assigned to the tile with the largest deposited energy in the super-module. The fraction of events with an ERT hit in the super-module represents the trigger efficiency and is calculated as a function of the tile energy. Figure 3.12 shows a plot of this fraction versus the tile energy in the W0 sector. The trigger saturated at ~1.5 GeV to a level of ≈95% which is consistent with the number of active super-modules in the high-p_T trigger. The fall-off at high-p_T above 2 GeV is a result of a few remaining noisy channels which are not been masked. The turn-on regions of these curves are fit with a cumulative Gaussian. Based upon this fit, the trigger is 50% efficient at 0.8 GeV and the width of the turn-on region is 0.17 GeV.

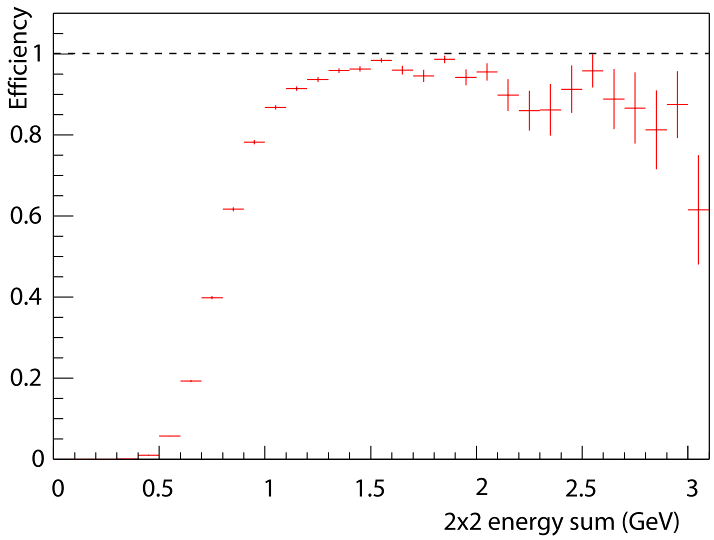

Figure 3.12: *Efficiency of the high-p_T trigger as a function of the energy deposited in a 2x2 sum with a fit of a cumulative Gaussian to the turn-on region.*

There is an inconsistency from the fit at the 2x2 sum energy between 1 to

1.5GeV. This is caused by the imbalance of the amplifier on the electric circuit. As discussed in Section 2.5.2, the adjustable feature of the amplifier gain is not used. For more thorough calculation, the measured energy in each tower is translated into ADC by applying the reversed calibration and is summed up to get the turn-on curve as a function of ADC. This turn-on curve in ADC is then incorporated into the FastMC simulation. As with the data, the input to the high-p_T trigger for each tile is calculated by summing up the ADCs in the four towers comprising the tile. Using these sums, the probability for each tile to fire is looked up from the threshold turn-on curve. The trigger for the π^0 then requires that one tile from higher energy photon fires the trigger. This condition results in that a trigger decision is sensitive to only the photon with the larger energy thus simplifies the dependence of the trigger efficiency on p_T. In the data, the number of π^0's are determined as described in Section 3.4 and the trigger condition requires that the cluster with the maximal energy is associated with an ERT hit. Figure 3.13

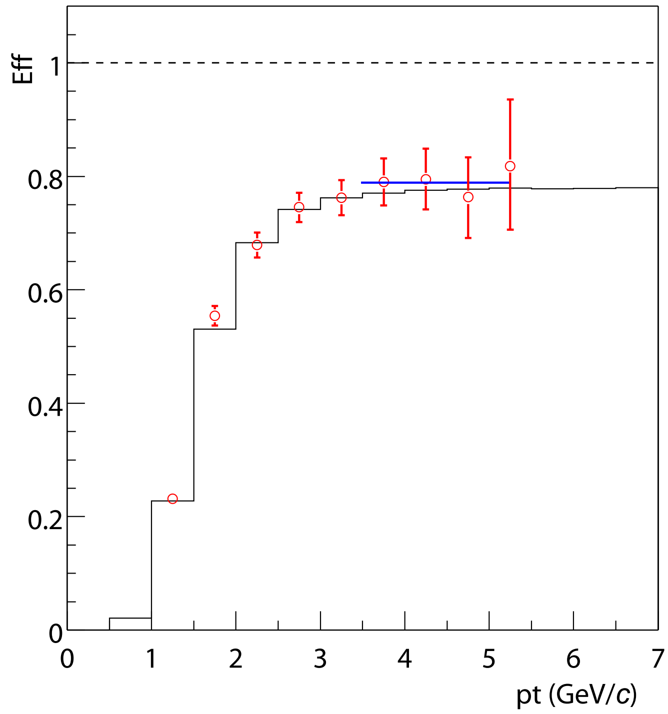

Figure 3.13: *Trigger efficiency for π^0's in the high-p_T trigger as a function of p_T of π^0. The red points are obtained from the analysis of the minimum bias trigger samples. The black histogram shows the predicted value obtained from the FastMC. The blue solid line shows the plateau value for the trigger as determined from the fraction of active tiles.*

shows the results of this comparison as a function of the π^0 p_T. The FastMC shows consistency behavior at p_T up to 5.5GeV/c.

The high-p_T trigger sample is corrected for the trigger efficiency using these data. For $p_T < 3.5$ GeV/c, this correction is taken from the threshold curve that is extracted from data because, in these bins, there is sufficient statistics to measure it. For higher p_T, there are not enough statistics, so the correction is determined from the fraction (0.778) of the number of active 2x2 sums. The difference between this value for the correction and the plateau value for the trigger efficiency as calculated with the FastMC is assigned as the systematic error for the correction. This error is 3% (0.023), which is dominated by the statistical error at $p_T > 3.5$ GeV/c. It should be noted that, because the high-p_T trigger is in coincidence with the minimum bias trigger, the resulting π^0 spectra is still biased by the event configuration requirement inherent in the minimum bias trigger. We discuss the trigger bias in next section.

3.7 Trigger Bias of Minimum Bias Trigger

The minimum bias trigger only fires when there are charged particles at forward and backward rapidity. This requirement does not only affect the normalization of the measurement but also could distort the p_T distribution of π^0 because it could bias the physics processes which generate the observed π^0. From the data, it is possible to determine the correction for this effect because one of the ERT 4x4 overlapping trigger has a raised threshold to reduce its raw trigger rate instead of being put in coincidence with the minimum bias trigger as is done with the 2x2 non-overlapping trigger. This trigger therefore measures the unbiased π^0 samples. From this sample of events, the trigger efficiency of π^0 ($\epsilon_{\pi^0}^{\mathrm{mini}}(p_T)$) is equal to the fraction of π^0 for which the minimum bias trigger also fired. To calculate this fraction, the π^0 sample is extracted from the 4x4 overlapping trigger sample using the procedure described in Section 3.4, except that no vertex cut is applied when selecting events. and that the invariant mass is calculated by assuming both photon are from zero vertex point. The exceptions doesn't change the distribution of the invariant mass and the yield of the π^0. If the fraction is equal to the trigger efficiency of events (0.516) as discussed in Section 3.9.1, the minimum bias trigger doesn't distort the π^0 production. Figure 3.14 shows the dependence of the trigger efficiency of π^0 on p_T. The efficiency is higher than 0.516 and is independent of p_T. Over the measured p_T range, this result agrees reasonably well both in shape and in magnitude with the PYTHIA [112] simulation for which it is 0.75, 0.76, 0.73, and 0.72 for a p_T of 1, 2, 4, 8 GeV/c. The efficiency for the PbGl agree very well with the PbSc and the averaged value of the efficiencies is 0.748 ± 0.022.

In this discussion, it has been assumed that the 4x4 overlapping trigger only fired as a consequence of a particle from real collisions. This assumption could be

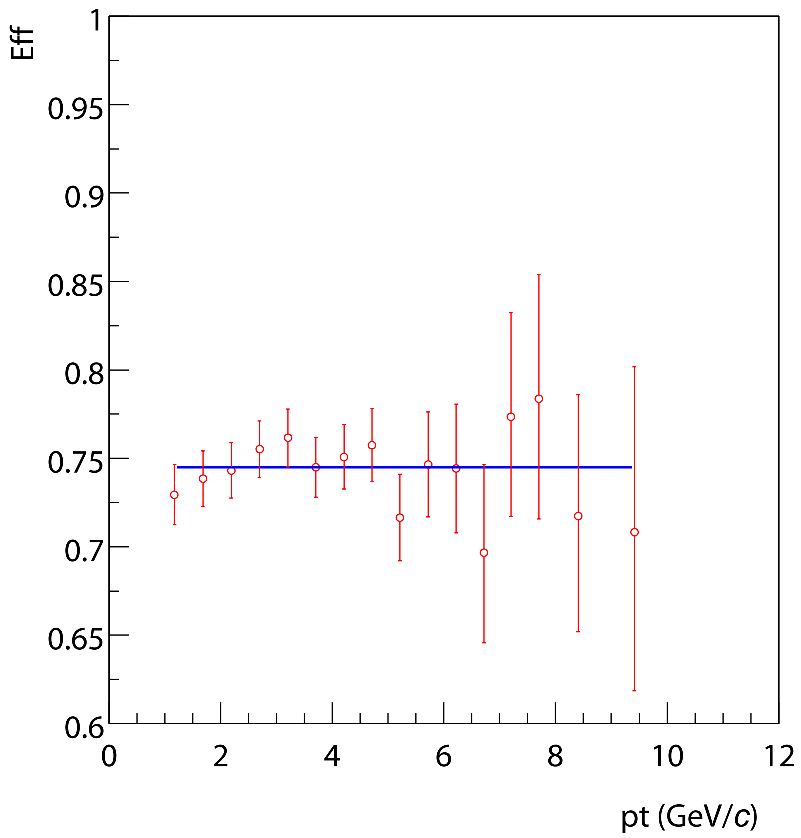

Figure 3.14: *Trigger efficiency of π^0 ($\epsilon_{\pi^0}^{\mathrm{mini}}(p_T)$) as a function of p_T of π^0 with a fit by a solid line.*

incorrect since the trigger could have been caused by electronics noise, particles from beam-gas or halo interactions, or cosmic rays. Events resulting from such triggers would alter the bias estimate because they would not be as likely to be accompanied by the minimum bias trigger. The non-collision contribution is studied by selecting bunch crossings in which the bunch from one of the beam is empty. As shown in Figure 3.15, the invariant mass spectra for two photons in these bunches is nearly nonexistent above 100 MeV. This study confirms that the estimate of the trigger efficiency of π^0 made with the 4x4 overlapping trigger sample is appropriate.

3.8 Conversion Effect

In the PHENIX central region, there is a non-negligible amount of material including a beam pipe and many detectors situated between the vertex point of

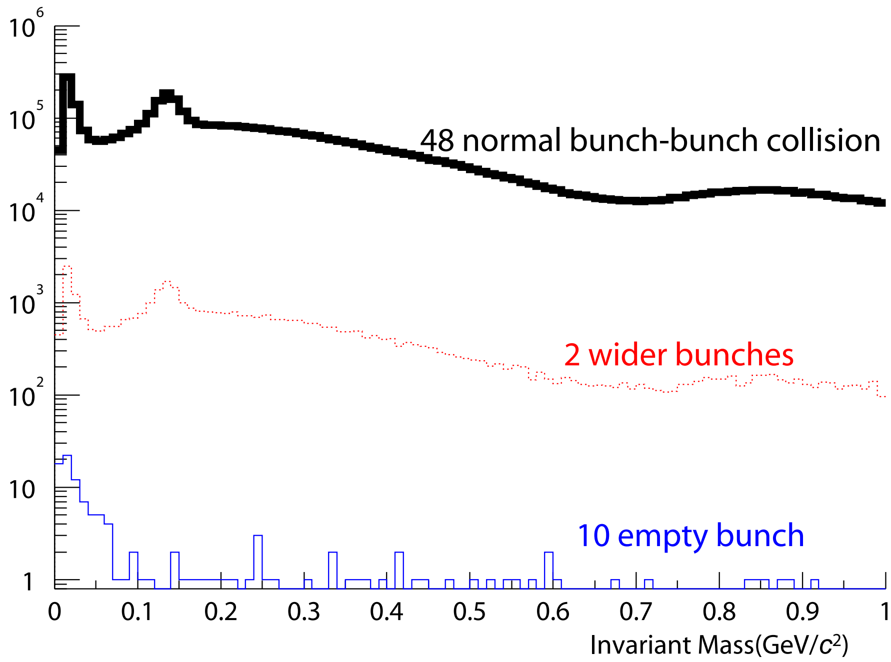

Figure 3.15: *Invariant mass distribution for paired clusters in the bunch crossing between collisions of normal bunches (top, black thick line), those of normal and wider emittance bunches (middle, red dotted line), and those of normal and empty bunches (bottom, blue solid line).*

a collision and the EMCal. Sometimes, one of the photons from the decay of a primary π^0 may convert to an e^+e^- pair in these materials. Depending on where this conversion occurs, the initial π^0 may or may not be reconstructed. For instance, if a photon converts just in front of the calorimeter, the resulting pair would not be resolved as separate clusters and, thus, would appear as a cluster from a single photon with nearly the same energy as the initial photon. In this case, the initial π^0 is very likely to be detected. The same, however, is not true for a photon which converts in the beam pipe. This conversion loss needs to be estimated in order to correct the observed yield.

In addition, there are several sources for non-primary π^0 mesons: 1) decay of primary hadrons (*e.g.*, K_s^0 or η mesons) into π^0+X, and 2) generation of background π^0 mesons from interactions of primary particles with material in the detector. The first effect is small and is estimated to be less than 6% in total as discussed in Appendix C. We do not correct the first effect from the hadron decay in this analysis. Nevertheless, the second effect named as "albedo" has to be taken an account.

In this section, we discuss the method used in this analysis to estimate the effects.

3.8.1 1st Method

Description of 1st Method In this analysis, the GEANT [109] simulation with an initial particle distribution obtained from the PYTHIA [112] simulation is used to estimate the albedo contribution to the cross section. Along the lines of a typical analysis, correction factors for the observed yield would be derived from the simulation by

$$\frac{\#\text{ of }\pi^0\text{ reconstructed from the invariant mass distribution}}{\#\text{ of }\pi^0\text{ generated}}\ .$$

This factor, however, includes corrections for all effects which influence the detection of π^0's. In our analysis, most of these effects are accounted for by the $C^{\mathrm{reco}}_{\pi^0}(p_T)$ correction determined with the FastMC as described in Section 3.5 because the FastMC is tuned to the data better than the GEANT simulation. To avoid double correction for such effects, a method is employed to isolate the conversion and albedo contributions to the detection efficiency. The initial particle distribution obtained from the PYTHIA. we calculate

$$\epsilon_{\mathrm{albedo}} = \frac{\#\text{ of }\pi^0\text{ in the peak of }\textit{selected}\text{ mass distribution}}{\#\text{ of }\pi^0\text{ in the peak of }\quad\textit{all}\quad\text{ mass distribution}}\ , \tag{3.4}$$

where the *selected* mass distribution is obtained from combinations of clusters which are only associated of photons from π^0 decays, the *all* mass distribution is obtained from all combinations of all clusters. The former represents that two photons from π^0 generated at the collision vertex reach on the EMCal without any conversion. Both the numerator and the denominator are calculated from the invariant mass plots of the observed clusters. As a consequence, the effects of the acceptance, reconstruction, and smearing appear in both numerator and denominator and thus cancel. The denominator contains both the conversion and albedo effect.

However, in the analysis of real data, no cut is imposed to remove clusters which came from electrons or positrons. Since electrons or positrons from conversions near the calorimeter face would generally result in a single cluster with nearly the same energy as the initial photon, the conditions imposed in the determination of the numerator of Equation (3.4), *i.e.* that only clusters coming from photons associated with the decay of a primary π^0, is too stringent. Thus, the factor ($\epsilon_{\mathrm{albedo}}$), as written, would over-correct the yield if applied. In principle, the criteria for selecting clusters when computing the numerator could be loosened to include cases where a photon from a primary π^0 converted to an e^+e^- pair but, due to the proximity of the two particles in the calorimeter, gave rise to a single cluster in the calorimeter. We estimate a correction ($\epsilon_{\mathrm{conversion}}$) to the numerator for the conversions as

$$\epsilon_{\text{conversion}} = \frac{\#\text{ of } \quad pure \quad \pi^0}{\#\text{ of } generated \ \pi^0} \ , \tag{3.5}$$

using the GEANT simulation of single π^0 events, where the *pure* π^0 is obtained from the *generated* π^0 when the both photons reach the EMCal without the conversion loss. The total correction for the π^0 yield is

$$\epsilon_{\pi^0}^{\text{conv\&albedo}} = \frac{\epsilon_{\text{albedo}}}{\epsilon_{\text{conversion}}} \ . \tag{3.6}$$

We discuss the details of computing these two factors.

Conversion Correction Factor The conversion correction factor ($\epsilon_{\text{conversion}}^{\pi^0}$) is determined from the GEANT simulation. In this simulation, single π^0 events are generated with flat ϕ and η distributions in different p_T starting at 0.5 and going up to 7 GeV. For each p_T, the sample of *generated* π^0 mesons are determined. Of this sample, the sub-sample of *pure* π^0 mesons is determined by requiring the hit on the EMCal without any conversion interaction for the *generated* π^0. The ratio of the counts in the sub-sample to that in the sample is equal to the conversion correction ($\epsilon_{\text{conversion}}^{\pi^0}$). In order to have a cross check, the analogous procedure is applied to extract a sample of photons, then to extract a sub-sample of detected photons, and finally to calculate the conversion factor for single photons ($\epsilon_{\text{conversion}}^{\gamma}$).

Figure 3.16 shows the values of $\epsilon_{\text{conversion}}$ for each of the six PbSc sectors as a function of p_T for the photon and the π^0 samples in the left and right panels, respectively. At first glance, the correction for π^0's ($\sim$20%) is roughly twice that for photons ($\sim$ 10%), which is quite reasonable. To extract the correction, the plots in Figure 3.16 are fit to a straight line. The results of this fit are averaged in each of the calorimeter unit and are 82.5±0.4 for the West Arm and 81.7±0.6 for the East Top, where the quoted error bar is statistical only. we refer to the existing XCOM database [113] and assign a 2% systematic error on this correction to account for the p_T dependence.

Albedo Correction Factor The albedo correction (ϵ_{albedo}) defined in Equation (3.4) is extracted from data generated by the GEANT with the initial particle distribution obtained from the PYTHIA. In this simulation, PYTHIA v5.720/JETSET v.7.408 is used to generate the event sample. We use the default setting of the PDF (CTEQ5L) and the FF (LUND model).

For each p_T, the invariant mass spectra are obtained from combinations of clusters using the reconstructed energy and position information. When extracting the π^0 yield, we apply the same software as is used for real data analysis. The denominator in Equation (3.4) is then calculated from the invariant mass distributions generated from *all* combinations of clusters. For the numerator of

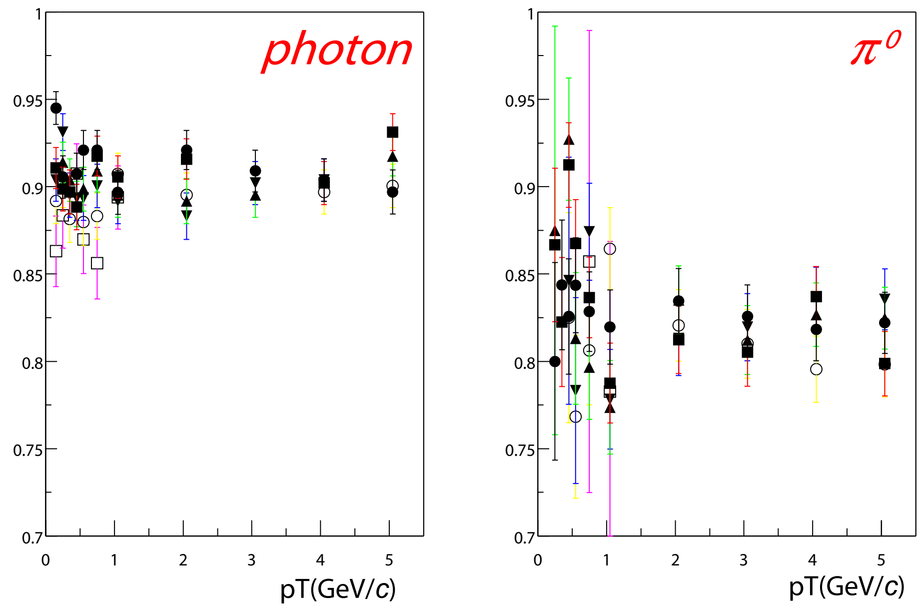

Figure 3.16: *(left)* $\epsilon^{\gamma}_{\text{conversion}}$ *and (right)* $\epsilon^{\pi^0}_{\text{conversion}}$ *as obtained in the GEANT simulation with a single* π^0 *events in W0 (black line, closed circle), W1 (red line, closed square), W2 (green line, up triangle), W3 (blue line, down triangle), E2 (yellow line, open circle), E3 (magenta line, open square) sector.*

selected π^0, additional requirements are imposed to restrict the sample of clusters considered for the invariant mass plot to those associated with a photon which originated from the decay of π^0 mesons generated in the collision. Specifically, we require the particle which deposited the most energy in a cluster is a photon, the parent of this photon is a π^0 from the collision vertex.

The observed peak position of the π^0 increases by 1 MeV as a result of the selection requirement. It means that the measured mass of π^0 mesons is lower than that in the FastMC. Figure 3.17 shows the direct comparison between the two samples of the invariant mass spectra after the contribution of the combinatorial background has been subtracted. The peak position in the *all* sample is lower than that in the *selected* sample. Since the absolute energy of the EMCal is calibrated by comparing the measured π^0 mass with the predictions from the FastMC and the FastMC includes neither albedo nor conversion component, the absolute energy calibration should be shifted by 1 MeV. As mentioned in Section 3.5, this effect is taken into account in the calculation of $C^{\text{reco}}_{\pi^0}(p_T)$ correction.

The ratio as a function of p_T is constant for the investigated range of p_T within the statistical error of the simulation. In this analysis, we fit the ratio by a constant. The results ($\epsilon^{\pi^0}_{\text{albedo}}$) of the fitting are $87.6\pm0.7\%$ in the West Arm

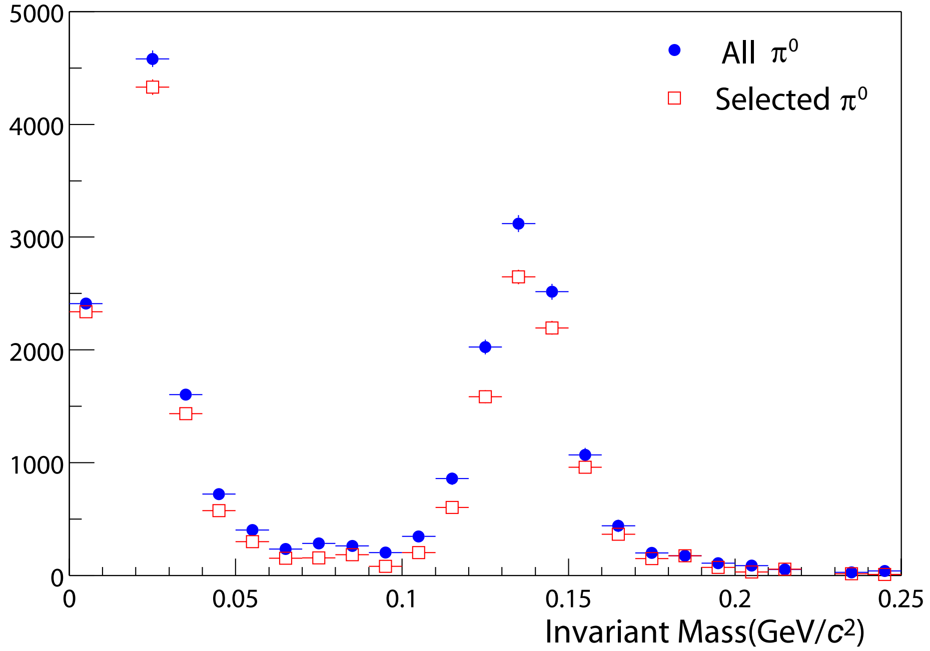

Figure 3.17: *Invariant mass spectrum in p_T of 1.0 to 1.2 GeV/c. The filled circle shows the sample of all cluster pairs and the open square shows the sample of selected pairs. The peak at around 0.03GeV/c^2 is caused by the charged and neutral hadron.*

and 86.8±0.9% in the East Top.

Total Correction in 1st Method The overall correction is calculated by Equation (3.6) as shown in Table 3.2.

West Arm	1.062±0.008
East Top	1.063±0.011

Table 3.2: *Overall correction ($\epsilon_{\pi^0}^{\mathrm{conv\&albedo}}$) as obtained from the conversion and albedo correction factors by Equation (3.6). The quoted error is statistical only.*

3.8.2 2nd Method

As defined by Equation (3.4), the albedo includes a contribution from so-called recovered conversion losses. In such events, one of the photons converts to an

e^+e^- pair, but, due to the proximity of the two particles in the calorimeter, still gives rise to a single cluster in the calorimeter. Since the energy of this cluster is quite close to the energy of the original photon, it is likely that the original π^0 is still reconstructed in the observed π^0 peak of the invariant mass distribution. To study this component of the albedo correction ($\epsilon_{\rm albedo}$), we determine the fraction of reconstructed π^0 mesons which are detected even though one of the photons converted to a pair. From the all samples, the sub-sample of these recovered π^0 candidates is selected by; 1) the particle is either an e^+ or an e^-, 2) the parent of this particle is photon, and 3) the grandparent of this particle (*i.e.*, the parent of the photon) is a π^0. We obtain the ratio of the yield of the selected π^0's to that of all π^0's and fit the p_T dependence by a constant. The results by the fit are $13.6 \pm 0.4\%$ for the West Arm and $14.4 \pm 0.6\%$ for the East Top. After adding the results of the above and $\epsilon^{\pi^0}_{\rm conversion}$, the total sum become 101.2% for the West Arm and 102.2% for the East Top and are consistent with 100% within the statistical error. we conclude that nearly all measured π^0 can be attributed to either $\gamma{+}\gamma$ or $\gamma{+}e^+/e^-$.

If this is indeed the only component of the albedo, then the total correction factor could be estimated more directly from a single particle Monte Carlo. Within in this context, we use a single particle GEANT simulation to estimate the fraction of π^0 which are produced but not counted in our analysis due to conversion effects. In this effort, single π^0 are generated according to a flat $\phi - \eta$ distribution. The particles are then propagated through the GEANT simulation.

For generated π^0's with p_T of 1.05 GeV/c, Figure 3.18 shows an example of the measured p_T and invariant mass spectra. The correction ($\epsilon^{\rm conv\&albedo}_{\pi^0}$) is then equal to

$$\epsilon^{\rm conv\&albedo}_{\pi^0} = \frac{\#\text{ of reconstructed }\pi^0\text{ in the mass window}}{\#\text{ of generated }\pi^0\text{ in simulation}} \ .$$

This quantity is plotted as a function of p_T for the eight calorimeter sectors with the mass window between 0.10GeV and 0.18GeV. This ratios are almost independent of p_T. We estimate $\epsilon^{\rm conv\&albedo}_{\pi^0}$ from fitting with a constant as shown in Table 3.3.

West Arm	1.019±0.002
East Top	1.021±0.006

Table 3.3: *Correction ($\epsilon^{\rm conv\&albedo}_{\pi^0}$) to the yield in the 2nd method as calculated using the simple procedure which is valid if the albedo is negligible. The errors are statistical only.*

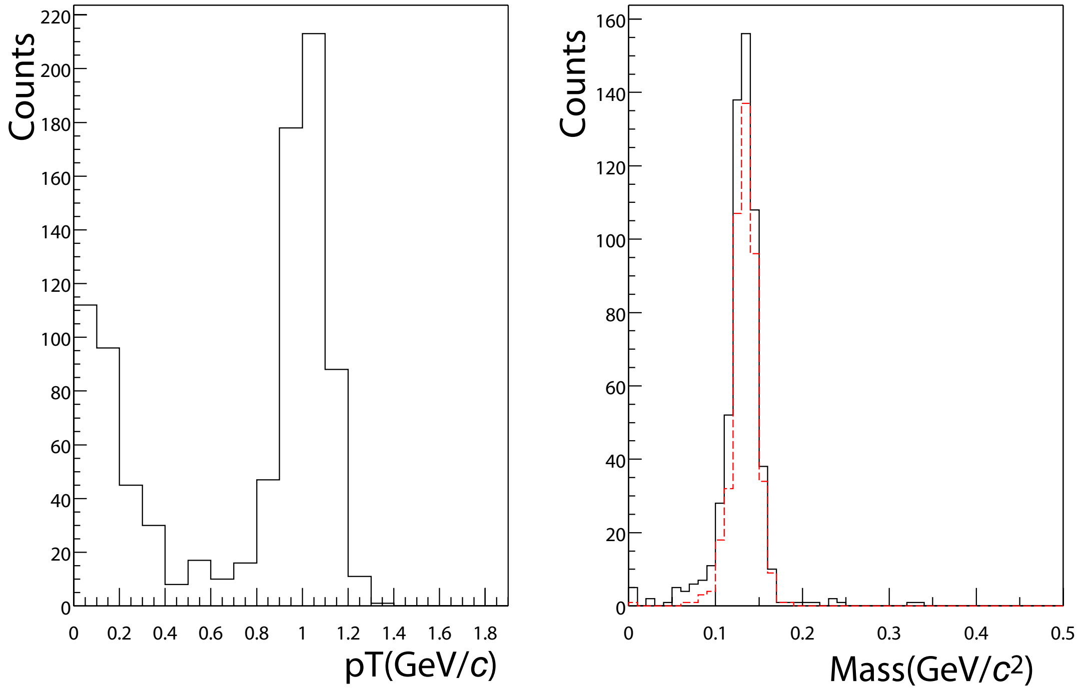

Figure 3.18: *From the single particle GEANT simulation – (left) The p_T distribution obtained with all combinations of all and (right) the invariant mass spectrum obtained with all combinations of clusters for which the reconstructed π^0 has p_T more than 0.5 GeV/c. The red dotted histogram shows a spectrum coming from π^0 from which the both photons can reach the EMCal without any conversion loss.*

3.8.3 Summary of Two Methods

From a comparison of the results from the two methods for estimating the conversion contribution, the 1st method yields larger correction by about 4% than that from the simpler 2nd method. We can't quite understand the reason of the difference from the two methods. By taking the discrepancies as an uncertainty, and adding the uncertainty of 2% on the conversion correction quadratically, the final correction is tabulated in Table 3.4. This correction is multiplicative.

West Arm	1.040±0.028
East Top	1.042±0.028

Table 3.4: *Overall correction ($\epsilon_{\pi^0}^{\mathrm{conv\&albedo}}$) for converting the number of reconstructed π^0's to the number of produced π^0's based on combining in the two methods. The error is systematic error.*

3.9 Cross Section and Systematic Errors

3.9.1 Luminosity Measurement

The machine luminosity is measured by the properties of the intersecting beams: specially, the beam intensities, the transverse dimensions of the collision diamond, and the beam repetition rate. The transverse size of overlap between the beams is measured directly using Van der Meer scan, in other word, Vernier scan. In the scan, one of the beams is systematically swept across the other beam along one axis. By monitoring the rates in a trigger counter and measuring the positions of the two beam, the width of the overlap is measured along one direction. Then, the luminosity is written as

$$L = \frac{f}{2\pi\sigma_v\sigma_h} \times \sum_{i=1,55} (N_1, N_2)_i \ ,$$

where f is the revolution frequency (78kHz) for one bunch in the beam, σ_v and σ_h are the vertical and horizontal width of the beam overlap measured by the scan, and $(N_1, N_2)_i$ is the product of the number of protons in 1-st and 2-nd beams for i-th beam crossing.

During the run when the Van der Meer scan was performed, the cross section for the minimum bias trigger results in 21.8mb. The systematic error is estimated from the three scans to be ±2.8mb at 2 sigma with an additional absolute scale error of ±0.7mb at 1 sigma. We quote the final error on the cross section as the linear sum of half of the 2 sigma error, that is ±2.1 (9.6%). Based on an examination of the available world data, the inelastic cross section is 42.2 ± 1.9 mb for collisions at $\sqrt{s}$ of 200GeV. Consequently, the trigger efficiency of events is 0.516 ± 0.051 (9.8%)

3.9.2 Cross Section for Each Triggers

The invariant π^0 cross section, $E\cdot d^3\sigma/dp^3$, is equal to:

$$\begin{aligned} E\cdot d^3\sigma/dp^3 &= \frac{1}{2\pi}\cdot\frac{1}{p_T}\cdot\frac{d^2\sigma}{dp_T dy} \\ &\simeq \frac{1}{2\pi}\cdot\frac{1}{p_T}\cdot\frac{d^2\sigma}{dp_T d\eta}, \end{aligned}$$

where p_T is the transverse momentum of the pion, y is the rapidity, and η is the pseudo-rapidity. The approximation of $y \sim \eta$ involves 1% correction at p_T of 1 GeV/c, 1/4% at 2 GeV/c, which is negligible relative to the other systematic error.

The cross section for the minimum bias trigger is calculated according to the following expression:

$$E \cdot d^3\sigma/dp^3 = \frac{1}{2\pi} \cdot \frac{1}{\mathcal{L}} \cdot \frac{N_{\pi^0}^{\rm corr}}{p_T \cdot \Delta p_T} \quad ({\rm mbGeV}^{-2}c^3) \ ,$$

with

$$\begin{aligned} N_{\pi^0}^{\rm corr} &= \frac{N_{\pi^0}^{\rm mini} \cdot C_{\pi^0}^{\rm reco}(p_T) \cdot \epsilon_{\pi^0}^{\rm conv\&albedo}}{\epsilon_{\pi^0}^{\rm mini}(p_T)} \ , \text{ and} \\ \mathcal{L} &= \frac{N_{\rm trig}^{\rm mini}}{21.8} \quad ({\rm mb}^{-1}) \ , \end{aligned}$$

where Δp_T is the width of the p_T bin, $N_{\pi_0}^{\rm mini}$ is the number of reconstructed π^0 in the minimum bias sample after the background subtraction, $\epsilon_{\pi^0}^{\rm mini}(p_T)$ is the trigger efficiency of π^0 in the minimum bias trigger, $C_{\pi^0}^{\rm reco}(p_T)$ is the reconstruction efficiency, $\epsilon_{\pi^0}^{\rm conv\&albedo}$ is the conversion and albedo correction, $N_{\rm trig}^{\rm mini}$ is the number of the minimum bias triggered events, and 21.8 (mb) is the effective total inelastic cross section as described in Section 3.9.1.

For the high-p_T events, the cross section is obtained similarly as that in the minimum bias events with

$$\begin{aligned} N_{\pi^0}^{\rm corr} &= \frac{N_{\pi^0}^{\rm high} \cdot C_{\pi^0}^{\rm reco}(p_T) \cdot \epsilon_{\pi^0}^{\rm conv\&albedo}}{\epsilon_{\pi^0}^{\rm high}(p_T) \cdot \epsilon_{\pi^0}^{\rm mini}(p_T)} \ , \text{ and} \\ \mathcal{L} &= \frac{N_{\rm trig}^{\rm mini}}{21.8} \cdot \frac{N_{\rm trig}^{\rm high}}{N_{\rm trig}^{\rm mini.and.high}} \quad ({\rm mb}^{-1}) \ , \end{aligned}$$

where $N_{\pi_0}^{\rm high}$ is the number of reconstructed π^0 in the high-p_T trigger sample, $\epsilon^{\rm high}(p_T)_{\pi^0}$ is the trigger efficiency of π^0 in the high-p_T trigger, $N_{\rm trig}^{\rm high}$ is the number of the high-p_T trigger, and $N_{\rm trig}^{\rm mini.and.high}$ is the number of the high-p_T trigger in which the minimum bias trigger is also fired. In both of these expressions, the pseudo-rapidity (η) and the azimuthal (ϕ) range are corrected implicitly by $C_{\pi^0}^{\rm reco}(p_T)$ from the PHENIX acceptance under the assumption that the distributions of the π^0 production for these variables are flat.

3.9.3 PbGl Analysis

The same data-set in the p+p collisions for both triggers is analyzed for the PbGl in an independent method and group. We combine two independent analyses for the final result as described in the next section, because the combination of two results from two detectors has an advantage in terms of reducing both systematic and statistical errors. In this section, a short summary of the π^0 analysis using the PbGl is described.

One of the large differences of two analyses between the PbSc and the PbGl is on their energy calibration for each tower. As described in Section 2.4, the PbGl is lead-glass Čerenkov calorimeter. When a charged hadron penetrates the tower from the surface to the backward, no ionization energy is deposited unlike the PbSc. However, the δ-electrons emitted by such the charged particle due to its energy loss may produce Čerenkov light. The Čerenkov light from the δ-electrons are not produced into the ordinary direction like the photon shower but typically into the transverse direction along to the charged hadron, so they may or may not reflected in the wall of the PbGl towers. The energy distribution in such process is partially reproduced by the GEANT simulation after careful research about the reflection material surrounding each tower. Finally, we decide not to use the energy distribution by the charged hadron for the purpose of the energy calibration.

Instead of using the charged particle, the photon are used for the calibration for towers. The towers with similar incident angle are assumed to have identical energy distribution. This assumption is used for the energy calibration. The local slope in the energy distribution by the photons with similar angle is determined for each tower and used to extract the gain.

Another large difference of two analyses is due to the energy distribution by electrons and positrons. As discussed in Section 3.5.3, we try to extract the E/p distribution using electron and positron samples. The peak of the distribution is skewed to be lower than 1.0. We expect it is caused by the TZR detector, which is sitting only in front of the PbGl. Finally, we decide not to use the E/p distribution for determining the energy resolution.

Instead of using electrons and positrons, the energy resolution and its uncertainty is determined only from the π^0 width and to be $\sigma_E/E = 12 \pm 3\% \oplus 8.5\%/\sqrt{E(GeV)}$, where $\oplus$ denotes a quadratic sum. The constant term of 12% is larger than 4.7% for the PbSc, which may be due to the poor assumption in the gain adjustment, so that the smearing effect on the p_T distribution is larger than that in the PbSc. Although its uncertainty of $\pm 3\%$ is similar with $\pm 2.6\%$ for the PbSc, the propagated error on the π^0 yield from the uncertainty is larger than that for the PbSc. The order of the propagated error on the π^0 yield is similar to the systematic uncertainty due to the absolute energy scale.

The uncertainty of the absolute energy scale, which is 1.5%, is another large contribution of the systematic error. The uncertainty on the π^0 yield is determined using the FastMC as described in Section 3.5 and to be 12% at p_T more than 8GeV/c, which is slightly larger than that (11%) for the PbSc. The total systematic error after summing all contributions quadratically for the PbGl is larger than that for the PbSc.

Because of the larger systematic error, the combination of two results doesn't reduce the total systematic error so much. However, in terms of statistical error, we still have an advantage for combining two results. Also we like to emphasize that the consistency of two independent analyses is important to check the reliability of the result.

3.9.4 Combination of Two Results

In this section, the procedure to combine two subsystems and two triggers are described. The two results from two different triggers, the minimum bias and the high-p_T trigger, are consistent within the statistical error in the common p_T range. Because the statistical error in the minimum bias sample is worse than that in the high-p_T trigger, the weighted result would be contributed only by the high-p_T trigger. However, the trigger efficiency of π^0 in the high-p_T trigger ($\epsilon_{\pi^0}^{\rm high}(p_T)$) becomes smaller as p_T decreases and the error of the efficiency increases. So we decide to use the result of the high-p_T trigger for more than 4GeV/c, and that of the minimum bias trigger for others.

The two results from two independent subsystems, the PbSc and the PbGl, are consistent within their systematic and statistical errors in measured p_T range. Figure 3.19 shows the comparison of two results in the top panel. the difference of the two in the bottom panel. The systematic errors of the two except the common errors are added quadratically and shown in the bottom panel. A fit by a constant results in that the χ^2 is small (3.8). This fact indicates that the systematic errors are overestimated or correlated. We obtain the weighted average of the cross section as described in the Particle Data Group [16]. The weighted average of the measured value $\bar{N}$ with error $\delta\bar{N}$ at each p_T bin is determined through

$$\bar{N}(p_T) \;\pm\; \delta\bar{N}(p_T) = \frac{\sum_i \, w_i(p_T)\, N_i(p_T)}{\sum_i \, w_i(p_T)} \;\pm\; \left(\sum_i \, w_i(p_T)\right)^{-1/2} ,$$

where $w_i(p_T)$ is $1/(\delta N_i(p_T))^2$, N_i and δN_i are the measured value and the error respectively by $i = 1$ (PbSc), 2 (PbGl). The total error $\delta N(p_T)$ is as follows:

$$(\delta N_i(p_T))^2 = (\overline{\delta N_i^{stat}}(p_T))^2 + (\overline{\delta N_i^{syst}}(p_T))^2 \ .$$

The separate statistical and systematic terms are calculated using the expressions:

$$\begin{aligned}
\overline{\delta N_i^{stat}}(p_T) &= \sqrt{\frac{1}{N}\,\frac{w_i(p_T)\,(\delta N_i^{stat}(p_T))^2}{\sum_i w_i(p_T)}} \ , \text{ and} \\
\overline{\delta N_i^{syst}}(p_T) &= \sqrt{\frac{1}{N}\,\frac{w_i(p_T)\,(\delta N_i^{syst}(p_T))^2}{\sum_i w_i(p_T)}} \ .
\end{aligned}$$

The common systematic errors for both measurements (PbSc and PbGl) are not included in the calculations above. They are 3% on the trigger efficiency of

π^0 in the minimum bias trigger ($\epsilon_{\pi^0}^{\mathrm{mb}}(p_T)$) and 9.6% of global normalization error. In the final result, the former error is quadratically added to the systematic errors calculated from the equation and the latter one is quoted separately.

Finally, the averaged p_T is defined as p_T for which the cross section is equal with its average over the bin. To calculate the averaged p_T, the data points are fitted with Hagedorn-type function [114], $f(p_T) = c(1+p_T/p_0)^{-n}$ iteratively. The fitted function is used to calculate the averaged p_T.

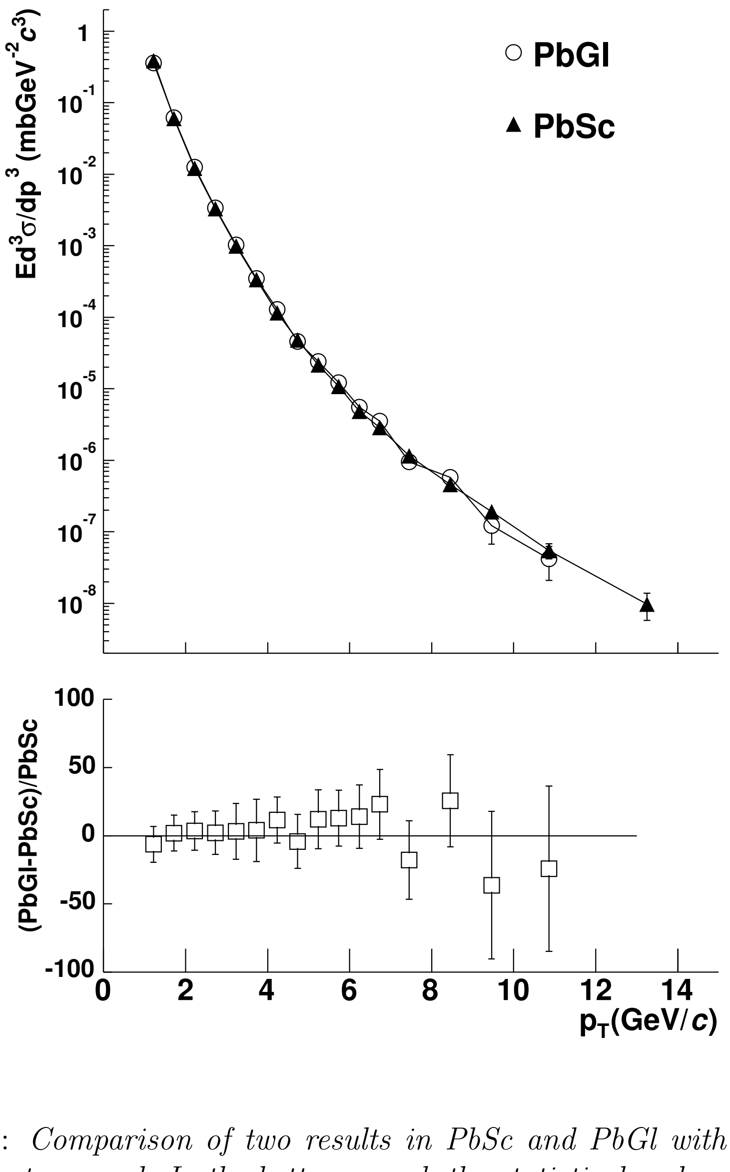

Figure 3.19: *Comparison of two results in PbSc and PbGl with only statistical errors in the top panel. In the bottom panel, the statistical and systematic (except the common errors) errors are added quadratically.*

Chapter 4

Results and Discussion

4.1 Results

The differential cross section of the π^0 production in the p+p collisions at $\sqrt{s}$ of 200GeV and the systematic error for each PbSc and PbGl are tabulated in Table 4.1 and Table 4.2. Figure 4.1 shows the cross section as a function of p_T with only the statistical error in the top panel and the statistical and systematic error in the bottom panel of the figure. In Table 4.2, the systematic uncertainty on $N^{\mathrm{raw}}_{\pi^0}$ is tabulated as yield extraction. Two errors related to the energy scale and the acceptance stability are selected from the systematic uncertainty on $C^{\mathrm{reco}}_{\pi^0}(p_T)$. The rest of the systematic uncertainty on $C^{\mathrm{reco}}_{\pi^0}(p_T)$ and the systematic uncertainty on $\epsilon^{\mathrm{high}}_{\pi^0}(p_T)$ and $\epsilon^{\mathrm{mini}}_{\pi^0}(p_T)$ are added quadratically and tabulated as the error on yield correction in the table.

The 8th order of magnitude on the cross section is obtained in the wide p_T range from 1.22 to 13.25GeV/c. The spectrum as shown in the top panel shows a smooth curve as a function of p_T. When we connect two adjoining points by a straight line, we can define a local slope as the slope of the line for each pair of data points. The local slopes are not constant in the measured p_T range. Specifically, they are steeper in the lower p_T than that in the higher p_T. This shape is very typical in the particle production in the high energy collisions. In the next section, we will discuss the shape in terms of the x_T scaling.

Because the two results of the PbSc and the PbGl are consistent within their statistical and systematic error, the combining two results allow us to reduce the errors. The systematic error of 9.6% on the global scale coming from the uncertainty of the luminosity measurement is not shown in both panels in the figure. The uncertainty of the energy scale is the largest contribution on the systematic error. The total systematic error depends on p_T and are from 7% to 15% as shown as the bands in the bottom panel. For p_T higher than 8GeV/c, the statistical error is larger than the systematic error. The statistical error at the highest p_T, 13.25GeV/c, is about 40%.

p_T bin (GeV/c)	$\bar{p_T}$ (GeV/c)	inv. cross section (mb·GeV^{-2}·c^3)	stat. error (%)	syst. error (%)
1.0-1.5	1.22	$3.73 \cdot 10^{-1}$	1.6	7.3
1.5-2.0	1.72	$6.05 \cdot 10^{-2}$	1.8	7.1
2.0-2.5	2.22	$1.22 \cdot 10^{-2}$	2.5	7.1
2.5-3.0	2.73	$3.31 \cdot 10^{-3}$	3.6	7.2
3.0-3.5	3.23	$9.98 \cdot 10^{-4}$	5.7	7.3
3.5-4.0	3.73	$3.39 \cdot 10^{-4}$	7.3	7.7
4.0-4.5	4.23	$1.19 \cdot 10^{-4}$	2.4	8.3
4.5-5.0	4.73	$4.73 \cdot 10^{-5}$	4.2	8.5
5.0-5.5	5.23	$2.21 \cdot 10^{-5}$	5.0	8.7
5.5-6.0	5.74	$1.11 \cdot 10^{-5}$	4.5	9.2
6.0-6.5	6.24	$5.00 \cdot 10^{-6}$	6.3	9.5
6.5-7.0	6.74	$3.00 \cdot 10^{-6}$	7.7	9.8
7.0-8.0	7.45	$1.08 \cdot 10^{-6}$	8.8	10.1
8.0-9.0	8.46	$4.85 \cdot 10^{-7}$	12.0	10.8
9.0-10.0	9.46	$1.64 \cdot 10^{-7}$	19.3	11.0
10.0-12.0	10.86	$5.07 \cdot 10^{-8}$	22.3	11.7
12.0-15.0	13.25	$9.76 \cdot 10^{-9}$	41.3	15.6

Table 4.1: *Invariant cross section for inclusive π^0 production in p+p collisions at $\sqrt{s}$=200 GeV with the statistical uncertainty, and the systematic uncertainty for each p_T bin. The absolute normalization error of 9.6% is not included.*

	% Error (PbSc)		% Error (PbGl)	
p_T (in GeV/c)	1.2	10.9	1.2	10.9
Energy Scale	3	11	6	12
Yield Extraction	7	4	5	5
Yield Correction	3	6	6	11
Acceptance Stability	4.5	4.5	3	2
Total	9	14	10	17

Table 4.2: *Summary of the sources of systematic errors on the π^0 yields and the total systematic error for p_T of 1.2 and 10.9 GeV/c. The absolute normalization error of 9.6% is not listed.*

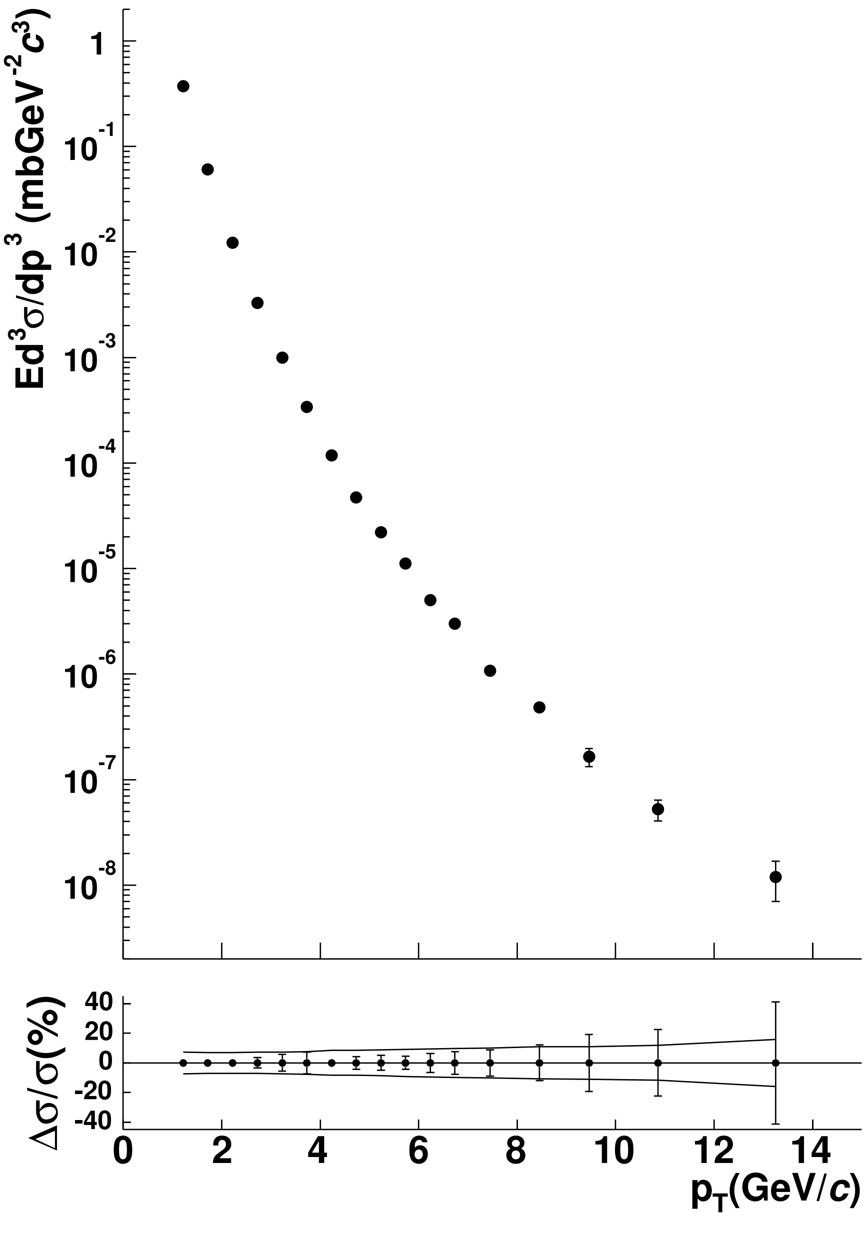

Figure 4.1: *(top) Invariant cross section for inclusive π^0 production with only the statistical error bar. (bottom) Statistical (bar) and systematic (band) errors. The absolute normalization error of 9.6% is not shown.*

In Section 4.2, we will compare the obtained result with the results in other experiments. The x_T scaling property of the present result will be discussed in Section 4.3. As described earlier, this work is motivated by two physics interests: providing a testing ground of pQCD and providing a reference data for the QGP search. We will discuss each in Section 4.4 and Section 4.5, respectively.

4.2 Comparison with Other Experiments

In this section, we compare the present result with results of the π^0 production in different $\sqrt{s}$ at pseudo-rapidity (η) of around 0 from other experiments. As discussed in Section 1.1, the π^0 production at $|\eta| \approx 0$ were measured in the $p+p$ collisions at $\sqrt{s}$ up to 63GeV and in the $p+\bar{p}$ collisions at $\sqrt{s}$ up to 540GeV. All of the published papers and preprints of the π^0 measurement are carefully examined and hep database [115] are used for the numerical values. Some experiments don't provide their numerical values in either paper or database.

In some experimental setup, two photons decayed from a π^0 with higher p_T are unresolved because the opening angle of two photons are smaller than the position resolution of the detectors. So the signal of π^0 in the detector cannot be distinguished from η decay and direct-γ. Such η and direct-γ contribution were not subtracted in some of them. The η [116] production was estimated as between 5% to 30% and the direct-γ [117, 118] production was smaller than 30%, which depend on their $\sqrt{s}$ and p_T. In total, their yield compared with the π^0 yield is not bigger than 50%. Because the contribution depends on the detector configuration strongly, we decide not to correct the effect in the data.

Some of the experiments at ISR colliders did not provide the systematic error on the cross section but on the scale of the measured p_T. We assign 25% error on the cross section when the systematic error on p_T is 5% , which was quoted by most of the experiments. Many of the experiments provided their mean p_T weighted by the measured cross section for each p_T bin. However, the results by R806 [53, 54] and E706 [64] were shown only in the p_T bin, *i.e.*, the minimum and maximum p_T of the each p_T bin. In the next section, we will compare the results with an NLO pQCD calculation. For the purpose of comparing all data within the same framework, we calculate the mean p_T value for each p_T bin for only the E706 data since their bin width is too large as discussed in Appendix D.

Figure.4.2 shows a comparison of the obtained result at $\sqrt{s}$ of 200GeV with other results at $\sqrt{s}$ between 20GeV and 540GeV. The data in the figure are scaled by a constant so that we can compare the slope as a function of p_T. The p_T distributions for each $\sqrt{s}$ without the scale are shown in Appendix D. The present result labeled as PHENIX covers an intermediate $\sqrt{s}$ region between the ISR and the SPS colliders. The obtained result provides a unique test for the pQCD.

For the lowest $\sqrt{s}$ of $\approx$ 20GeV in the figure, the local slope at p_T from 1 to

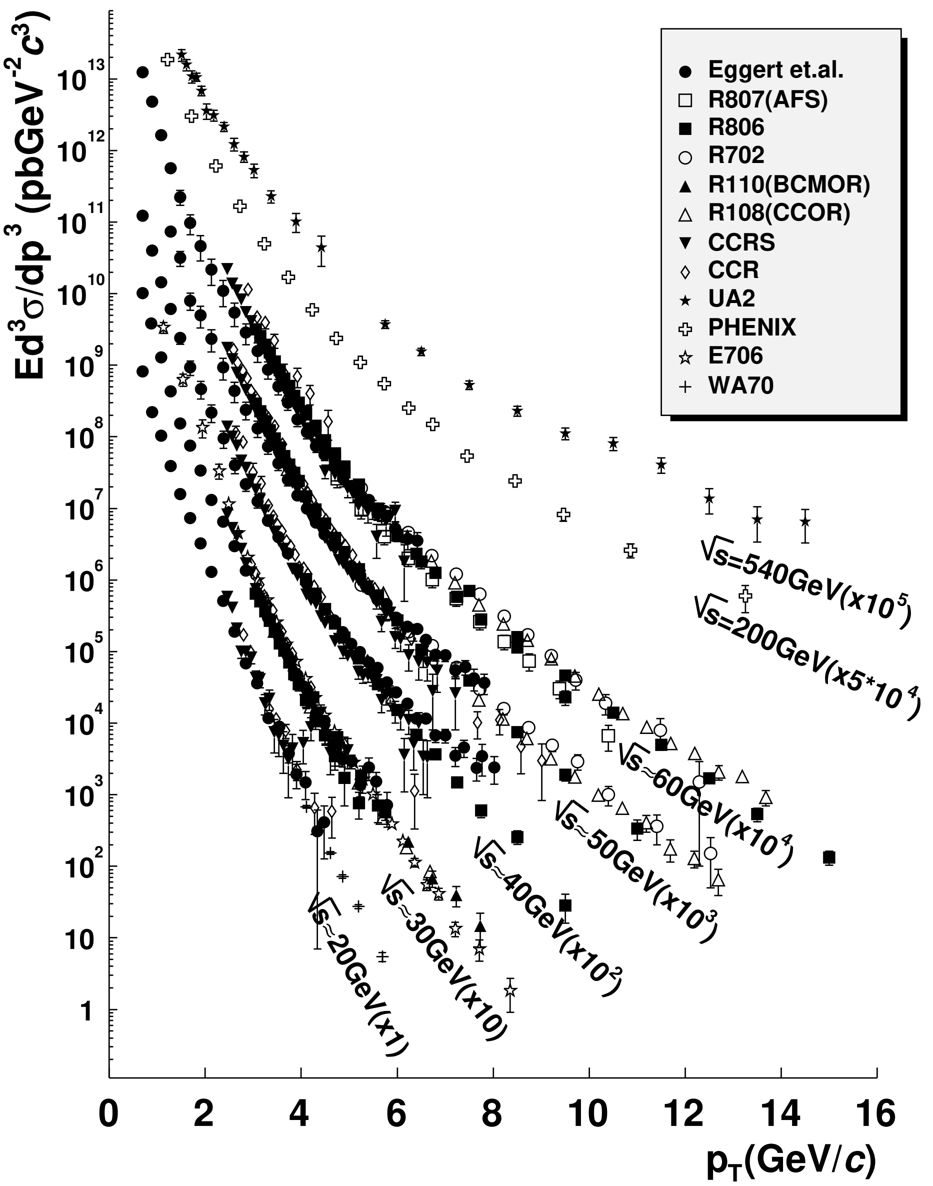

Figure 4.2: *Comparison of the inclusive π^0 production at $\sqrt{s}$ between 20GeV and 540GeV. Only the statistical errors are shown.*

6GeV/c doesn't change. However, as $\sqrt{s}$ goes higher, the distributions show a sort of bend at p_T of around 5GeV/c. especially for $\sqrt{s}$ of 200GeV and 540GeV. In those $\sqrt{s}$ region, the slope at the higher p_T than the bend point becomes flatter than that at lower p_T, which can be explained by the hard interaction in hadrons. Unlike the behavior at the higher p_T, the slope in lower p_T shows less dependence on $\sqrt{s}$. As p_T becomes lower, all the slopes at different $\sqrt{s}$ seem to converge into a similar slope. This independent behavior on $\sqrt{s}$ in the low p_T may be explained by soft interaction in the collisions. From the above comparison, we will discuss with the present result in terms of hard and soft interaction.

4.3 x_T Scaling

The point-like structure in protons was observed in deep inelastic scattering (DIS) in 1968 [3]. The proton structure function is independent of Q^2 and is scaled by a scaling variable. Bjorken [119] suggested that the fact is due to the point-like interaction of partons. In the similar analogy of the point-like scattering in the DIS, the x_T scaling property, where the x_T is defined as $2p_T/\sqrt{s}$, in the hadron production from hadron collisions were introduced by Cahalan *et al.* [120]. In this section, we examine the x_T scaling of the present result together with other results.

The basic formalism of the hadron production from hadron collisions is written as Equation (1.2) in Section 1.1. For the hadron production at the pseudo-rapidity of 0, the equation can be approximated by the following formulae:

$$E\frac{d^3\sigma}{dp^3} \approx (\sqrt{s})^{-n} \times \mathcal{F}(x_T) , \tag{4.1}$$

where n is constant named as the power index and $\mathcal{F}(x_T)$ does not depend on $\sqrt{s}$.

The naive parton model has $n = 4$ in the leading order and $n = 4 + \alpha$ in the next-to-leading order. In the approximation, however, there are two assumptions: 1) the Q^2 scaling of the PDF and FF 2) the coupling constant (α_s) is independent of Q^2. Since the assumptions are violated as discussed in Section 1.1, the power index is not constant and is a function of x_T and $\sqrt{s}$. As $\sqrt{s}$ increases, the power index is expected to decrease since the running coupling constant decreases and Q^2 scale breaking becomes smaller and smaller. The R108 collaboration [51] has reported $n = 6.3$ in $\sqrt{s}$ between 20 and 63GeV and in the x_T range between 0.1 and 0.5. In this section, we follow their conclusion. We examine the obtained result together with other results which were obtained at $\sqrt{s}$ of more than 63GeV in the form of $\sqrt{s}^{6.3} \times E\frac{d^3\sigma}{dp^3}$.

Figure 4.3 shows a comparison between the present result and other results at $\sqrt{s}$ between 60 and 540GeV. Only the data points at p_T more than 4GeV/c for

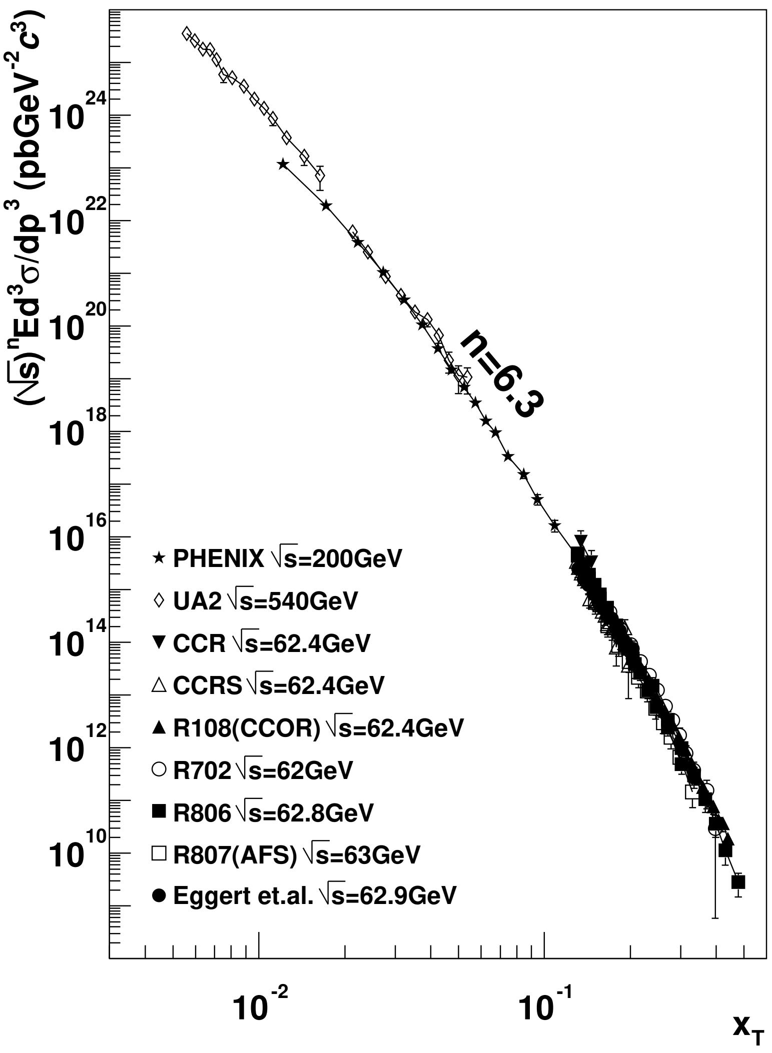

Figure 4.3: $\sqrt{s}^{6.3} \times E\frac{d^3\sigma}{dp^3}$ *at* $\sqrt{s}$ *between 60 and 540GeV. The statistical errors are shown in the figure. Only the data points at* p_T *more than 4GeV/c at* $\sqrt{s}$*=63GeV and 2GeV/c at* $\sqrt{s}$ *>100GeV are compared. The present result labeled as PHENIX together with other results shows the* x_T *scaling property.*

63GeV data and 2GeV/c for 200GeV and 540GeV are used in the comparison. There is a common range of the measured x_T between the present result and other results at $\sqrt{s}$ of 540GeV by the UA2 collaboration and of 63GeV at the ISR collider. The figure shows good agreement on each other in the measured x_T range between 0.005 and 0.5 and in $\sqrt{s}$ range between 60 and 540GeV. We conclude that the scaling property reported by the R108 collaboration is valid at $\sqrt{s}$ up to 540GeV. This scaling property indicates that the present data are dominated by the point-like interaction.

4.3.1 Meson Exchange Model

In this section, one of models for the soft interaction is explained and is used to investigate whether the x_T scaling property can be described by the model.

The constituent interchange model (CIM) [121] was proposed in 1972. The model predicts that the hadronic bremsstrahlung from the incident particles and the interaction between the produced meson and quark can describe the particle production with large transverse momentum in hadron collisions. In the case of proton collisions, the proton beam behaves effectively like a meson beam with much lower energy in the model. Figure 4.4 represents a schematic view of basic idea in the model. Unlike pQCD, this model is based on the meson (soft)

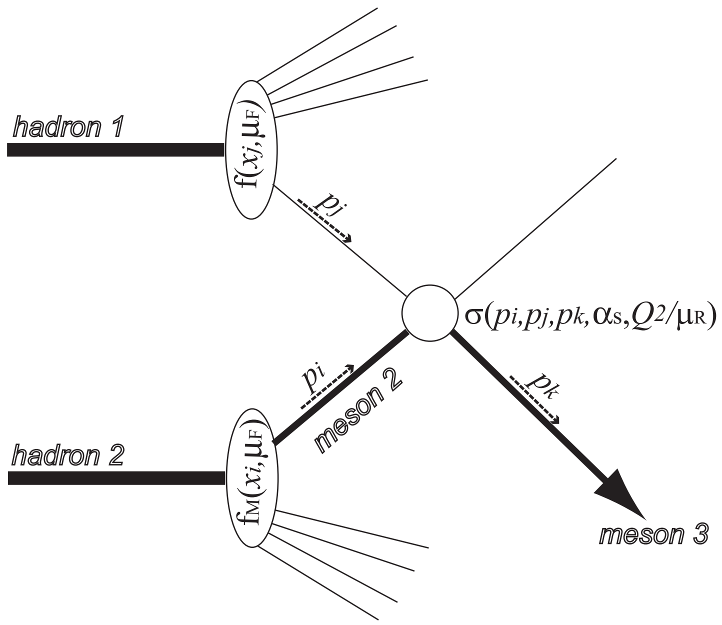

Figure 4.4: *Diagram for the meson production in the constituent interchange model (CIM) [121] in the reaction of* $1 + 2 \rightarrow 3$. *A virtual meson is produced through a bremsstrahlung process from hadron.*

interaction. As similar to Equation (4.1), the model calculation suggests that the differential cross section can be written as the following formulae:

$$\begin{aligned} E\frac{d^3\sigma}{dp^3} &= C \cdot p_T^{-n} \cdot (1-x_T)^m \\ &= \sqrt{s}^{-n} \times C' \cdot x_T^{-n} \cdot (1-x_T)^m, \end{aligned}$$

where C and C' are constant and n is named as power index. The prediction of the CIM model is $n = 8$ and $m = 9$.

The first measurement of the power index for π^0 was performed by the CCR [47] collaboration. The Chicago-Princeton (CP) [122] collaboration concluded $n = 8.2 \pm 0.5$ for $\pi^\pm$ production and summarized that all of the existing results at that time are consistent with $n = 8$. Figure 4.5 shows $\sqrt{s}^n \times E\frac{d^3\sigma}{dp^3}$ measured by the CCR [47] and the CCRS [48] collaborations with varying the power index of 6.3 and 8.6. The index of 8.6 is the best value obtained by the CCR collaboration. The comparison in various $\sqrt{s}$ between 20 and 63GeV shows that the data agrees to the prediction with $n = 8.6$ better than that with $n = 6.3$. Due to the

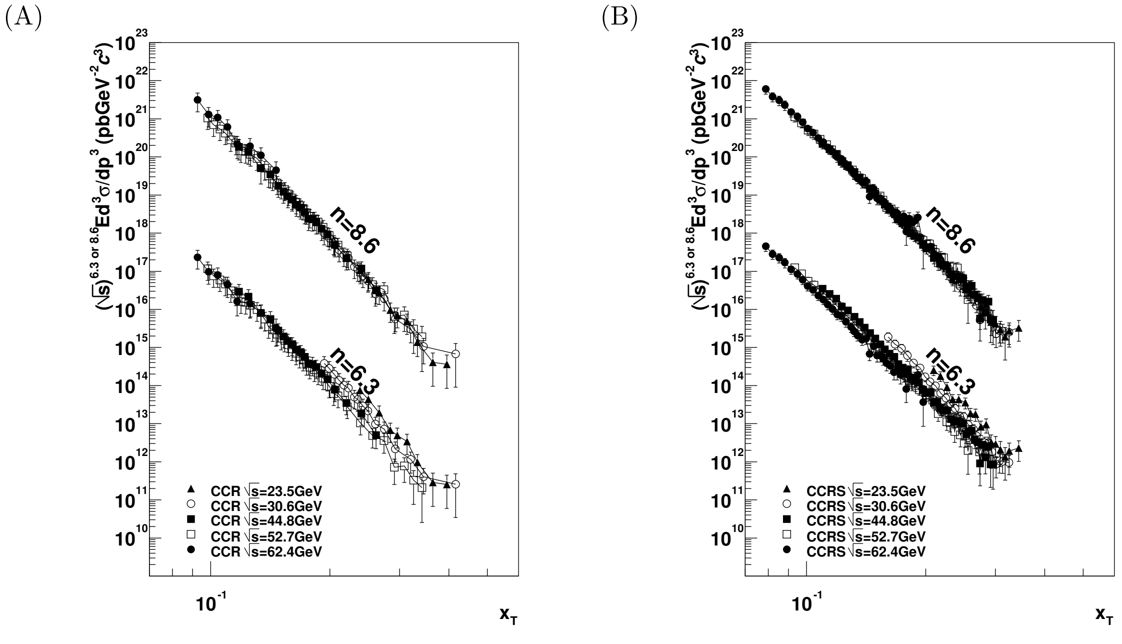

Figure 4.5: $\sqrt{s}^n \times E\frac{d^3\sigma}{dp^3}$ *in varied* $n = 8.6$ *(upper) and* $n = 6.3$ *(lower) by (A)the CCR [47] and (B)the CCRS [48] collaborations at* $\sqrt{s}$ *between 20 and 63GeV. Due to the limited statistics, most of the data are sitting at the* x_T *of less than 0.3. Only the statistical errors are shown. The upper comparison of* $n = 8.6$ *shows better agreement than the lower one.*

limited statistics, most of the data points were in $x_T < 0.3$ region.

However, a pQCD calculation considering only the interaction between quarks and gluons predicts the power index of n=4 in the leading order and $n = 4 + \alpha$ in the higher order. The $\sqrt{s}$ dependence on the power index can be a good probe for distinguish of two different models. Figure 4.6 shows the comparison made by the R806 [53] and the R108 [51] collaboration. The $n = 6.3$ is the best value from the R108 collaboration in their x_T and $\sqrt{s}$ range as shown in the figure. The two comparison in Figure 4.5 and Figure 4.6 are performed in same $\sqrt{s}$ range. The only difference is that the latter are performed in higher x_T region because of their higher statistics of the data.

This discrepancy is very interesting for understanding the present result. As discussed in the previous section, the steep slope of the obtained result at the lower p_T may be contributed by the soft interaction. We examine the present result together with other results in the form of $\sqrt{s}^{8.6} \times E\frac{d^3\sigma}{dp^3}$. Figure 4.7 shows a comparison between the present result and other results at $\sqrt{s}$ between 60 and 540GeV when using the power index of $n = 8.6$. Only the data points at p_T more than 4GeV/c for 63GeV data and 2GeV/c for 200GeV and 540GeV are used in

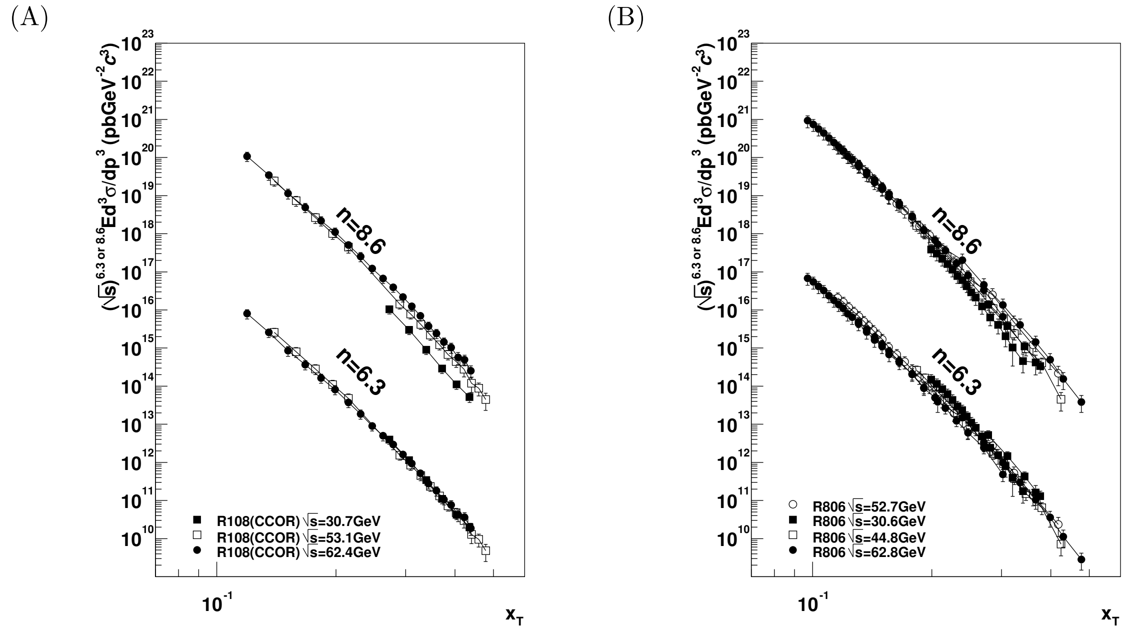

Figure 4.6: $\sqrt{s}^n \times E\frac{d^3\sigma}{dp^3}$ *in varied* $n = 8.6$ *(upper) and* $n = 6.3$ *(lower) by (A)the R806 [53] and (B)the R108 [51] collaborations at between 20 and 63GeV in the* x_T *of up to 0.5. Only the statistical errors are shown. The upper comparison (*$n = 8.6$*) start to diverge at the* x_T *of more than* 0.3. *The R108 collaboration concluded* $n = 6.3$ *is the best value in their kinematic range.*

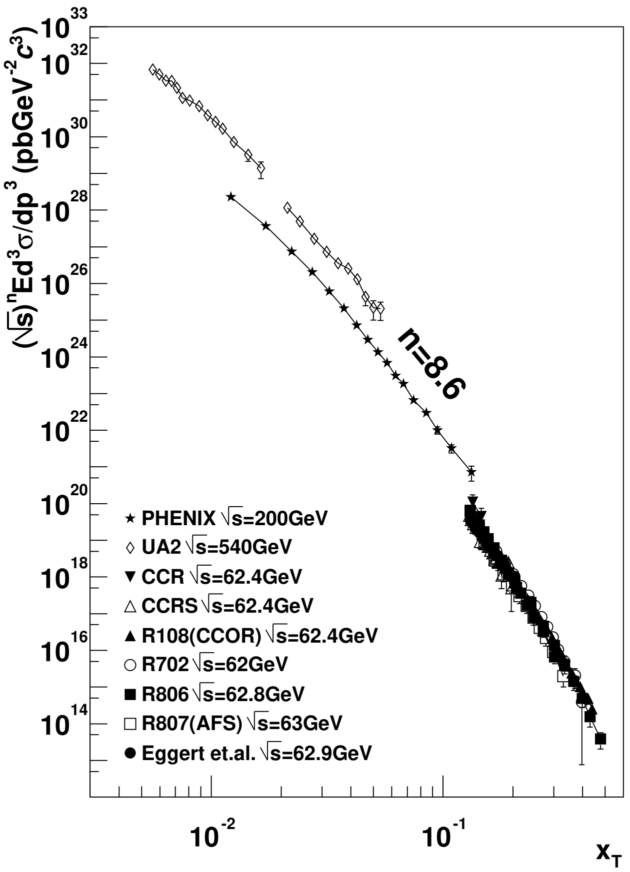

Figure 4.7: $\sqrt{s}^{8.6} \times E\frac{d^3\sigma}{dp^3}$ *at* $\sqrt{s}$ *between 60 and 540GeV. The statistical errors are shown in the figure. Only the data points at* p_T *of more than 4GeV/c at* $\sqrt{s}$*=63GeV are compared. There appears an apparent discrepancy between data.*

the comparison. The figure shows a clear dis-connectivity in the entire x_T range. The local slope of the present result and other results are apparently different.

A conclusion in this section is that the present result at $\sqrt{s}$ of 200GeV provides an important reference to distinguish the power index at higher $\sqrt{s}$ region. The simple comparison shows the CIM model fails to describe the x_T scaling property. We conclude the present result, the π^0 production at $\sqrt{s}$ of 200GeV, is not dominated by the meson exchange interaction, which is one of models for the soft interaction. In the next section, we describe an NLO pQCD calculation and compare the present result with the calculation.

4.4 Comparison with NLO pQCD

In this section, the present data is compared with an NLO pQCD calculation in the context of the motivation, which is providing a testing ground of the pQCD. First of all, we explain the parameters of the calculation.

An NLO pQCD calculation is performed using the PHOX [123] software, whose original code was created by F. Aversa *et al.* [65] and P. Aurench *et al.* [66]. The CTEQ6M [24, 75] is used for the parton distribution function (PDF) and KKP [43] is used for the fragmentation function (FF). Both renormalization and factorization scales are set to be equal ($\mu = \mu_F = \mu_R$) and to be varied by $1/2\ p_T$, p_T, and $2\ p_T$.

Figure 4.8 shows the present data compared with the NLO pQCD calculation. The three calculations using the scales of $1/2\ p_T$, p_T, and $2\ p_T$ are shown by three solid lines from top to bottom, respectively. In the pQCD calculation, the factorization and renormalization scale may approach the starting scale Q^0 (=1GeV) of the QCD evolution. So the calculation using the scale of $1/2\ p_T$ are performed at p_T of more than 2GeV/c. The present data labeled as PHENIX is consistent with the calculation using the scale of $\mu = p_T$ (middle line) in the lower p_T region. In the higher p_T region, the data are sitting between the calculations at $\mu = p_T$ and $\mu = 2p_T$. The data are consistent with the NLO pQCD calculation within their deviation when using the three different scales. We conclude that the NLO pQCD calculation can describe the present data.

4.4.1 Comparison of Fragmentation Functions.

In this section, we examine the different fragmentation functions. We explain that the present data provides an ideal reference for the determination of the fragmentation function, especially from the gluon jet.

Figure 4.9 shows ratios of the present data to the NLO pQCD calculation at the scale of $\mu = p_T$ using various fragmentation functions (FF): Kretzer [42], BKK [41], and KKP [43] fragmentation functions from top to bottom. Also the ratios of the pQCD calculations at $\mu = 1/2p_T$, $\mu = p_T$, and $\mu = 2p_T$ to that at $\mu = p_T$ are shown as solid lines for each FF.

As well as discussed in previous section, the NLO pQCD calculation using KKP FF can describe the present data at the scale of $\mu = p_T$ in the lower p_T and at the scale of $\mu = 2p_T$ in the higher p_T. The NLO pQCD calculation using BKK FF shows similar behavior as that using KKP FF except of the global normalization. The ratio to the BKK FF is shifted by a factor of about 1.5 from the ratio to the KKP FF. Nevertheless, we conclude that the NLO pQCD calculation using BKK FF describes the present data. From the above comparison in both FFs, a large uncertainty on choices of the renormalization and factorization scales of $\pm 50\%$ remains in the NLO pQCD calculation. However, the NLO pQCD calculation using Kretzer FF shows very different behavior. The

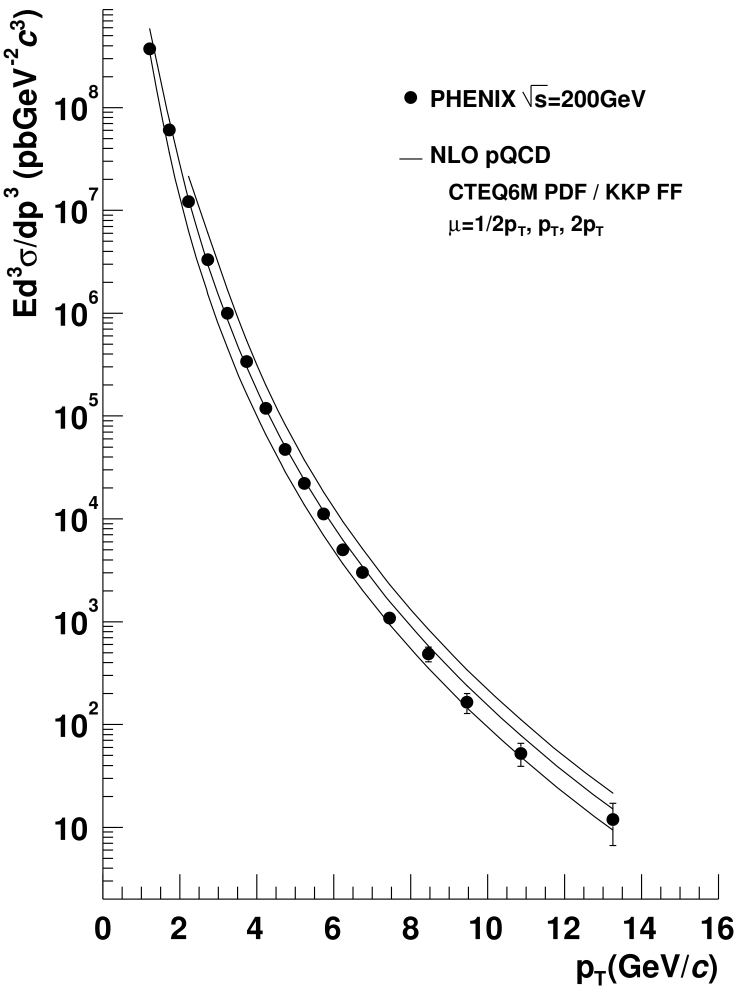

Figure 4.8: *Comparison Differential cross section of* π^0 *production at* $\sqrt{s}$ *of 200GeV an NLO pQCD calculations with CTEQ6M [24, 75] PDF and KKP [43] FF are shown in three scales of* $1/2p_T$ *(top),* p_T *(middle), and* $2p_T$ *(bottom). Only the statistical errors are shown.*

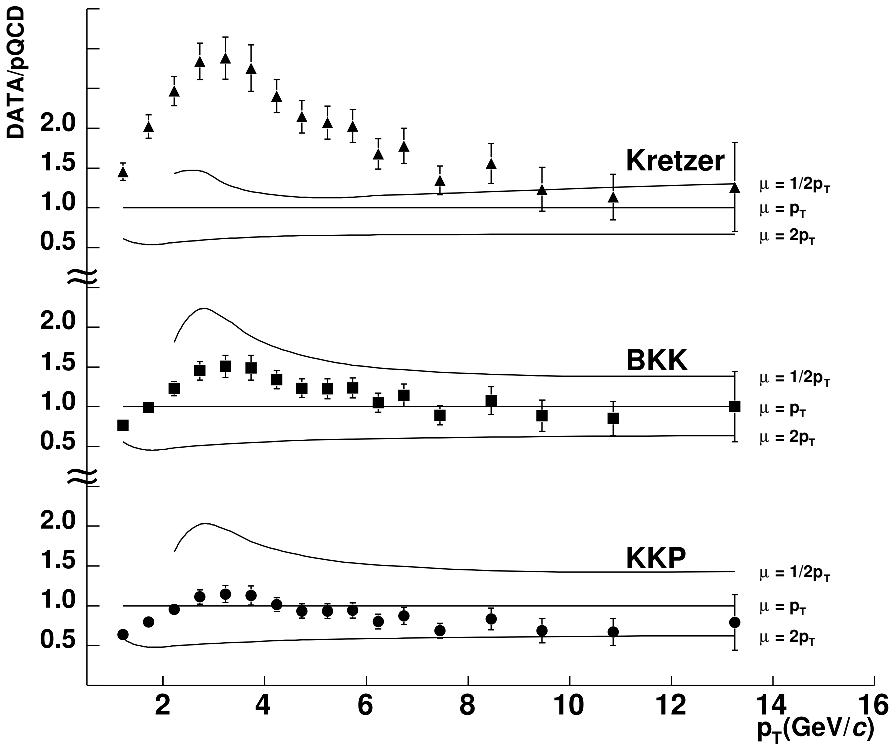

Figure 4.9: *Ratios of the present data with only the statistical error to the NLO pQCD calculations at the scale of $\mu = p_T$ when using Kretzer [42], BKK [41], and KKP [43] fragmentation functions. The ratios of the pQCD calculations at $\mu = 1/2p_T$, $\mu = p_T$, and $\mu = 2p_T$ to that at $\mu = p_T$ are shown as solid lines, respectively. The CTEQ6M [24, 75] PDF are used commonly.*

figure shows the ratio using Kretzer FF is apparently higher than one in the lower p_T, which means the calculation underestimates the yield. The ratio is about 3 at p_T of around 3GeV/c. The ratio becomes close to one as p_T becomes higher than around 8GeV/c. We conclude that the NLO pQCD calculation using the Kretzer FF fails to describe the data.

These different behavior with the three FFs is due to the fragmentation from the gluon jet. Figure 4.10 shows the fraction of gluon and quark jet for the π^0 production as a function of π^0 p_T. The figure is obtained from the NLO pQCD calculation when using the KKP FF and the scale of p_T. In the lower p_T than 8GeV/c where the discrepancy from three FFs are observed, the π^0 production is dominated by the gluon jet. This can be explained by the parton distribution in the proton. In the small x region, the gluon is a dominant parton.

Figure 4.11 [42] shows the fragmentation function from the gluon jet as a function of z from the OPAL collaboration [38] at $\sqrt{s}$ of 161GeV. In the figure,

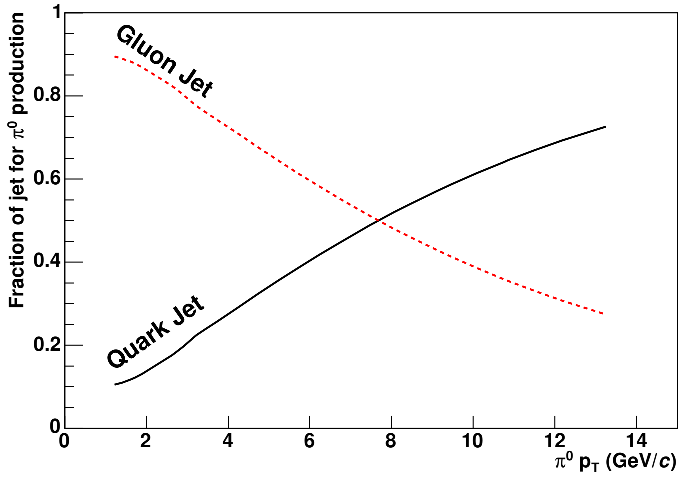

Figure 4.10: *Fraction of gluon (dotted red line) and quark (solid black line) jet for the π^0 production obtained from the NLO pQCD calculation with CTEQ6M [24, 75] PDF and KKP [43] FF at the scale of p_T.*

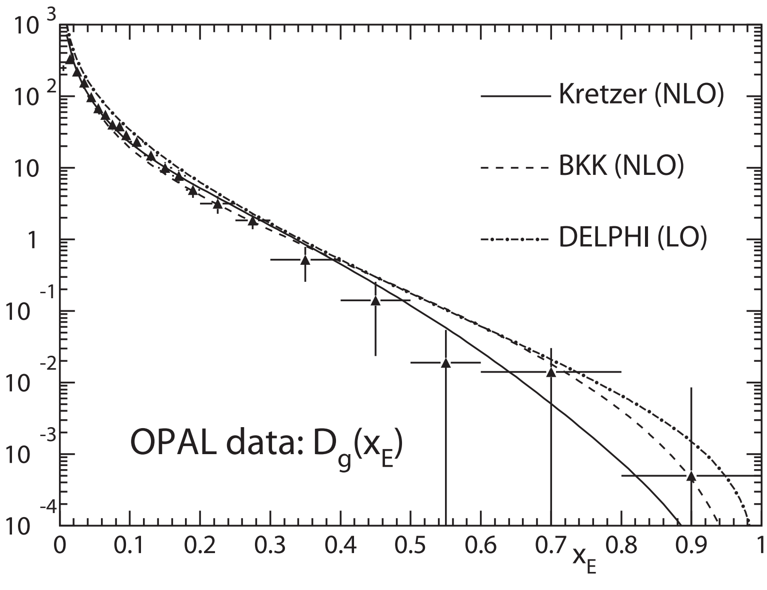

Figure 4.11: *As shown in [42], the gluon fragmentation function (FF) measured by the OPAL collaboration [38] at $\sqrt{s}$ of 161GeV are compared with Kretzer [42], BKK [41], and a leading-order FF from the DELPHI [39] collaboration.*

three different FFs are compared: Kretzer [42], BKK [41], and a leading-order FF from the DELPHI [39] collaboration. As discussed by Kretzer, there remains a large uncertainty on the gluon fragmentation function at the high z region because of the poor statistics on the 3-jet events. The figure shows the Kretzer FF is apparently lower than BKK FF at z>0.5. They differ by a factor of 10 at the maximum.

A natural question is about z range in which we have observed the π^0 production at $\sqrt{s}$ of 200GeV. Because both the fragmentation function and the p_T distribution of jet production are steep, the z distribution, which contributes to π^0 production at low p_T, spreads widely from 0 to 1 and peaks at around 0.5. The contribution from the lower z is suppressed because of the steep p_T distribution of jet In the same analogy, the contribution from the higher z is suppressed because of the steep distribution of the FF. Thus, the deviation between two FFs at the z more than 0.5 affects the π^0 spectrum. The failure of the Kretzer FF can be explained by the gluon fragmentation at the higher z region.

In summary, the uncertainty on the renormalization and factorization scale, which is derived from three scales, is order of $\pm 50\%$ in the NLO pQCD calculation. Within that level, the NLO pQCD calculation using KKP and BKK FF are consistent with the present data. However, the Kretzer FF fails to describe the present data. This discrepancy is due to the large uncertainty on the gluon FF at z larger than 0.5. A conclusion in this section is that the present data, the cross section measurement of the π^0 at $\sqrt{s}$ of 200GeV, provides an ideal reference for the fragmentation function, especially for the gluon fragmentation function.

4.4.2 $\sqrt{s}$ Dependence.

In this section, we examine the $\sqrt{s}$ dependence of the present data together with other data. We discuss the uncertainty on the renormalization and factorization scale in the NLO pQCD calculation.

Figure 4.12 shows a comparison between the present data with only the statistical error and the pQCD calculation using the KKP [43] fragmentation function. The comparison of other data at $\sqrt{s} = 23$GeV by CCRS [48] and WA70 [59], at $\sqrt{s} = 62$GeV by CCRS [48], Eggert *et al.* [49], R806 [53], and R807(AFS) [53], and at $\sqrt{s} = 540$GeV by UA2 [61] are also shown in the same figure. All the data shown in the figure are from resolved π^0 measurement or are corrected for the contamination of the η and the direct-γ. In the pQCD calculation, the scales of 1/3 p_T, 1/2 p_T, and p_T at $\sqrt{s} \approx 23$GeV and the scales of 1/2 p_T, 1 p_T, and 2 p_T at $\sqrt{s} > 23$GeV are used. For most of data at the ISR collider and at fixed target experiments, the measured range of η is assumed to be less than ± 0.01 in the calculation because it's not clearly shown. The figure shows that all the data at $\sqrt{s}$ from 20 to 540GeV are consistent with the pQCD calculation using three selected scales. From the comparison, we conclude the pQCD calculation can describe the present data and all the data at the wide $\sqrt{s}$ range from 20

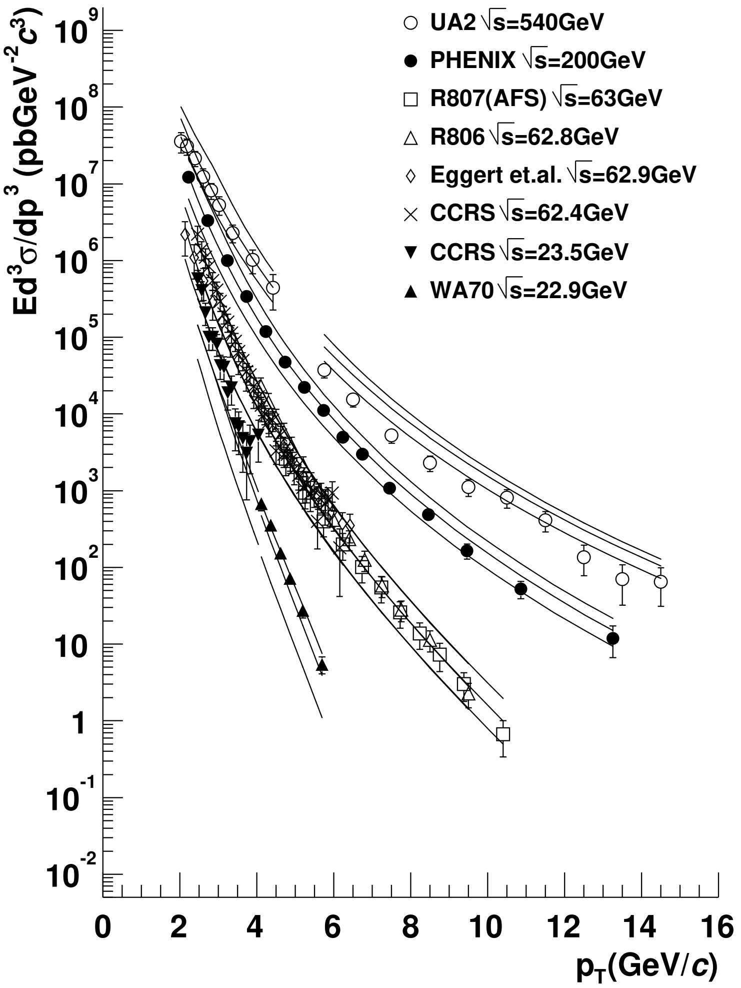

Figure 4.12: *Differential cross section of* π^0 *production at* $\sqrt{s}$ = *23GeV by CCRS [48] and WA70 [59], at* $\sqrt{s}$ = *62GeV by CCRS [48], Eggert et al. [49], R806 [53], and R807(AFS) [53], at* $\sqrt{s}$ = *540GeV by UA2 [61], and the present data labeled as PHENIX. An NLO pQCD calculations with CTEQ6M [24, 75] PDF and KKP [43] FF are shown in three scales of* $1/3p_T$ *(top),* $1/2p_T$ *(middle), and* p_T *(bottom) for* $\sqrt{s} \approx 23\text{GeV}$ *and those of* $1/2p_T$ *(top),* p_T *(middle), and* $2p_T$ *(bottom) for* $\sqrt{s} > 60\text{GeV}$. *Only the statistical errors are shown.*

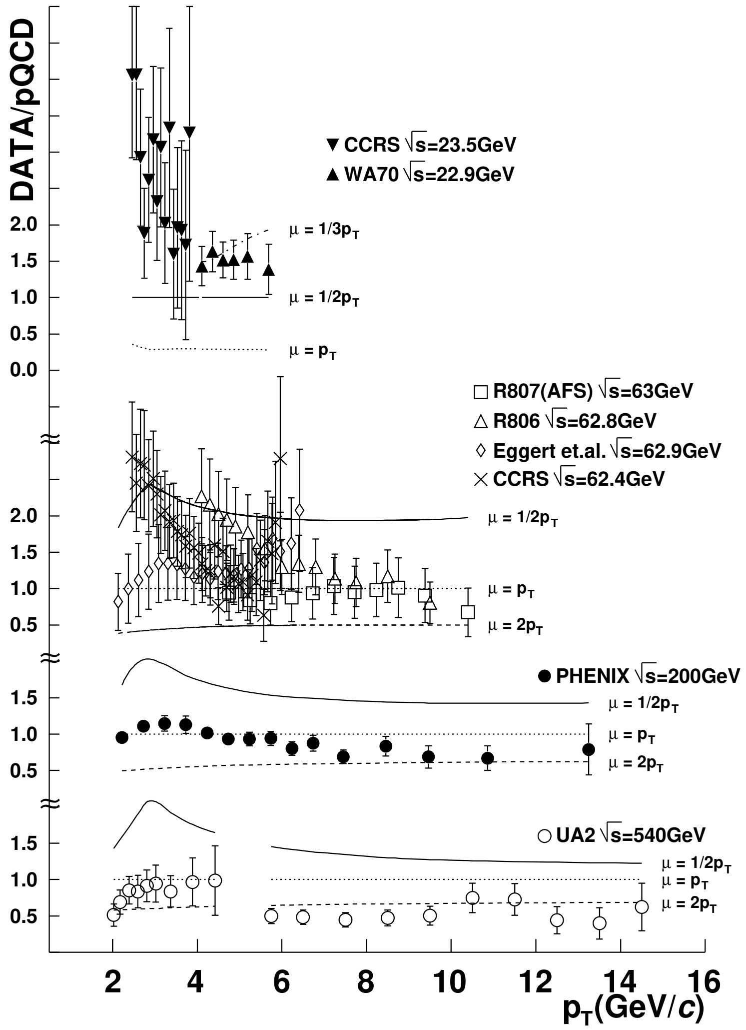

Figure 4.13: *Ratios of the cross section of* π^0 *production at* $\sqrt{s} = 23GeV$ *by CCRS [48] and WA70 [59], at* $\sqrt{s} = 62GeV$ *by CCRS [48], Eggert et al. [49], R806 [53], and R807(AFS) [53], at* $\sqrt{s} = 540GeV$ *by UA2 [61], and the present data to an NLO pQCD calculation obtained with the scale of* $\mu = 1/2p_T$ *for* $\sqrt{s} \approx 23GeV$ *and of* $\mu = p_T$ *for* $\sqrt{s}$ *>20GeV. The ratios of the NLO pQCD calculation with the three scales are shown. The systematic and statistical errors are added quadratically and shown in the ratios.*

to 540GeV. The NLO pQCD calculation covers, for example, over 5th order of magnitude (10pb/GeV^2 to 10^5pb/GeV^2) at p_T of 5GeV/c.

Figure 4.13 shows ratios of the data to the pQCD calculation. The systematic and statistical errors are added quadratically and shown in the ratios. As discussed before, the factorization and renormalization scale may approach the starting scale Q^0 (=1GeV) of the QCD evolution. Especially at the scale of 1/3 p_T, the parton densities are not constrained by data. To avoid this problem, the comparison is performed at larger p_T than 2GeV/c. The ratios of the data to the calculations show that the data can not be explained by calculations using single scale. As discussed before, the present data labeled as PHENIX and the UA2 data are consistent with the calculation using the scale of p_T in the lower p_T and decreases down to the level at the scale of 2 p_T gradually as p_T increases. However, different behavior is observed at the lower $\sqrt{s}$. The data at the lower $\sqrt{s}$ than 63GeV are consistent with the calculation at the scale of $\mu = 1/3p_T$. This fact indicates that selection of scale and its $\sqrt{s}$ dependence on the scale is essential to reproduce the data. In order to describe all the data by an NLO pQCD calculation, the renormalization and factorization scales need to be chosen properly depending on the measured kinematic region. The best scale in which the calculation reproduces the data increases systematically as $\sqrt{s}$ increases. For more thorough comparison, we also compare the data from other experiments with the NLO pQCD calculation as shown in Appendix D. They show consistent behavior as those in Figure 4.13.

In the rest of this section, we discuss the choice of the scales in different $\sqrt{s}$. As discussed in [66], soft gluon radiation is important so it is not easy to verify the principle of minimum sensitivity criterion for the scale selection. This means that the higher order correction is large so that the prediction of the NLO pQCD calculation is quite unstable under changes of the scales. In order to improve the knowledge of the soft gluon radiation, a next-to-next-to-leading-order (NNLO) pQCD calculation are recently performed in direct photon production [124]. For the NNLO calculation in hadron production, the fragmentation function using the NNLO evolution, which is not yet obtained, is necessary

The collinear process, which is the gluon radiation from parton with small transverse momentum, is the main source of the soft gluon. In the pQCD calculation, such soft gluon with smaller transverse momentum than the factorization scale is cut off as discussed in Section 1.1, thus it is related to the uncertainty of the scale. The sophisticated factorization scheme [125] to re-sum the collinear process have been proposed. However, the contribution of the collinear process is sometimes treated as the transverse component of the initial parton's momentum in hadron, which is named as k_T smearing effect. The first observation of the initial k_T smearing effect is reported in the lepton pair measurement for the Drell-Yang process. The lepton pair production shows a wide p_T distribution, whose width is believed to be caused by the initial k_T smearing of the quark and anti-quarks in the hadron. The values of the initial k_T of the quark can be estimated as $1/\sqrt{2}$ of the lepton pair p_T. As well as the lepton pairs, other measurements of muon, pion, and jets pairs in proton-proton or proton-antiproton collisions show a logarithmical increase [126] of the width of the p_T distribution with increasing $\sqrt{s}$. An extrapolation of the initial k_T to $\sqrt{s}$ of 200GeV is $2-3$GeV, which is apparently larger than an expectation (0.3-0.5GeV/c) from the proton size. In the comparison between the direct photon measurement and an NLO pQCD calculation, a classical treatment of the initial k_T smearing has succeeded [127] to describe the direct photon production. In order to study the scale selection, we need to study the effect carefully.

A conclusion in this section is that the NLO pQCD calculation can describe the inclusive π^0 measurement in wider range of $\sqrt{s}$ from 20GeV to 540GeV only when the renormalization and factorization scales are chosen depending on the kinematic region.

4.5 Comparison with Au+Au Collisions

In this section, the π^0 measurement in p+p collisions and in Au+Au collisions are compared. Figure 4.14 shows the π^0 measurement in Au+Au central collisions with less than 10% centrality and in the peripheral collisions from 80% to 92% centrality [90]. The centrality is estimated by the particle production at BBC and ZDC. We define that the 0% centrality means the head-on collisions. The obtained result in this work is divided by the total inelastic cross section of the p+p collisions and multiplied by a number of collisions ($\langle N_{coll}\rangle$) which is the average number of nucleon+nucleon collision in an Au+Au collision estimated by the Glauber model [89]. The model calculation results in that the $\langle N_{coll}\rangle$ is 955.4 ± 93.6 in the central collisions and 4.9 ± 1.2 in the peripheral collisions.

The comparison between the p+p collisions and the peripheral Au+Au collisions shows a good agreement within the systematic error of $\langle N_{coll}\rangle$, which is shown as bands in the figure. The systematic error of $\langle N_{coll}\rangle$ in the peripheral collisions, which is $\pm$ 25%, is originated from the validity of the Glauber model and from imperfect knowledge of the Au+Au collisions. The uncertainty is mainly on the particle production from collisions in the forward region where the BBC and ZDC are sitting and the density distribution especially in the skin of the Au nucleus. The agreement in the peripheral collisions within the bands represents that the validity of the Glauber model and that the peripheral collisions can be described as an incoherent superposition of nucleon+nucleon collisions.

In the central collisions, the Au+Au result shows a large deviation and notably below the scaled p+p collisions even with the systematic error on $\langle N_{coll}\rangle$ of $\pm$ 10%. The ratio of the Au+Au central collisions to the present result is around 20-30%, which depends on the measured p_T. This suppression in the Au+Au collision is consistent with the theoretical model, jet quenching, which is predicted as a QGP signature [80].

In summary, the result in the Au+Au peripheral collisions is consistent with the present result in the p+p collisions scaled with the $\langle N_{coll} \rangle$. This consistency indicates that the Glauber model is valid in our kinematic region. A significant suppression of the π^0 production in the Au+Au central collisions compared to the present result scaled with the $\langle N_{coll} \rangle$ has been discovered. This suppression indicates that the π^0 production in the Au+Au central collisions can not be explained by an incoherent superposition of the nucleon+nucleon collisions, but can be explained by a model, in which the QGP is created in the collisions. We conclude that the present result provides a crucial data for the QGP search.

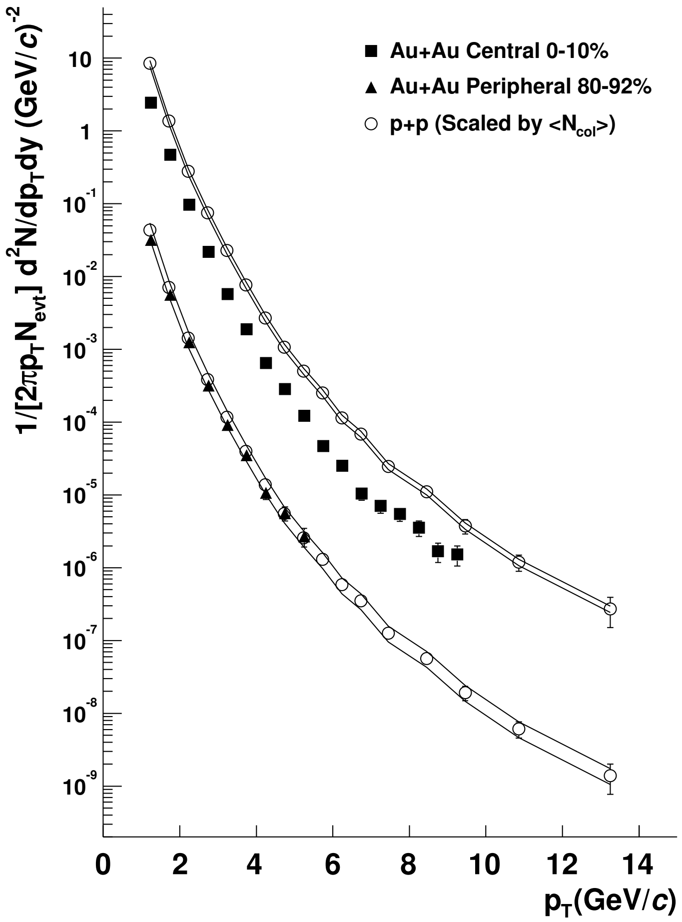

Figure 4.14: π^0 *yields per event as a function of* p_T *for* $60-80\%$(*lower*) *and* $0-10\%$(*upper*) *centrality event samples with references of the* π^0 *yield per collision in N+N collisions multiplied by the averaged number of collisions* ($< N_{coll} >$) *estimated by the Glauber model [89].*

Chapter 5

Conclusion

We report the cross section of the neutral pion (π^0) production from the proton-proton collisions at $\sqrt{s}$ of 200GeV at the PHENIX experiment. We have measured the cross section at p_T from 1.22GeV/c to 13.25GeV/c in the pseudo-rapidity coverage of -0.35 to 0.35. This is the neutral pion measurement at the highest energy in the world as the proton-proton collisions. During 2001–2002, the Relativistic Heavy Ion Collider (RHIC) was successfully operated as the first polarized proton collider. The data were collected using the minimum bias trigger and newly installed high-p_T trigger. The high-p_T trigger is essential in enhancing the sample of neutral pions at high p_T by a factor of about 50. The analyzed data consists of 16M events of the minimum bias trigger and 18M events of the high-p_T trigger, which are equivalent to the beam luminosity of 39nb^{-1}.

Two photons from π^0 are detected by the PHENIX electro-magnetic calorimeter. The uncertainty of the energy scale is the largest source of the systematic error on the π^0 measurement. The total systematic error is 7% to 15% depending on the measured p_T. The normalization error, which is the error on the luminosity, is 9.6%. In p_T higher than 8GeV/c, the statistical error is larger than the systematic error. The statistical error at the highest p_T is about 40%.

The obtained cross section is compared with other measurement from $p+p$ and $p+\bar{p}$ collisions in wide range of $\sqrt{s}$ from 20 to 540GeV. The present result together with other results are examined for the x_T scaling property in the form of $\sqrt{s}^n \times E\frac{d^3\sigma}{dp^3}$. The results can be described by a single function of x_T when using $n = 6.3$, which is consistent with the R108 collaboration [51]. This scaling property over the wide $\sqrt{s}$ range from 60GeV to 540GeV indicates the point-like interaction in the collisions. The constituent interchange model (CIM), which predicts $n = 8$, is apparently ruled out.

In this work, we have a motivation to provide a testing ground of perturbative Quantum ChromoDynamics (pQCD). The present data are compared with a next-to-leading-order (NLO) pQCD calculation with the CTEQ6M [24, 75] parton distribution function (PDF). In the NLO pQCD calculation. the uncertainty on the renormalization and factorization scale, which is derived from three scales, is order of $\pm 50\%$. Within that level, the NLO pQCD calculation using the KKP [43] and the BKK [41] fragmentation function (FF) are consistent with the present data. However, the calculation using the Kretzer [42] FF fails to describe the present data. This discrepancy is due to the large uncertainty on the gluon FF at z larger than 0.5. We conclude that the present data provides an ideal reference for the determination of the fragmentation function, especially from the gluon jet.

The present data together with other data in various $\sqrt{s}$ can be described well by the NLO pQCD calculation only when the proper scales are chosen for the measured kinematic region. At $\sqrt{s}$ of $20 - 540$GeV, the best scale in which the calculation reproduces the data increases systematically as $\sqrt{s}$ increases. We conclude that the best scale is $\mu = p_T$ at $\sqrt{s}$ of 200GeV.

The present result is compared with the π^0 production in the Au+Au collisions at $\sqrt{s}$ of 200GeV. After multiplying an averaged number of collisions calculated by the Glauber model, the present result is consistent with the result in the peripheral Au+Au collisions. This fact is a proof of that the averaged number of collisions calculated by the Glauber model is correct. In the comparison with the central Au+Au collisions, a notable decrease of the π^0 yield in the central collisions is observed, which is consistent with the jet quenching scenario as a QGP signal. We conclude that the present result provides a crucial data for the QGP search.

Acknowledgement

I would like to thank Prof. Ken'ichi Imai as the group leader of the experimental nuclear and hadron physics group at Kyoto Univ. His suggestion for me to go in the MuID construction group and the EMCal test experiment at CERN was the trigger for my participating in the PHENIX collaboration. Without his sincere support, I couldn't finish this work.

I feel very good in performing this work with the PHENIX collaboration. I am deeply grateful to the spokesperson, Prof. Will A Zajc for his heartful administration of entire collaboration. He also supported my participating and performing the EMCal test experiment at CERN.

The financial support from RIKEN and PHENIX-J was essential to continue the work. I would like to thank the former chief scientist of the radiation laboratory at RIKEN, Dr. Masayasu Ishihara and current chief scientist, Dr. Hideto En'yo for their support. I would express my special thanks to Hideto for the useful discussion about the analysis. The deputy group reader of the RIKEN BNL Research Center, Dr. Gerry Bounce, has always encouraged my continuing the research at BNL. I'd like to express many thanks to the PHENIX-j group leader, Prof. Hideki Hamagaki for the continuous financial support.

Prof. Naohito Saito and Dr. Yuji Goto have proposed the EMCal test experiment and kindly supported my analysis of the test experiment. Their strong intention for the entertainment including food, drink, music, and movie allow me to spend great time at BNL. I have to mention that their endless pressure for my writing thesis and many comments on the thesis draft have encouraged me. I'd like to express my sincere thanks to them.

I thank the PHENIX EMCal group, T. C. Awes, G. David, E. Kistenev, P. Stankus, M.J. Tannenbaum, S. N. White, and C.L. Woody. I express my special thanks to Edouard for his teaching about the detector. His unique and gentle discussion has encouraged me always. I thank my friends, S. Bathe and H. Buesching for the useful discussion about the detector. I also thank X. Camard and C. Klein-Boesing for the collaboration to perform the FEM quality check. For constructing the ERT trigger, I appreciate all helps and discussions with the ERT group, C. Aidara, F. Bauer, M. Harvey, B. K. Nandi, K. Okada, M. Grosse Perdekamp, and W. Xie. The collaboration with RICH group, F. Kajihara, S. Kametani, T. Matsumoto, K. Oyama, and K. Ozawa, are very helpful for the implementing the ERT trigger. I'd like to express many thanks to them.

I'd like to thank the π_0 analysis group, S. Bazilevsky, S. Belikov, B. D Fox, K. Reyger, and M. Volkov. I want to express my special thanks to Sasha for his help to obtain several figures and the Monte Carlo simulation in my thesis. To be honest, the analysis would not be completed without his excellent idea about the trigger bias. I've been encouraged by Brendan for his heartful administration of entire the group. I also thank the Au+Au analysis group.

The computing center at Japan (CCJ) were used for the data analysis and the NLO pQCD calculation. I'd like to express many thanks to the CCJ group for their endless maintenance of the computers. I also thank RCF group for their 24-hour support. The member of the RIKEN group are very gentle and helpful not only for my physics interest but also my spending good time at BNL. I'd like to express many thanks to them.

I appreciate all heartful support by the secretaries, T. A. Heinz, H. Horie, T. Ito, N. Kiyama, and C. Shimoyamada for their support of the research. The sharing the house at BNL with many people from Japanese institutes have enabled me to spend a joyful time. The amazing entertainment with them at BNL and Manhattan have sometimes relaxed me. I am grateful to all my colleagues and friends.

I'd like to express my great thanks to my father and mother, Kazuyuki and Hisae, for their support of my continuing this work. I couldn't continue and finish this work without my wife and her support. I'd like to dedicate this thesis to my wife, Mina.

Appendix A

Beam Test for EMCal Performance

The calorimeter's energy resolution, linearity and hadron rejection had already been measured at BNL-AGS in the energy range up to 7GeV [103]. In order to extend these measurements to the energy range up to 80GeV, a beam test [104] was performed at the CERN-SPS H6 beam line in 1998. In this section, we explain the setup of the test beam and the analysis for the PbSc.

The purpose of the test is to investigate the performance of the calorimeter in the energy range up to 80GeV and, in particular, the linearity of response versus beam energy. Since our goal in PHENIX is to measure prompt photon and π^0 production cross sections with the calorimeter within 10% errors, it is important to understand the linearity of the calorimeter at the level of 2%.

A.1 Setup

Figure A.1 shows setup of the beam test. One PbSc super-module and four PbGl super-modules were located at the H6 beam line and were tested with electron beams in the momentum range of 10GeV/c to 80GeV/c and π^+ beams of 40GeV/c. They were placed on a movable platform to change the position and angle of the incident beam. A delay-line wire chambers (DWC) [128] was located just in front of the calorimeter to measure the beam incident position. The position dependence of the energy deposit were measured and corrected using the DWC. Two scintillators, S1 and S2 were used as trigger counters and two other scintillators (muon counters) were set behind iron blocks to identify muons in the beam. There was a Čerenkov Differential counter with Achromatic Ring focus (CEDAR) further upstream of the S1 for electron identification.

We used the 10GeV/c muon beams for tower-by-tower gain adjustment of the towers in addition to the electron beams. For time-dependent gain drift correction of the PbSc calorimeter, we used a laser monitoring system [102].

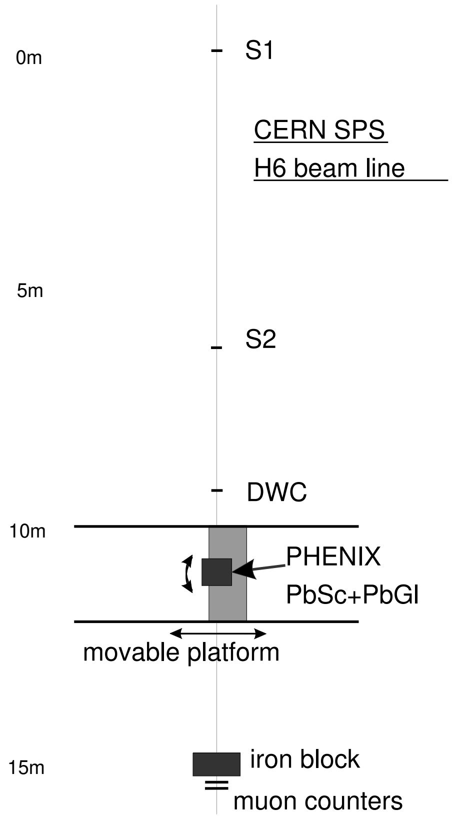

Figure A.1: *Setup of the beam test at CERN.*

The DWC has good position resolution of 0.2mm and high detection capability of 2×10^5 particles/sec. It consists of one anode-wire plane and two cathode wire planes The cathode planes have 2mm wire spacing. Their wires are connected with a delay-line through which signals are read out by TDC modules. The timing information corresponds linearly to position information. The active area is 100×100 mm^2.

A beam trigger was composed of the S1("$S1$"), the S2 ("$S2$") and two muon counters ("μ"). An electron trigger was made by $S1\otimes S2\otimes\bar{\mu}$ and a muon trigger was made by $S1\otimes S2\otimes\mu$. Other Triggers for pedestal measurement and for the laser monitoring system were used between beam spills.

We used two different HV settings:

- normal HV setting (1.23–1.29kV) for energy measurements up to 80GeV and
- low HV setting (1.13–1.19kV) for energy measurements up to 160GeV.

To read-out the PMT signals from the calorimeter, we used front-end electronics from the CERN experiment WA98[129].

A.2 Analysis

The deposited energy in each tower is calculated by multiplying the ADC count by a calibration factor, $C(t)$ (GeV/count). The calibration factor has time dependence. We parameterize the time dependence by an initial gain factor, G (GeV/count), and a gain drift, $D(t)$; $C(t) = G \times D(t)$. The time dependent factor, $D(t)$, is defined to be 1 at the time of the muon calibration run.

The ADC count is derived from low and high gain ADCs which are designed to cover the wide dynamic range. We examine the ratio of the high gain to the low gain for each event. We find 1% difference between the ratio in electron events and in laser events. We obtained the ratio in electron events for the 40 towers which have hits in the electron beam data. For the other towers, we measure the ratio with the laser trigger events. These towers have only a small contribution to the electron energy measurement, hence have small effect on the energy measurement. The average value of the ratio is 7.8. The ADC value is derived from the low gain ADC when the low gain ADC is larger than 90 counts. We also confirm no time dependence of the ratio during whole run. The systematic error caused by the ratio is less than 1%.

The gain for each tower is adjusted by using muons. In order to identify muons, the following selections are applied:

1. The tower which has the largest energy deposit in all towers must have more than 80% of the energy sum of all towers.

2. The number of towers which have energy deposit more than 130MeV must be zero or one.

When a muon beam penetrates one tower longitudinally, the most probable energy deposit is about 300MeV. The first selection requires that there are some hits which make a peak on that tower. The second selection requires the peak is caused by a minimum-ionizing single particle and rejects background from electrons and multi-hits.

After the muon selection, we have more than 100 muons in each of the 40 towers. We adjust gains of these 40 towers so that the MIP peak position is at the same energy. The peak position is determined to a precision of 2–3%. In order to improve the precision and to obtain the gain factor for the other towers, we use electrons. The remaining errors of tower-by-tower adjustment is 3% in total. These errors are statistical ones. The systematic errors are smaller than these. The absolute value of the gain factor is obtained at the electron beam energy of 20GeV. The average value of the gain factor is 110 (count/GeV).

The time dependence of the gain is obtained using laser calibration system. The time variation of the laser amplitude is less than 3% reflecting the stability of the laser output. To monitor the fluctuation of the laser output, we use a truncated mean of the laser amplitude from 144 towers. The obtained gain drift works reliably over periods of order a few hours. The gain drift between several sets of run period is normalized by using the beam energy of 20GeV in each run period. The accuracy of the beam energy is 1% at 15GeV[130].

In this analysis, the total deposited energy is defined as a sum of energies in the 5×5 towers centered on the tower with the maximum energy deposit. The total energy is corrected by a position dependent factor. The upper-left figure of Fig.A.2 shows the position dependence of the energy sum in 5×5 towers for the 20GeV electron beam. In this figure, the coordinate (X, Y) shows position in one tower obtained by the DWC. The position $(0, 0)$ presents the center of the tower and $(1, 1)$ presents the edge of the tower. The position dependence is fitted as shown in the upper-right figure of Fig.A.2 by the following formula:

$$1 + a \times (X^2 + Y^2) + b \times (X^4 + Y^4) + c \times X^2 \cdot Y^2 \ . \tag{A.1}$$

We obtain the best fit with the following parameters:

$$\begin{aligned} a &= -0.3079 \\ b &= +0.3643 \\ c &= -0.02894 \ . \end{aligned}$$

We use these parameters to correct for the position dependence. The lower-left figure shows the deviation of the energy sum from the hit position dependence and the lower-right figure shows a projection of the deviation. The deviation is 0.5% of the energy sum. The systematic error remaining after the position dependence correction is evaluated to be 0.5%.

A.3 Restults

We measure the energy resolution, linearity and position resolution of the PHENIX EMCal in the test beam at CERN as discussed in Section 2.4.2. For the PbSc, we obtained energy resolution of

$$\begin{aligned} \sigma_E/E &= 1.2\% + \frac{6.2\%}{\sqrt{E(GeV)}} \\ &= 2.1\% \oplus \frac{8.1\%}{\sqrt{E(GeV)}} \ , \end{aligned}$$

and position resolution of

$$\sigma_x(\mathrm{mm}) = 1.4(\mathrm{mm}) + \frac{5.9(\mathrm{mm})}{\sqrt{E(\mathrm{GeV})}} \ .$$

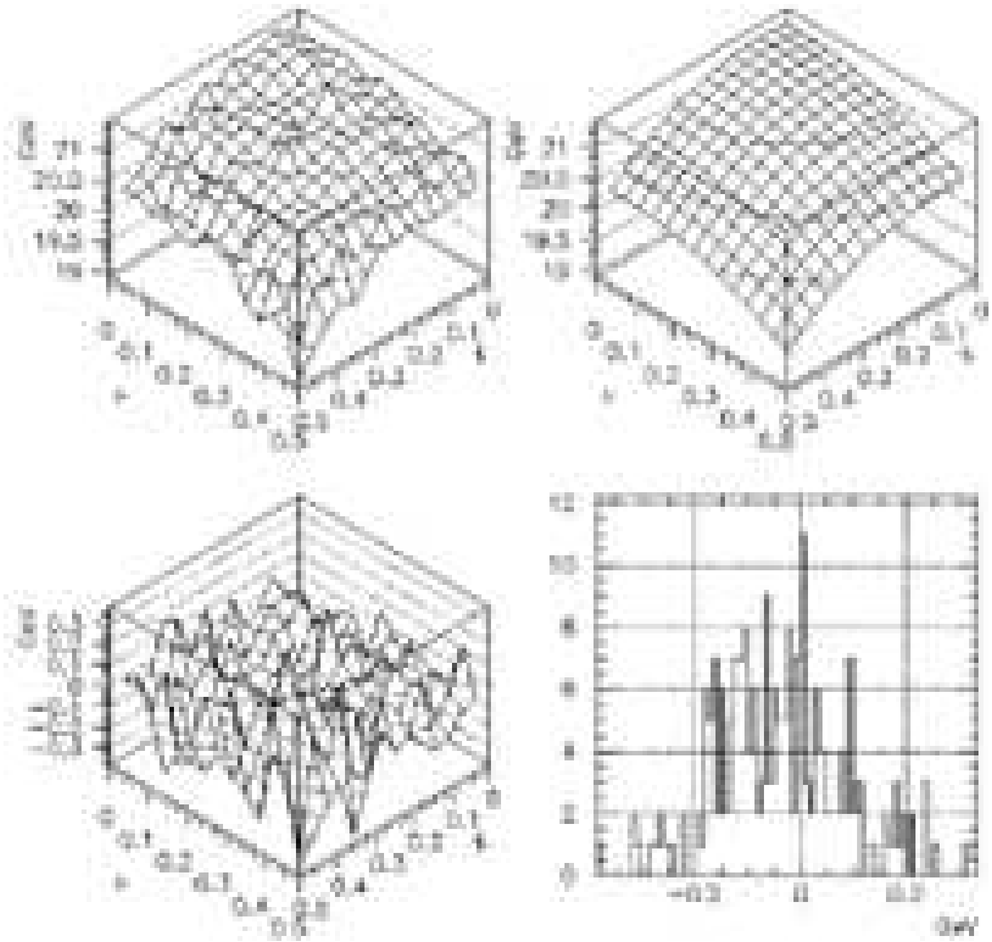

Figure A.2: *(Upper-left) Position dependence of the* 5×5 *energy sum for the 20GeV electron beam, where* (X, Y) *shows a hit position obtained by the DWC. (Upper-right) Fitted hit position dependence. (Lower-left) Deviation of the energy sum from the fitted position dependence (Lower-right) Projection of the deviation.*

We obtain the energy linearity with the systematic error of ≈2%, which meets our requirement.

Appendix B

Discussion of Energy Resolution

The constant term of the energy resolution obtained by analyzing the E/p width in the electron sample is 4.7% as described in Formulae 3.2. The observed p_T of the electron sample is up to 3 GeV/c. The energy resolution obtained by E/p width is consistent with that determined by the π^0 width in the lower p_T where the uncertainty of the other source like the position resolution is negligible. It means that two independent measurements of the energy resolution are consistent in the lower p_T region. The measured constant term of 4.7% is worse than the expectation of 3.0% as described in Section 2.4.3. In this subsection, we discuss the possible source of the worsened resolution.

Gain Drift Figure B.1 shows the MIP energy as a function of the run number in the six PbSc sectors.[1] In all sectors, the run dependence of the MIP looks pretty flat. Figure B.2 shows the projection on the y-axis of Figure B.1. The gain drift of the each sector is smaller than 1% based on fitting the distributions in Figure B.2 with a gaussian.

MIP Higher Order Correction When we calibrate the energy tower-by-tower, the MIP energy of a cluster is used to calibrate the central tower. The central tower is defined in the way that the measured energy of the central tower is largest in all the towers in the cluster. If a charged particle penetrates the EMCal with a maximum angle of 20° in the PHENIX configuration, two or three towers would be activated and clustered. On average, 60% of the total energy in the cluster is detected in the central tower. For the completeness, the MIP correction should be applied in an iterative fashion. However, we only do it once and apply this result to the data. So, the higher-order components of the correction remains uncorrected.

[1]The figures are not obtained from the final version. The only difference from the final version is that the absolute energy calibration (a factor of -2.5% on average) is not applied, so the observed gain drift is still valid.

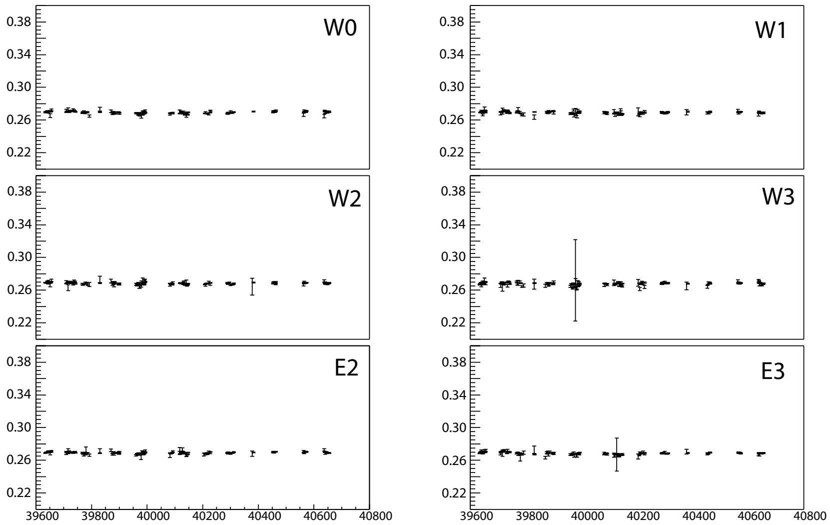

Figure B.1: *Energy of the MIP peak as a function of run number for the six PbSc sectors. The data aren't from the final version of correction which differ only by an overall energy scale correction of -2.5% on average.*

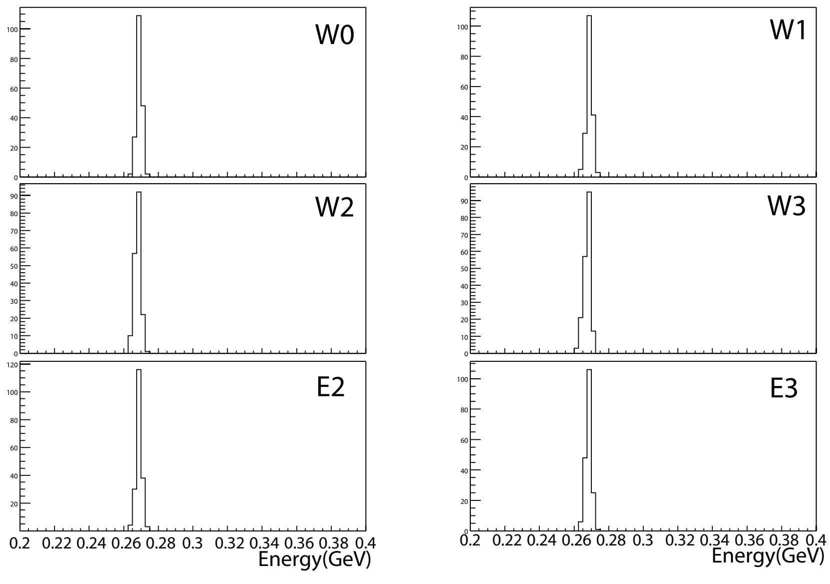

Figure B.2: *Distribution of the run dependence of the MIP energy in the six PbSc sectors. The data are not determined from the final version of correction which differ only by an overall energy scale correction of -2.5% on average.*

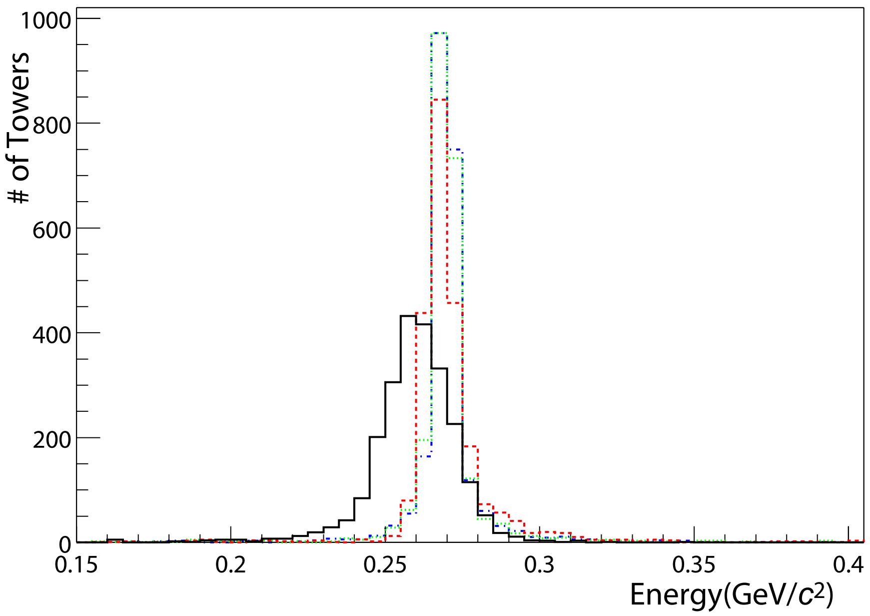

Figure B.3: *Distribution of MIP energy for the 2592 towers in the W0 sector for each higher order of the MIP correction. The initial distribution obtained from the data is the black solid line. The distributions after the second, third, and fourth order corrections are shown in red dashed line, green dotted line, and blue dash-dotted line, respectively.*

Figure B.3 shows the distribution of the tower's MIP energy after applying the higher order components from the 1st to the 4th in the W0 sector. The figure shows that the MIP distribution becomes narrower as higher order corrections are applied. The width after applying the 4th order correction is 1%. In this analysis, the 1st order correction has been applied. The width of the 2nd order correction, which reflects the remaining imperfection in the calibration, is 3%.

For 2% of the towers in addition to the dead towers as discussed in Section 3.3.1, it is not possible to fit the MIP distributions with a gaussian as needed to obtain the position of the MIP peak. We conclude that these 2% is the error on the procedure to determine the dead map. Thus, these matter is incorporated into a systematic error as described in Section 3.5.

Angle Dependence When determining and applying the MIP calibration to the data, it is assumed that the position dependence of the MIP peak arise only from the variation in the incident angle as shown in Formulae 3.1. This assumption is not strictly correct because of: (1) differences in the background shape coming from hadronic shower as mentioned in Section 3.3.2, and (2) the energy threshold (10 MeV) in the clustering algorithm. To estimate the uncertainty arising from them, the single particle GEANT simulation for charged pions is performed.

Figure B.4 (A) shows the distribution of the measured energy (E_{clus} in Formulae 3.1) for charged pions incident on the calorimeter at several different angles. As extracted from these plots, Figure B.4 (B) shows the angle dependence of the position of the peak. In this figure, the black solid line shows the expected trend if the above assumption is true, and the red dotted line shows a fit of the points to a product of the expected trend and a first order of polynomial. The χ^2 of the fit is quite reasonable, so we conclude that the deviation from the assumption is 1% at the maximum.

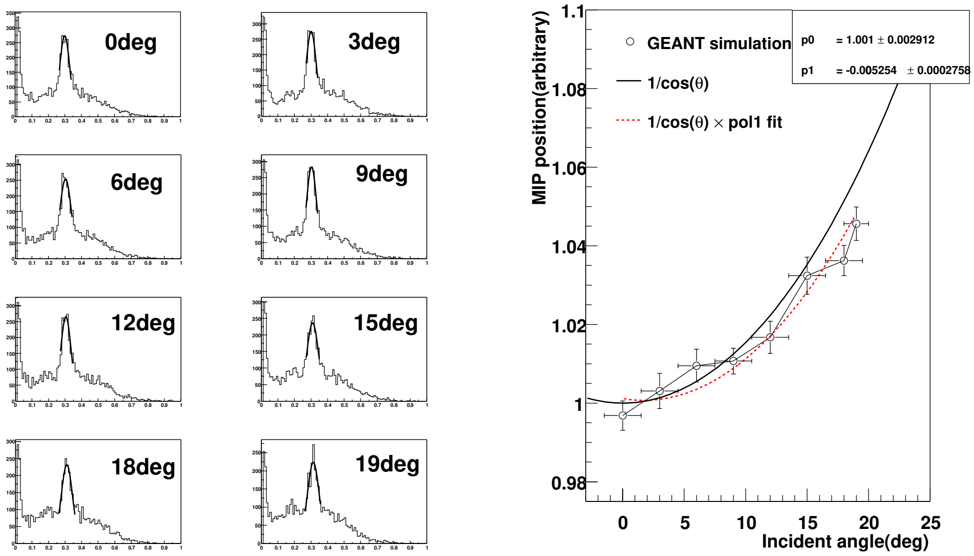

(A) (B)

Figure B.4: *(A)Energy distribution by charged π in the single particle GEANT simulation for different angles of incident where 0° is defined as the orthogonal to the face of the calorimeter. In each plot, the peak position of the MIPs has been fit with a gaussian. (B)Angular dependence of the position of the MIP peak relative to the position for normal incident The black solid line shows the expectation for the case where the measured energy depends on the incident angle only as a result of the variation in the path length through the calorimeter. The red dotted line shows a fit to the product of a first order of polynomial function and the expectation for the above assumption.*

Summary of All Effects From these four studies, we conclude that the various contributions to the energy resolution are:

- gain drift 1%,
- MIP higher-order correction 3%,
- angle dependence 1%, and
- intrinsic resolution 3%.

When summed in quadrature, these contributions result in a 4.5% energy resolution which is consistent with the observed value of 4.7% for E/p in the electron sample as noted in Formulae 3.2. In addition, the position and angle dependence of the measured energy increases the energy resolution. However, the contribution is negligible in comparison with 4.7% when averaging the all position and angle.

Appendix C

Contribution of Hadron Decay

A source for albedo is decays of other hadrons produced in the collision to π^0's. As discussed in Section 3.8, the contribution is not corrected in the data. In this appendix, the detail of the estimate is shown.

To estimate these contributions, the GEANT [109] simulation with an initial sample obtained from the PYTHIA [112] simulation. The PYTHIA v5.720/JETSET v.7.408 is used to generate the event sample. The detail settings are same as described in Section 3.8.1. From the GEANT simulation, the ratio of the selected π^0's and all π^0's is determined to isolate π^0's from hadron decays using the criteria of (1) the particle is photon, (2) the parent of the photon is a π^0, and (3) the grandparent of the photon, i.e. the parent of the π^0 is either a K_0^s or an η. The both invariant mass spectrum of selected and all π^0 are fitted as described in Section 3.4 to extract the raw π^0 yields. The ratios of the selected π^0 and all π^0 represent the contribution of decays from η and K_0^s. The ratios result in 1–3% for K_{0s} and 2–4% for η at p_T between 0.7 and 1.4GeV/c. In both cases, the effects are small.

As a precaution, we examine world data to verify that the results from the PYTHIA are reasonable. Figure C.1 shows the existing measurements of K_0^s [131] and $(h^+ + h^-)/2$ [132] cross sections from the UA1 experiment at $\sqrt{s}$=630 GeV. The data in this figure are fit to the following power-law formula [114]:

$$E \cdot d^3\sigma/dp^3 \quad = \quad A \cdot (p_t^0)^n/(p_T + p_T^0)^n \ .$$

The charged average cross section ($\sigma_{(h^+ + h^-)}$) is scaled by 1/1.6 to estimate the $\sigma_{(\pi^+ + \pi^-)/2}$ cross sections. Figure C.2 (A) shows a comparison of the ratios between $\sigma_{K_0^s}$ and either σ_{π^0} or $\sigma_{(\pi^+ + \pi^-)/2}$ cross sections obtained from the PYTHIA, measured by UA1, and measured by UA5 [133] at $\sqrt{s}=540$ GeV. Both the measurements and the PYTHIA prediction are consistent and show a strong p_T dependence. The PYTHIA prediction shows its maximum of 0.35 at p_T of 3 GeV/c followed by a steady decrease in the higher p_T.

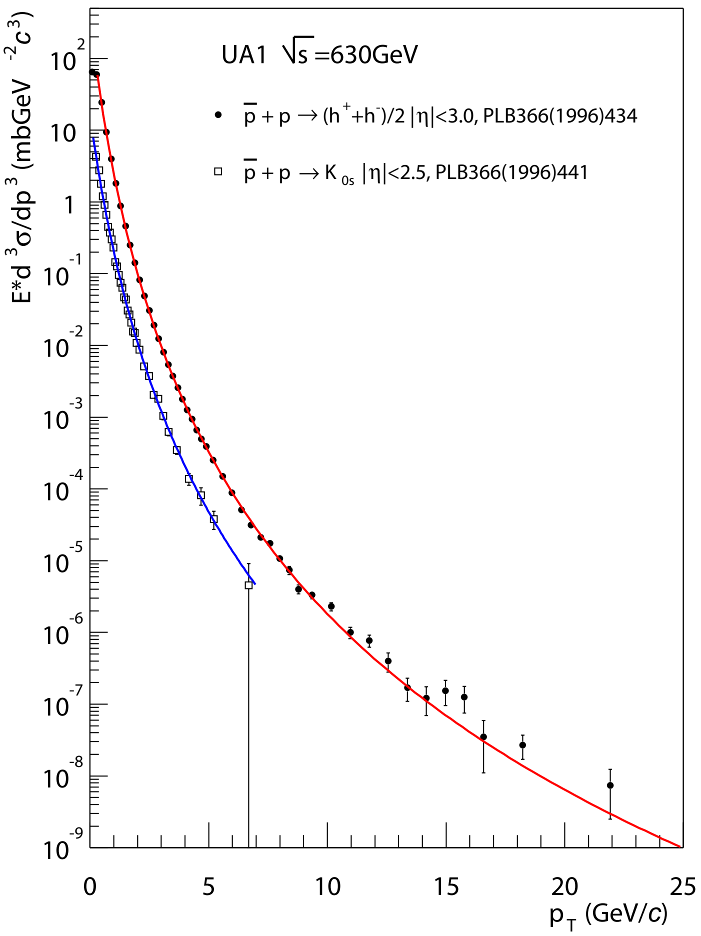

Figure C.1: *Invariant cross section of charged hadron production (closed circle) [132] and K_s^0 production (open square) [131] from the UA1 collaboration at $\sqrt{s}$ of 630GeV with fitting results.*

Figure C.2 (B) shows the ratio of σ_η to σ_{π^0} at $\sqrt{s} = 63$ GeV [134]. Both the measurement and the PYTHIA prediction are consistent. This ratio looks flat 0.45 in the p_T region of more than 2 GeV/c.

We don't investigate the $\sqrt{s}$ dependence of the η/π^0 and K_0^s/π^0. Both the ratios for both η and the K_0^s in the PYTHIA simulation are consistent with the measurements in the measured range of p_T. For further consistency check, the kinematic acceptance of π^0 from the decay of η and K_0^s are shown in Figure C.3 as the measured ratio of π^0 from the decay and all π^0. The estimated contribution is 3-6% in our p_T range which, within the statistical error, is consistent with the GEANT simulation with an initial sample from the PYTHIA in the measured range of p_T.

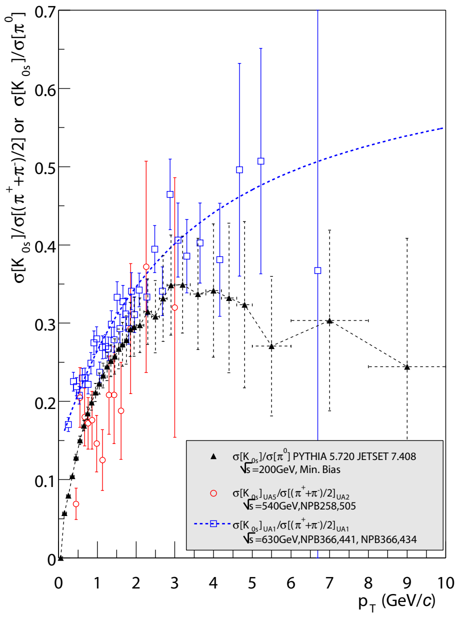

(A)

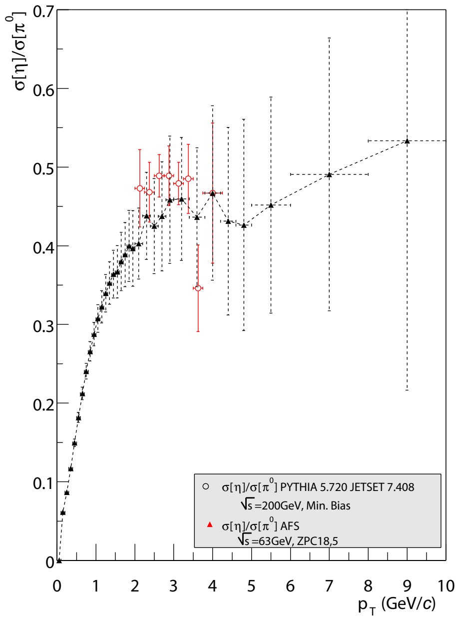

(B)

Figure C.2: *(A)Comparison of the ratio of K_{0s} to $(\pi^+ + \pi^-)/2$ and π^0 from available data from UA5 [133] and UA1 [131] as shown in Figure C.1 with the results from the PYTHIA simulation. (B)Comparison of the ratio of η to $(\pi^+ + \pi^-)/2$ and π^0 from available data by AFS [134] with the results from the PYTHIA simulation.*

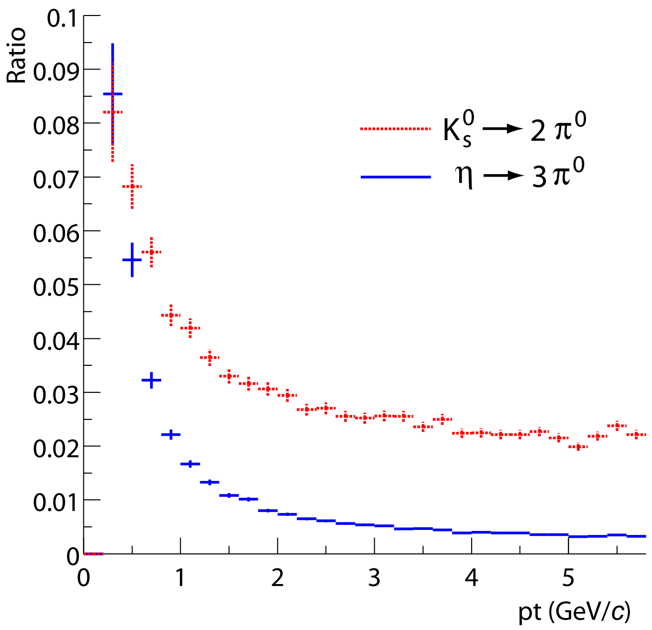

Figure C.3: *Ratio of π^0 from η and K_s decay obtained by the FastMC to the initial π^0. The ratio of the initial η/π^0 and K^s/π^0 is taken from the PYTHIA simulation of p+p collisions at $\sqrt{s}$ of 200GeV. The sum of both at p_T of more than 1GeV/c is less than 6%.*

Appendix D

Compilation of Other Results

In this chapter, we explain how to obtain the weighted mean p_T of the result from the E706 collaboration. Then the inclusive differential cross section of π^0 are shown for their different $\sqrt{s}$ from 20GeV to 540GeV from other experiments as discussed in Section 4.2.

Weighted Mean p_T The π^0 measurement from the E706 collaboration is shown in their paper [64] with their p_T bin, *i.e.*, the minimum and maximum value of p_T bin. To compare the measurement of π^0 production by E706 and an NLO pQCD calculation, and to deal with them with the other results in a same way, it is convenient to obtain the weighted mean p_T for each p_T bin. In this section, the way to obtain the weighted mean p_T is described.

Figure D.1 shows the results of the π^0 measurement by E706 at the beam momentum of 530GeV and 800GeV The power-law formula, $f(p_T) = c(1 + p_T/p_0)^{-n}$ [114] is used to fit them and the results are also shown in the figure. the weighted mean ($[p_T]$) for the p_T bin ((p_{T1}, p_{T2}) is defined as

$$[p_T] \equiv \int_{p_{T1}}^{p_{T2}} (p_T \times F(p_T))dp_T / \int_{p_{T1}}^{p_{T2}} F(p_T)dp_T \ ,$$

where $F(p_T) = p_T \cdot f(p_T)$.

these fitting and the calculation of the weighted mean p_T need to be done in an iterative way. In this work, the procedure is done only once and the weighted mean p_T is obtained.

Comparison of Other Results Figure D.2 shows the $\sqrt{s}$ dependence of the differential cross section from 20GeV to 540GeV. Only the statistical errors are shown in the figures. The data by E706 at $\sqrt{s}$ = 31.5GeV and by CCR at $\sqrt{s}$ = 62.4GeV show larger values than others systematically. All the data are sitting within several order magnitude difference for each other, which difference can be easily explained by their systematic error. The obtained result in this work

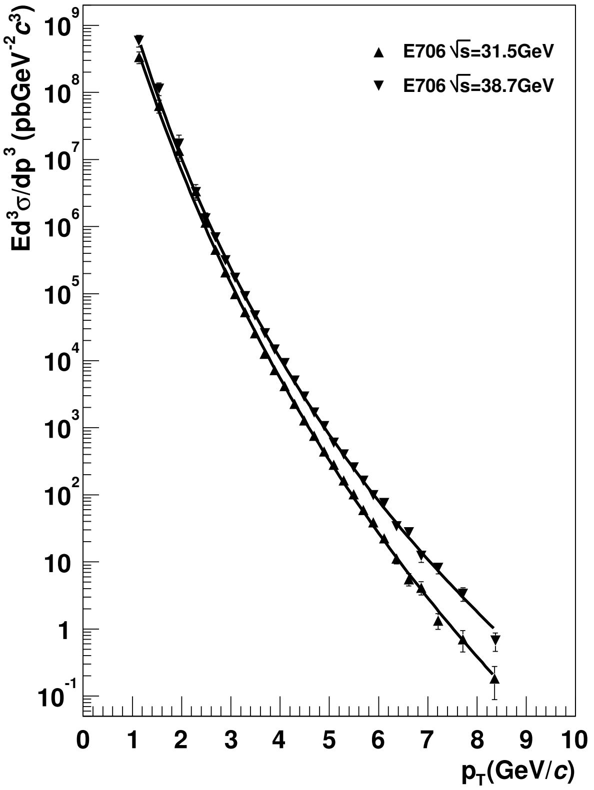

Figure D.1: *Differential cross section of the* π^0 *by the E706 collaboration [64] at the beam momentum of 530GeV* ($\sqrt{s} = 31.5\text{GeV}$) *(up triangle) and 800GeV* ($\sqrt{s} = 38.7\text{GeV}$) *(down triangle) with the results of a fitting by the power-law formula,* $f(p_T) = c(1 + p_T/p_0)^{-n}$.

is labeled as PHENIX. We summarize the all the experiments and the reference in Table D.1.

Comparison with an NLO pQCD Calculation Figure D.3, Figure D.4, and Figure D.5 show ratios of all the results ,which covers the wide $\sqrt{s}$ range from 20GeV to 540GeV, to the pQCD calculation with the scale of $\mu = 1/2p_T$. The systematic and statistical errors are added quadratically and shown in the ratios.

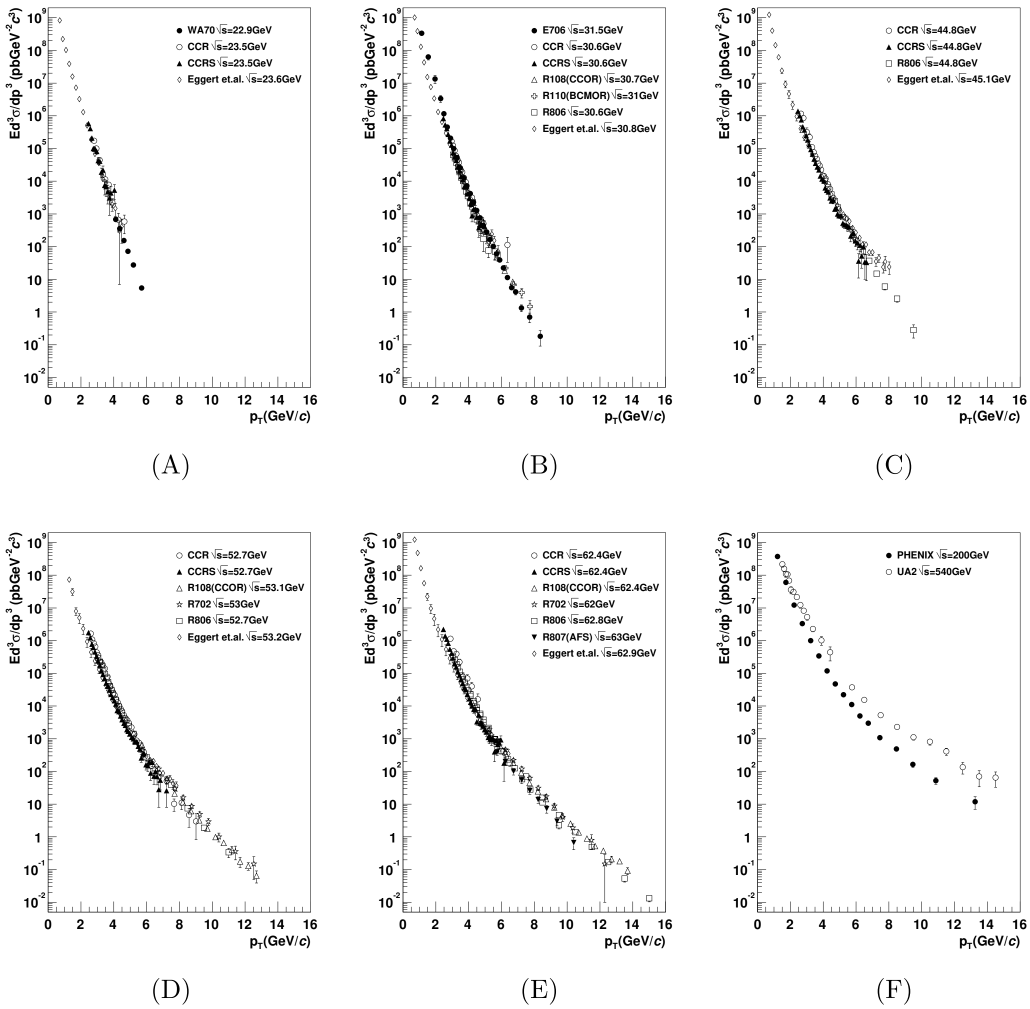

Figure D.2: *Compilation of the inclusive π^0 production at $\sqrt{s}$ of around (A)20GeV and (B)≈ 30GeV. (A)≈ 40GeV, (B)≈ 50GeV, (C)≈ 60GeV, and (D)more than 100GeV. Only the statistical errors are shown.*

Machine	Coll-sion	Experiments	Pub. Year	$\sqrt{s}$ [GeV]	pt [GeV/c]	[R]/[U]
ISR	$p+p$	SS [46]	1973	23.2-52.7	1-2.5	[U]
		Eggert *et al.* [49]	1975	23.6-62.9	0.5-7.6	[R]
		CCR [47]	1973	23.5-62.4	2.5-9.0	[U]
		CCRS [48]	1975	23.5-62.4	2.5-7.5	[R]
		R702 (CSS) [50]	1978	53,63	5.3-16.5	[U]-η
		R108 (CCOR) [51]	1978	30.7-62.4	3.7-13.7	[U]
		R110 (BCMOR) [52]	1987	31	3.4-8.4	[U]
		R806 (ABCS) [53]	1979	30.6-62.4	3-10	[R]
			1979	52.7-62.4	7-15	[U]-η
		R807 (AFS) [55]	1983	63	4.8-11.4	[R]
SPS	fixed p	NA24 [58]	1987	23.7	1.3-6.0	[R]
		WA70 [59]	1988	22.9	4.0-6.5	[R]
		UA6 [60]	1998	24.3	4.1-7.7	[R]
S$p\bar{p}$S	$p+\bar{p}$	UA2 [61]	1982	540	1.5-4.4	[R]
			1985	540	5.8-14.5	[U]-$\eta\gamma$
FNAL	fixed p	E268 [62]	1976	13.6-19.4	1.0-5.0	[R]
		E704 [63]	1996	19.4	2.5-4.1	[R]
Tevatron	fixed p	E706 [64]	2003	31.5,38.7	1-10	[R]

Table D.1: *List of π^0 measurement at pseudo-rapidity≈0. The last column represents two photons from π^0 are [R]resolved or [U]unresolved. When the contribution of η and direct-γ are corrected in the case of the unresolved π^0, (-η) or (-γ) are shown in the column.*

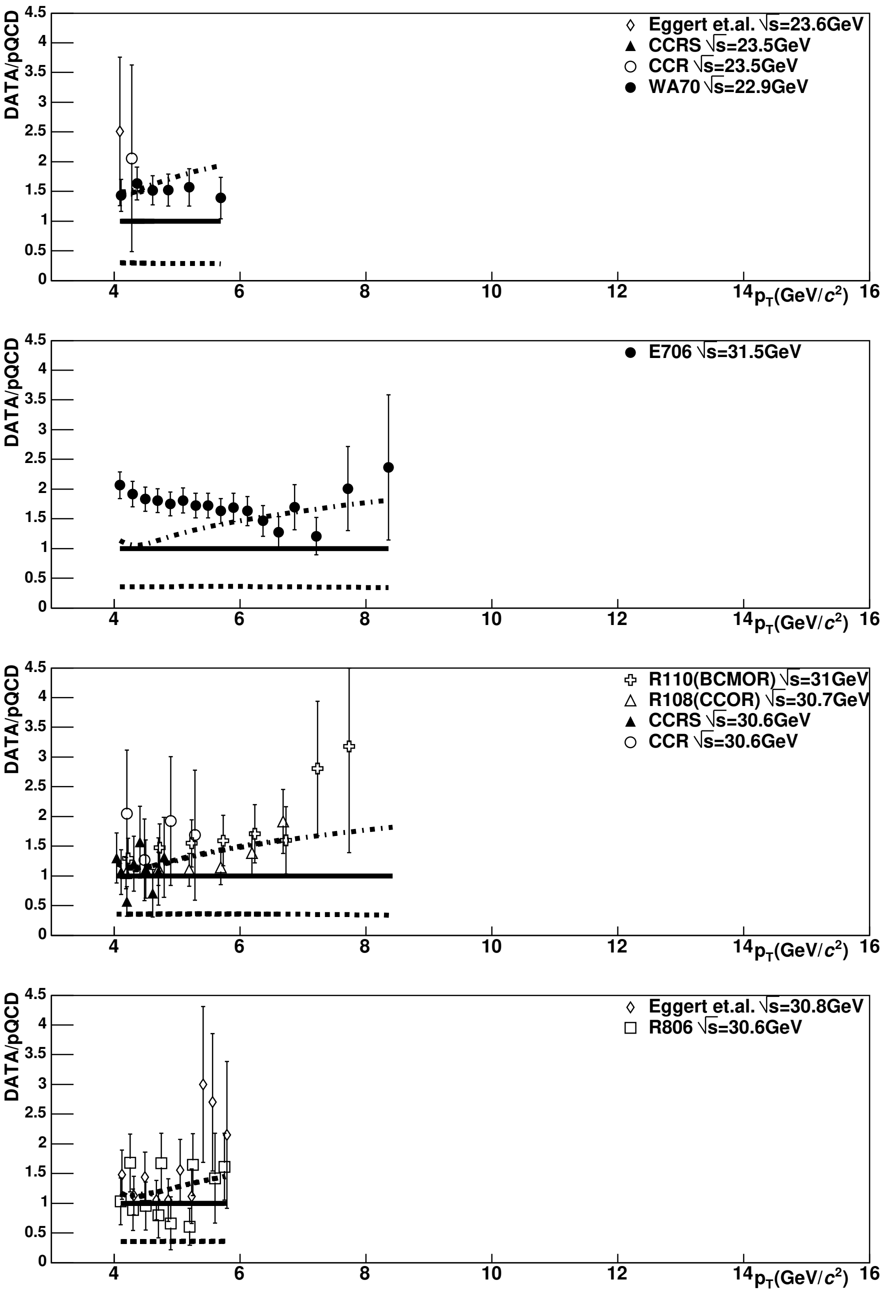

Figure D.3: *Ratios of the inclusive* π^0 *cross section at* $\sqrt{s}$ *of* $\approx$ *20GeV and* $\approx$ *30GeV to an NLO pQCD calculation with the scale of* $\mu = 1/2p_T$. *The systematic and statistical errors are added in quadrature and shown in the ratios.*

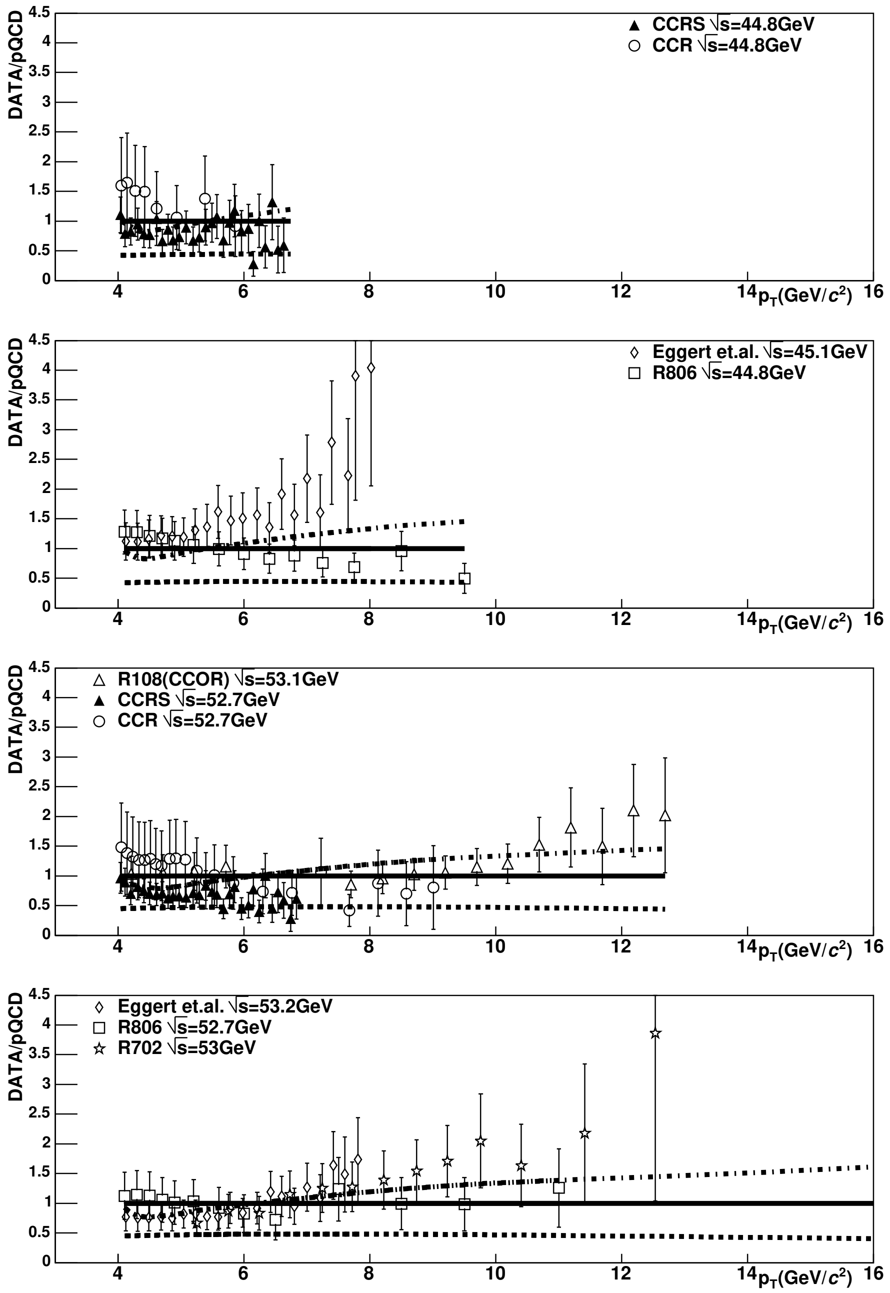

Figure D.4: *Ratios of the inclusive* π^0 *cross section at* $\sqrt{s}$ *of* $\approx$ *40GeV and* $\approx$ *50GeV to NLO pQCD calculation with the scale of* $\mu = 1/2p_T$*. The systematic and statistical errors are added in quadrature and shown in the ratios.*

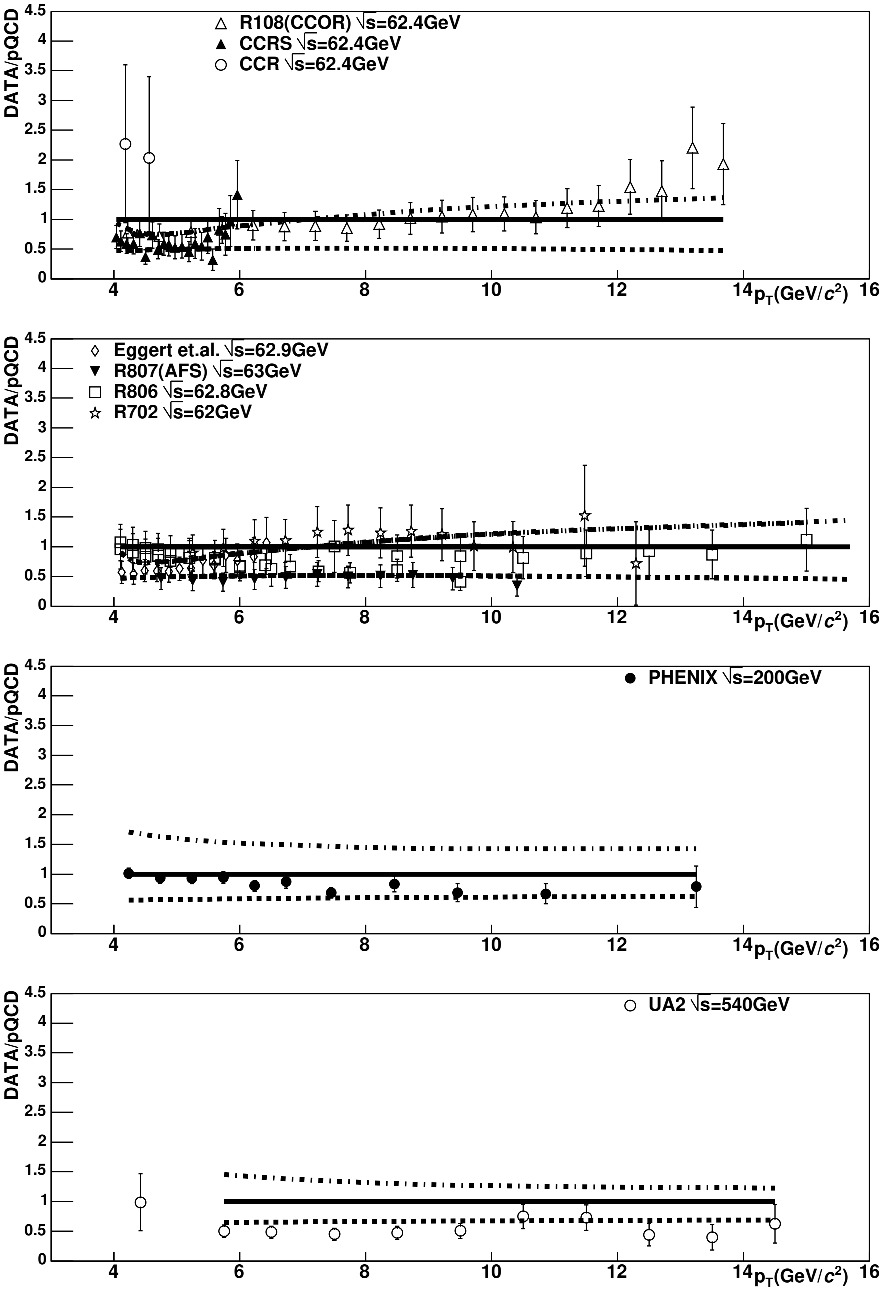

Figure D.5: *Ratios of the inclusive* π^0 *cross section at* $\sqrt{s}$ *of* $\approx$ *60GeV, 200GeV, and 540GeV to NLO pQCD calculation with the scale of* $\mu = 1/2p_T$ *for* $\sqrt{s} < 100$ *and* $\mu = p_T$ *for* $\sqrt{s} > 100$*. The systematic and statistical errors are added in quadrature and shown in the ratios.*

Bibliography

[1] J. F. Owens, Rev. Mod. Phys. **59** (1987) 465

[2] S. Weinberg, Phys. Rev. Lett. **31** (1973) 494, H. Fritzsch, M. Gell-Mann, and H. Leutwyler, Phys. Lett. **47B** (1973) 365, D. J. Gross, F. Wilczek, Phys. Rev. **D8** (1973) 3633

[3] E. D. Bloom *et al.*, Phys. Rev. Lett. **23** (1969) 930, M. Breidenbach *et al.*, Phys. Rev. Lett. **23** (1969) 935

[4] R. P. Feynman, Phys. Rev. Lett. **23** (1969) 1415

[5] J. D. Bjorken and E. A. Paschos, Phys. Rev. **D185** (1969) 1975

[6] CDF collaboration: F. Abe *et al.*, Phys. Rev. Lett. **74** (1995) 2626, D0 collaboration: S. Abachi *et al.*, Phys. Rev. Lett. **74** (1995) 2632

[7] P. M. Stevenson, Phys. Rev. **D23** (1981) 1981

[8] SLAC collaboration: L. W. Whitlow *et al.*, Phys. Lett. **B282** (1992) 475

[9] H1 collaboration: S. Aid *et al.*, DESY 96-039 (1996)

[10] ZEUS collaboration: M. Derrick *et al.*, Z. Phys. **C69** (1996) 607

[11] BCDMS collaboration: A. C. Benvenuti *et al.*, Phys. Lett. **B223** (1989) 485

[12] E665 collaboration: M. R. Adams *et al.*, Phys. Rev. **D54** (1996) 3006

[13] EMC collaboration: Aubert *et al.*, Nucl. Phys. **B259** (1985) 189

[14] NMC collaboration: M. Arneodo *et al.*, Phys. Lett. **B364** (1995) 197

[15] CCFR collaboration: W. G. Seligman *et al.*, Phys. Rev. Lett. **79** (1997) 1213

[16] Particle Data Book, K. Hagiwara *et al.*, Phys. Rev. **D66** (2002) 010001

[17] NA51 collaboration: A. Baldit *et al.*, Phys. Lett. **B332** (1994) 244

[18] E866 collaboration: E. A. Hawker *et al.*, Phys. Rev. Lett. **80** (1998) 3715

[19] CDF collaboration: F. Abe *et al.*, Phys. Rev. Lett. **81** (1998) 5754

[20] CDF collaboration: T. Affolder *et al.*, Phys. Rev. **D64** (2001) 032001

[21] D0 collaboration: B. Abbott *et al.*, Phys. Rev. Lett **86** (2001) 1707; Phys. Rev. **D64** (2001) 032003.

[22] W. Vogelsang and M. R. Whalley, J. Phys. G: Nucl. Part. Phys. **23** (1997) 1-69

[23] GRV collaboration: Z. Phys. **C67** (1995) 433

[24] CTEQ collaboration: H. Lai *et al.*, Eur. Phys. J. **C12** (2000) 375, H. Lai *et al.*, Phys. Rev. **D51** (1995) 4763.

[25] MRST collaboration: Alan D.Martin *et al.*, Eur. Phys. J. **C4** (1998) 463

[26] S. I. Alekhin, Phys. Rev. **D68** (2003) 014002, hep-ph/0211096

[27] CTEQ collaboration: J. Pumplin *et al.*, JHEP **0207** (2002) 012, hep-ph/0201195

[28] MRST collaboration: A. D. Martin *et al.*, Eur. Phys. J. **C28** (2003) 455, hep-ph/0211080, hep-ph/0308087

[29] ZEUS collaboration: S. Chekanov *et al.*, Phys. Rev. **D67** (2003) 012007

[30] MRST collaboration: A. D. Martin *et al.*, Phys. Lett. **B531** (2002) 216, hep-ph/0201127

[31] TPC collaboration: H. Aihara *et al.*, Phys. Rev. Lett. **61** (1988) 1263

[32] DASP collaboration: R. Brandelik *et al.*, Nucl. Phys. **B148** (1979) 189

[33] ARGUS collaboration: H. Albrecht *et al.*, Z. Phys. **C44** (1989) 547

[34] TASSO collaboration: M. Althoff *et al.*, Z. Phys. **C17** (1983) 5,

[35] SLD collaboration: W. Braunschweig *et al.*, Z. Phys. **C42** (1989) 189

[36] SLD collaboration: K. Abe *et al.*, Phys. Rev. **D59** (1999) 052001

[37] ALEPH collaboration D. Buskulic *et al.*, Phys. Lett. **B357** (1995) 487, Z. Phys. **C66** (1995) 355, Phys. Rep. **294** (1998) 1

[38] OPAL collaboration: R. Akers *et al.*, Z. Phys. **C67** (1995) 27, G. Abbiendi *et al.*, Eur. Phys. J. **C11** (1999) 217

[39] DELPHI collaboration: D. Buskulic *et al.*, Phys. Lett. **B357** (1995) 487, Eur. Phys. J. **C5** (1998) 585, CERN-EP/99-144

[40] one of pioneering works, R. D. Field, R. P. Feynman, Phys. Rev. **D15** (1977) 2590

[41] J. Binnewies *et al.*, Phys. Rev. **D52** (1995) 4947

[42] S. Kretzer, Phys. Rev. **D62** (2000) 054001, hep-ph/0003177

[43] B. Kniehl *et al.*, Nucl. Phys. **B582** (2000) 514, hep-ph/0010289

[44] L. Bourhis, Eur. Phys. J. **C19** (2001) 89, hep-ph/0009101

[45] L. Bourhis, Eur. Phys. J. **C2** (1998) 529, hep-ph/9704447

[46] SS collaboration: M. Banner *et al.*, Phys. Lett. **B44** (1973) 537

[47] CCR collaboration: F. W. Büsser *et al.*, Phys. Lett. **B46** (1973) 471

[48] CCRS collaboration: F. W. Büsser *et al.*, Nucl. Phys. **B106** (1976) 1

[49] K. Eggert *et al.*, Nucl. Phys. **B98** (1975) 45

[50] R702(CSS) collaboration: A. B. Clark *et al.*, Phys. Lett. **B74** (1978) 267

[51] R108(CCOR) collaboration: A. L. S. Angelis *et al.*, Phys. Lett. **B79** (1978) 505

[52] R110(BCMOR) collaboration: A. L. S. Angelis *et al.*, Phys. Lett. **B185** (1987) 213

[53] R806(ABCS) collaboration: C. Kourkoumelis *et al.*, Phys. Lett. **B83** (1979) 257, Phys. Lett. **B84** (1979) 271

[54] R806(ABCS) collaboration: C. Kourkoumelis *et al.*, Z. Phys. **C5** (1980) 95

[55] R807(AFS) collaboration: T. Åkesson *et al.*, Phys. Lett. **B128** (1983) 354, Sov. J. Nucl. Phys. **51** (1990) 836

[56] R108(CCOR) collaboration: A. L. S. Angelis *et al.*, Phys. Lett. **B94** (1980) 106, CERN-EP/82-106

[57] R806(ABCS) collaboration: C. Kourkoumelis *et al.*, Phys. Lett. **B104** (1979) 75

[58] NA24 collaboration: C. De Marzo *et al.*, Phys. Rev. **D36** (1987) 16

[59] WA70 collaboration: M. Bonesini *et al.*, Z. Phys. **C38** (1988) 371, CERN-EP/87-222

[60] UA6 collaboration: G. Ballocchi *et al.*, Phys. Lett. **B436** (1998) 222

[61] UA2 collaboration: M. Banner *et al.*, Phys. Lett. **B115** (1982) 59, Z. Phys. **C27** (1985) 329

[62] E268 collaboration: G. Donaldson *et al.*, Phys. Lett. **B73** (1978) 375, Phys. Rev. Lett. **36** (1976) 1110

[63] E704 collaboration: D. L. Adams *et al.*, Phys. Rev. **D53** (1996) 4747

[64] E706 collaboration: L. Apanasevich *et al.*, Phys. Rev. **D68** (2003) 052001

[65] F. Aversa *et al.*, Nucl. Phys. **B327** (1989) 105

[66] P. Aurenche *et al.*, Eur. Phys. J. **C13** (2000) 347, hep-ph/9910252

[67] E80 collaboration: M. J. Alguard *et al.*, Phys. Rev. Lett. **37** (1976) 1261, Phys. Rev. Lett. **23** (1969) 930,

[68] E130 collaboration: G. Baum *et al.*, Phys. Rev. Lett. **51** (1983) 1135

[69] EMC collaboration: J. Ashman *et al.*, Phys. Lett. **B206** (1988) 364, Nucl. Phys. **B328** (1989) 1

[70] E142 collaboration: P. L. Anthony *et al.*, Phys. Rev. Lett. **71** (1993) 959

[71] E143 collaboration: K. Abe *et al.*, Phys. Rev. Lett. **74** (1995) 346, Phys. Rev. Lett. **75** (1995) 25

[72] SMC(NA47) collaboration: D. Adams *et al.*, Phys. Lett. **B357** (1995) 248

[73] PHENIX collaboration: N. Saito *et al.*, Nucl. Phys. **A638** (1998) 575

[74] PHENIX collaboration: S. S. Adler *et al.*, submitted to Phys. Rev. Lett., hep-ex/0404027

[75] `http://www.phys.psu.edu/~cteq/`

[76] Z. Fodor, S. D. Katz, JHEP **0203** (2002) 014; hep-lat/0106002

[77] L. D. Landau and I. J. Pomeranchuk, Dokl. Akad. Nauk. SSSR **92** (1953) 92; A. B. Migdal Phys. Rev. **103** (1956) 1811

[78] K. Kasahara, Phys. Rev. **D31** (1985) 2737

[79] E146 collaboration: P. L. Anthony *et al.*, Phys. Rev. **D56** (1997) 1373

[80] M. Gyulassy and X. N. Wang, Nucl. Phys. **B420** (1994) 583; X. N. Wang, Phys. Rev. **C55** (1997) 3047

[81] WA80 collaboration: R. Albrecht *et al.*, Eur. Phys. J. **C5** (1998) 255 , nucl-ex/9805007

[82] WA98 collaboration: M. M. Aggarwal *et al.*, Phys. Rev. Lett. **81** (1998) 4087, nucl-ex/9806004

[83] X.N.Wang, Phys. Rev. Lett. **81** (1998) 2655, hep-ph/9804384

[84] S. J. Brodsky and J. F. Gunion, Phys. Rev. **D17** (1978) 848

[85] J. F. Gunion and G. Bertsch, Phys. Rev. **D25** (1982) 746

[86] R. Baier *et al.*, Phys. Lett. **B345** (1995) 277

[87] B. G. Zakharov, JETP Lett. **65** (1997) 615

[88] K. Adcox *et al.*, Phys. Rev. Lett. **88** (2002) 022301, Phys. Lett. **B561** (2002) 82-92

[89] R. J. Glauber and G. Matthiae, Nucle. Phys. **B21** (1970) 135

[90] S. S. Adler *et al.*, Phys. Rev. Lett. **91** (2003) 072301, Phys. Rev. **C69** (2004) 034910

[91] H. Hahn *et al.*, Nucl. Instr. and Meth. **A499** (2003) 245

[92] K. Adcox *et al.*, Nucl. Instr. and Meth. **A499** (2003) 469

[93] C. Adler *et al.*, Nucl. Instr. and Meth. **A499** (2003) 433

[94] M. Allen *et al.*, Nucl. Instr. and Meth. **A499** (2003) 549

[95] S. H. Aronson *et al.*, Nucl. Instr. and Meth. **A499** (2003) 480

[96] K. Adcox *et al.*, Nucl. Instr. and Meth. **A499** (2003) 489

[97] M. Aizawa *et al.*, Nucl. Instr. and Meth. **A499** (2003) 508

[98] L. Aphecetche *et al.*, Nucl. Instr. and Meth. **A499** (2003) 521

[99] S. N. White, Proc. of the Fourth Int. Conf. on Calorimetry in High Energy Physics (1994).

[100] J. Badier *et al.*, Nucl. Instr. and Meth. **A348** (1994) 74.

[101] E. Tarkovsky, Nucl. Instr. and Meth. **A379** (1996) 515.

[102] G. David *et al.*, IEEE Trans. Nucl. Sci. **45** (1998) 705.

[103] G. David *et al.*, IEEE Trans. Nucl. Sci. **45** (1998) 692.

[104] T. C. Awes *et al.*, nucl-ex/0202009

[105] G. David *et al.*, IEEE Trans. Nucl. Sci. **42** (1995) 306.

[106] D. Muller, Phys. Rev. **5** (1972) 2677.

[107] G. Bathow *et al.*, Nucl. Phys. B **20** (1970) 592.

[108] T. C. Awes *et al.*, Nucl. Instr. and Meth. **A311** (1992) 130.

[109] GEANT 3.21, CERN Program Library
`http://wwwasd.web.cern.ch/wwwasd/geant/index.html`

[110] S. S. Adler *et al.*, Nucl. Instr. and Meth. **A499** 560-592 (2003)

[111] S. S. Adler *et al.*, Nucl. Instr. and Meth. **A499** 593-602 (2003)

[112] PYTHIA v5.720 `http://www.thep.lu.se/~torbjorn/Pythia.html`

[113] `http://physics.nist.gov/PhysRefData`

[114] C. Albajat *et al.*, Nucl. Phys. **B335** (1990) 261.

[115] `http://durpdg.dur.ac.uk/hepdata`

[116] CCRS collaboration: F. W. Büsser *et al.*, Phys. Lett. **B55** (1975) 232

[117] R110(BCMOR) collaboration: A. L. S. Angelis *et al.*, Nucl. Phys. **B327** (1989) 541

[118] NA24 collaboration: C. De Marzo *et al.*, Phys. Rev. **D36** (1987) 8

[119] J. D. Bjorken, Phys. Rev. **179** (1969) 1547

[120] R. F. Cahalan *et al.*, Phys. Rev. **D11** (1975) 1199

[121] R. Blankenbecler, S. J. Brodsky, and J. F. Gunion, Phys. Lett. **B42** (1972) 461, Phys. Rev. **D18** (1978) 900

[122] D. Antreasyan *et al.*, Phys. Rev. **D19** (1979) 764

[123] `http://wwwlapp.in2p3.fr/lapth/PHOX_FAMILY/readme_inc.html`

[124] N. Kidonakis and J. F. Owens, Phys. Rev. **D61** (2000) 094004

[125] A. Kulesza, G. Sterman, and W. Vogelsang, Nucl. Phys. **A721** (2003) 591

[126] L. Apanasevich *et al.*, Phys. Rev. **D59** (1999) 074007

[127] Hung-Liang Lai *et al.*, Phys. Rev. **D58** (1998) 114020

[128] J. Spanggaard, *Delay Wire Chambers A Users Guide*, CERN SL-Note-98-023 (1998).

[129] A. L. Wintenberg *et al.*, Proc. of the Fourth Int. Conf. on Electronics for Future Colliders, LeCroy Corp. (1994).

[130] G. Ambrosini *et al.*, Eur. Phys. J. C **10** (1999) 605.

[131] G. Bocquet *et al.* (UA1 Collaboration), Phys. Lett. **B366** (1996) 441

[132] G. Bocquet *et al.* (UA1 Collaboration), Phys. Lett. **B366** (1996) 434

[133] G. J. Alner *et al.* (UA5 Collaboration), Nucl. Phys. **B258** (1985) 505.

[134] T. Åkesson *et al.* (AFS Collaboration), Z. Phys. **C18** (1983) 5.